www.itis.ethz.ch/pem2017

Abstract Book

PEM2017

2nd International Workshop on Photonics Applied to Electromagnetic Measurements

5 – 6 October 2017, Zurich, Switzerland

IT'IS FOUNDATION

TABLE OF CONTENTS

KEYNOTE

SESSION 1 **Basic theory and techniques of photonics applied to EM measurements**

SESSION 2 **Photonics applied to EM measurement systems and new applications**

SESSION 3 **New technologies in photonics applied to EM measurements**

SESSION 4 **Biomedical applications of photonics applied to EM measurements**

TABLE OF CONTENTS
POSTER

Antenna Measurement Using Photonics Applied to Electromagnetic Measurement Technology

Satoru KUROKAWA[*], Masanobu HIROSE, Michitaka AMEYA, Yuanfeng SHE, and Sayaka MATSUKAWA
National Metrology Institute of Japan, National institute of advanced industrial science and technology (AIST),
305-8563 Tsukuba, Japan
*Corresponding author: satoru-kurokawa@aist.go.jp

Abstract – We are developing some antenna measurement systems using photonics applied to electromagnetic measurement (PEM) technologies. PEM system usually uses optical devices and optical fibers. PEM system can replace the metal coaxial cables and suppress the reflection waves from the coaxial cable. In this paper, we show some antenna measurement systems using PEM technology and antenna measurement results up to 40 GHz.

Keywords – antenna measurement; optical device; photonics applied to electromagnetic measurement technology; antenna calibration; electromagnetic interference measurement

1. Introduction

The conventional antenna measurement system and electromagnetic interference (EMI) measurement system usually use metal coaxial cables. CISPR (Comité International Spécial des Perturbations Radioélectriques) 16-1 specifies the measurement method, characteristics and performance of equipment for the measurement of radio disturbance in the frequency range from 9 kHz to 18 GHz [1]. Further, 5th generation mobile network will use high frequency band including from 27.5 GHz to 71 GHz [2]. Coaxial cable system has some problems, such as the attenuation of signals in the cables, reflection waves on the outside surface and the difficulty of its handling. For this reason, we have already proposed some optical fiber link antenna measurement systems.

In this paper, we explain recent research topics for antenna measurement systems using the PEM technology. At first, we explain an antenna measurement system using a photo biased photo diode (PD) and electro absorption optical intensity modulator (EAM) up to 40 GHz. Then, we explain an optical fiber link port extender for vector network analyzer (VNA) up to 4 GHz.

2. Antenna Measurement Using a Photo Diode and a Electro Absorption Optic Intensity Modulator up to 40 GHz [3][4]

Our proposed optical fiber link antenna measurement system consists of PD, EAM and an optical fiber. Our using EAM and PD can use for antenna measurement without thermo-electric cooler (TEC) and DC bias. Figure 1 shows outline of our proposed antenna measurement system. Figure 2 shows frequency characteristics of our system with E8363C vector network analyzer of Keysight technologies Inc.

We demonstrate antenna measurement using two same type of antennas. Two antennas set face to face with the variable distance from 1.5 m to 4 m. Figure 3 shows the measured $S_{21}(\omega)$s of model 3115 double ridged guide horn antennas (DRGH) using EAM – PD with microwave amplifier as a receiving system. Figure 4 shows the measured $S_{21}(\omega)$s of WR-28 standard gain horn antennas using EAM with microwave amplifier - PD with microwave amplifier as a receiving system. $S_{21}(\omega)$s are measured by the VNA after response calibration. The frequency range, the frequency interval, and the IF frequency of the VNA are from 100 MHz to 40 GHz, 100 MHz, and 5 Hz, respectively. These results show the fact that our proposed antenna measurement system can measure the antenna response in the frequency range from 1 GHz to 40 GHz.

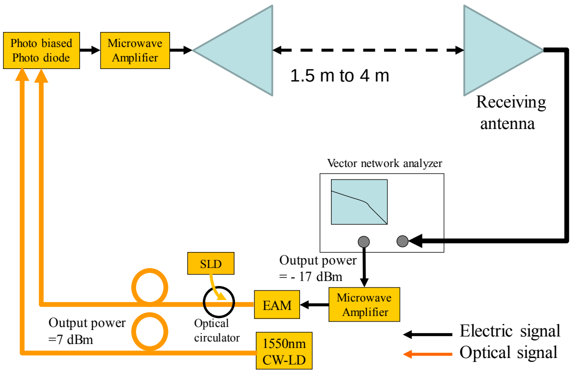

(a) Outline of the antenna measurement setup

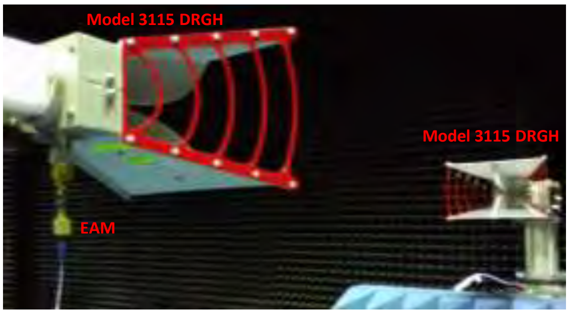

(b) Photo of the setup for DRGH

Figure 1. Antenna measurement setup using our system

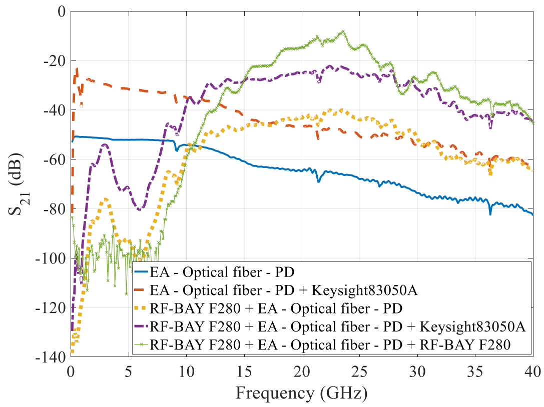

Figure 2. Frequency response of our system with VNA

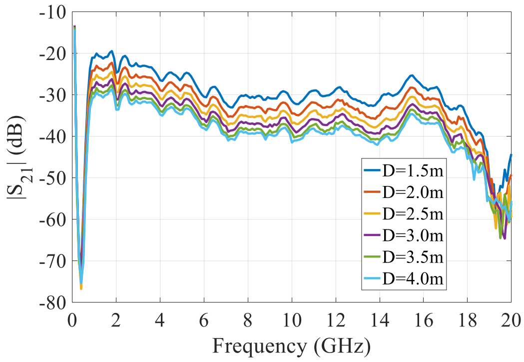

Figure 3. S_{21} (dB) measurement results of Model 3115 double ridged guide horn antenna

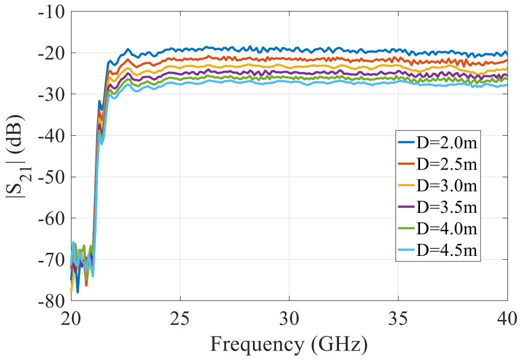

Figure 4. S_{21} (dB) measurement results of WR-28 standard gain horn antennas

3. Antenna Measurement Using Bi-Directional Optical Fiber Link port extender of VNA [5][6]

We have proposed a port extender of VNA using bi-directional type optical fiber link transceivers [5][6]. Figure 5 shows the outline of our system with VNA. Our proposed port extender connects to the direct access port of VNA. Then, our proposed transceivers connect to the transceivers for device under measurement by optical fibers. Figure 6 shows the measurement results of $S_{21}(\omega)$s using our proposed system with two 30 m optical fibers and step attenuator. [ATT= x dB] indicates the measurement frequency response for the case of ATT= x dB attenuation. These results show that the dynamic range of our system is more than 100 dB in the frequency range from 100 MHz to 3 GHz.

To demonstrate the validity of the proposed optical fiber link port extender, we carry out the single antenna gain measurement method [7] for model 3115 DRGH of ETS-Lindgren Inc. in one-port calibration of VNA. DRGH set perpendicularly to the ground plane with the variable position from 1.5 m to 5 m high above it. The reflection coefficient $S_{11}(\omega)$ is measured by our proposed system with VNA in frequency-domain. Then, we apply the single antenna method for estimating the antenna gain of DRGH. Finally, we estimate the antenna gain using the phase center modified Friis transmission formula[8]-[10].

$$|s_{21}(\omega,z)|^2 = \left(1-|\Gamma_1(\omega)|^2\right)\left(1-|\Gamma_2(\omega)|^2\right) \left(\frac{\lambda}{4\pi(z+d_1(\omega)+d_2(\omega))}\right)^2 G_{\mathrm{far\_1}}(\omega)G_{\mathrm{far\_2}}(\omega) \qquad (1)$$

For self-calibration method,

$$\begin{aligned} &\Gamma_1(\omega) = \Gamma_2(\omega) = \Gamma(\omega), \\ &G_{\text{far\_1}}(\omega) = G_{\text{far\_2}}(\omega) = G_{\text{far}}(\omega), \\ &d_1(\omega) = d_2(\omega) = d(\omega) \\ &G_{\text{far}}(\omega) = \frac{4\pi(z_1 - z_2)}{\lambda}\left(1 - |\Gamma(\omega)|^2\right)^{-1} \\ &\qquad \left(\frac{1}{|s_{21}(\omega, z_1)|} - \frac{1}{|s_{21}(\omega, z_2)|}\right)^{-1} \qquad (2) \end{aligned}$$

Figure 7 shows the outline of measurement setup. Figure 8 shows the estimated antenna gain of single antenna method using the proposed system and the estimated antenna gain of 3-antenna extrapolation method using coaxial cable system. Figure 9 shows the difference of antenna factors between them. Difference of antenna factors is less than 0.8 dB in the frequency range from 1 GHz to 4 GHz. These results show the fact that our proposed system can measure the antenna gain up to 4 GHz.

4. Conclusion

In this paper, we have shown some antenna measurement system and antenna measurement results using photonic applied to electromagnetic measurement technology. Our proposed system can measure antenna characteristics up to 40 GHz without coaxial cables.

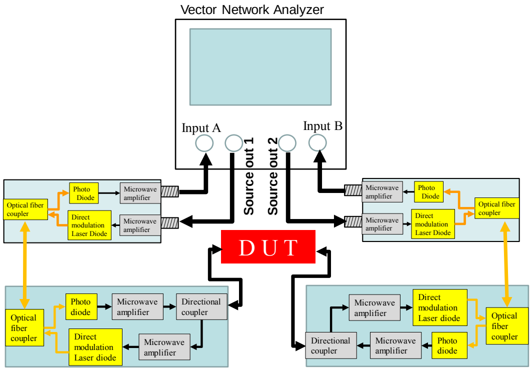

Figure 5. Measurement setup for the dynamic range of our proposed system

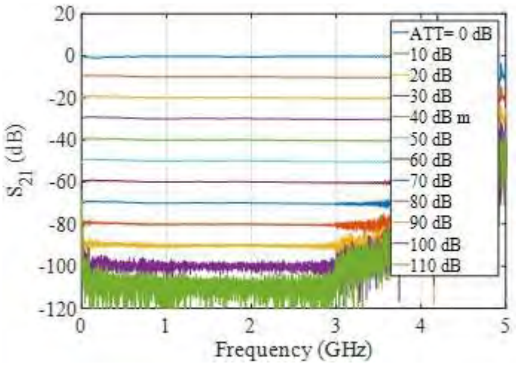

Figure 6. Dynamic range of our proposed system with VNA using two 30 m optical fiber cables

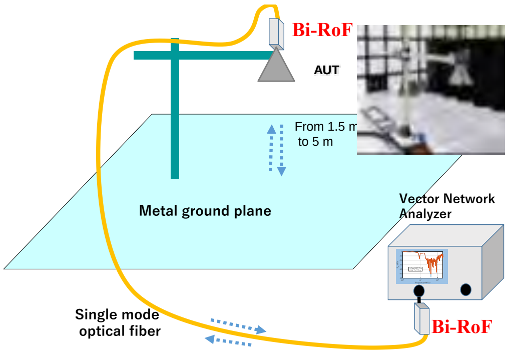

Figure 7. Setup for the measurement of antenna gain using our single antenna method.

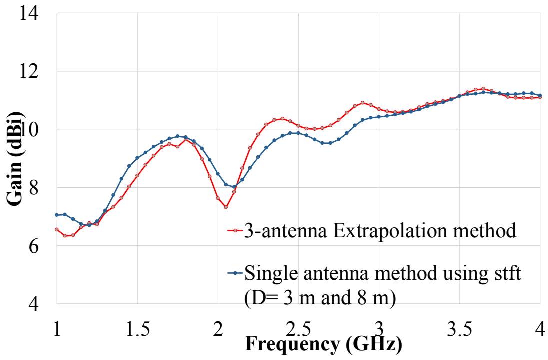

Figure 8. Estimated antenna factors compare with single antenna method using the proposed system and 3-antenna extrapolation method using coaxial cable system

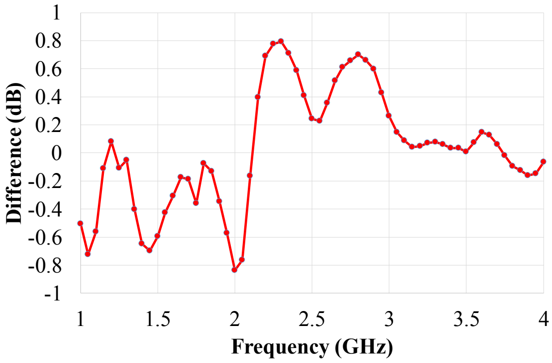

Figure 9. Difference of antenna factors between them

References

[1] CISPR 16-1-1:2015 Specification for radio disturbance and immunity measuring apparatus and methods - Part 1-1: Radio disturbance and immunity measuring apparatus - Measuring apparatus

[2] Leading towards Next Generation "5G" Mobile Services. Federal Communications Commission, https://www.fcc.gov/news-events/blog/2015/08/03/leading-towards-next-generation-5g-mobile-services

[3] S. Kurokawa, and M. Hirose, “Optical fiber link microwave measurement system using zero biased optical devices,” in Proc. of ICCEM 2017, March 2017.

[4] S. Kurokawa, and M. Hirose, “Microwave receiving system for antenna measurement using optical devices up to 40 GHz,” in Proc. of EuMW 2017, Oct. 2017.(to be published)

[5] S. Kurokawa, M. Hirose, Y. Toba, M. Onizawa, and J. Ichijo, ``Antenna Gain Estimation for a Single Antenna Measurement Using Bi-directional Optical fiber link transceiver,” in Proc. of 2016 IEEE CAMA, Oct. 2016.

[6] S. Kurokawa, M. Hirose, Y. Toba, M. Onizawa, and J. Ichijo, `` Optical Fiber Link Port Extender for Vector Network Analyzer,” in Proc. of 32nd URSI GASS, Aug. 2017.

[7] S. Kurokawa, M. Hirose, K. Komiyama, ``Experimental study of self-calibration method for Log-periodic antenna,'' Proceedings of ISAP2004, pp.285-288, Aug. 2004.

[8] K. Harima, “Accurate gain determination of LPDA by considering the phase center,” IEICE Electronics Express, vol.7, no.23, 1760-1765, Oct. 2010.

[9] M. Hirose, S. Kurokawa, M. Ameya, “Theoretical Investigation on Relationship Between Near-Field Gain and Far-Field Gain Using Phase Center,’’Technical report of IEICE, AMT2012-02, June, 2012. (In Japanese)

[10] S. Kurokawa, M. Ameya, and M. Hirose, ``Far filed gain estimation method for Japanese broadband antenna standard using time-frequency analysis,” Proc. PIERS 2013 Stockholm, pp. 838-842, Stockholm, Sweden, Aug. 2013.

Controlling Light-Matter Interactions on the Nanometer Scale

Lukas NOVOTNY [1*]
[1]Photonics Laboratory, ETH Zurich, 8093 Zurich, Switzerland
*Corresponding author: lnovtony@ethz.ch

Abstract – The past 20 years have brought exceptional control over light-matter interactions on the nanoscale. Today, localized optical fields are being probed with nanoscale materials, and, vice versa, nanoscale materials are being controlled and manipulated with localized fields. In this talk I will review both early and recent developments in near-field optical imaging and optical nanomanipulation.

Optical Sampling with a Picosecond Pulsed Laser and Its Application to High-Speed Time-Domain Electric-Field Sensing

Sze Y. SET[1*]
[1]Reseach Center for Advanced Science and Technology
The University of Tokyo, 4-6-1 Komaba, Meguro-ku, Tokyo 153-0053, Japan
*Corresponding author: set@cntp.t.u-tokyo.ac.jp

Abstract –We introduce an all-optical electro-optic (EO) probe with a broad frequency response. The 3-axis EO-probe contains no metallic elements at all, allowing a completely non-invasive measurement of electric field well beyond 18GHz, limited by the photodetector. We propose to use a non-synchronous all-optical sampling system using a picosecond pulsed laser, capable of measurement high-speed optical waveform to extend the bandwidth of the EO probe beyond the current limit to beyond 160GHz. This system allows a stable and unambiguous real-time waveform reconstruction for time-domain electric-field measurement.

Keywords – Electro-optic probe; electric field measurement; non-invasive sensor; picosecond optical sampling;

1. Introduction

Optical electric-field sensor [1-5] has been of much interest in applications where conventional metallic antenna-type probe fails to perform due to their invasiveness. Applications such antenna characterization, specific absorption ratio (SAR) measurement [2][3] for cellular mobile phone safety standard, electromagnetic compatibility (EMC) and so on, calls for high precision measurement of the 3-dimensional vectorial field distribution around the object under test. Optical electric-field sensors in the market are mostly based on Lithium-niobate waveguide Mach-Zehnder interferometer type configuration [1][4] with frequency response up to 10GHz, where sensor element such as dipole antennas are attached on the waveguide to enhance probe sensitivity and directivity. The presence of the metallic sensor element will disturb the surrounding electric-field and hence distorting measurement results.

A completely non-invasive, non-metallic EO probe has been demonstrated [3]. Miniaturized tip-on-fiber EO probe has also been realised [5]. In this talk, we introduce a 3-axis non-invasive EO probe based on the tip-on-fiber configuration with broadband frequency response over 18GHz, limited only by the bandwidth of the photo-detector. Here, we propose to use an all-optical sampling oscilloscope to drastically extend the operating bandwidth.

2. Configuration of the EO-Probe

The probe construction is depicted in Figure 1. The probe is based on a glass substrate with a plastic housing. 3 pieces of 1x1x1mm ZnTe crystals are used as the electro-optic sensors. The principle of the electric-field sensor is well described in [5].

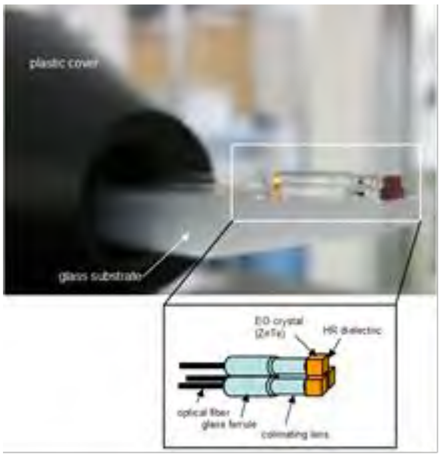

Figure 1. Construction of the EO-Probe tip.

An input laser light at ~1550nm is launched with a circular polarization, via a graded index collimating lens, incident to the corresponding crystal that has a HR dielectric coating at the end-facet to reflect the light back to the fiber. Each of the 3 crystals has its sensing axis aligned to one of the predetermined direction (X, Y, or Z). Incident electric-field will cause changes to the state of polarization of the reflected light. An all-optical polarization analyzer is constructed with miniaturized optics inside the probe main-body housing. The returning light from each of the 3 crystals are coupled back to 3 high-speed photo-detectors, respectively for the measurement of the vectorial electric field strength.

3. Experimental Setup

The performance of the probe is measurement using the experimental setup as shown in Figure 2. 1550nm CW laser with 80mW output power is launched into the EO probe, and the returning signal from the EO probe is detected using a high-speed photo-detector with frequency response of 1MHz – 18GHz. An optical low-noise optical amplifier is inserted together with a narrow band optical filter for the suppression of the amplified spontaneous emission (ASE) from the optical amplifier.

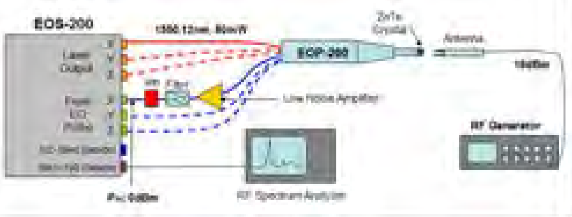

Figure 2. Experimental setup.

An RF signal generator with 16dBm output power is used to drive an antenna placed close to the tip of the probe with different orientation to suit the axis of measurement. The signal from the photo-detector is measured using an RF spectrum analyzer. It is evident that the signal-to-noise ratio and hence the sensitivity of the measured signal can be greatly enhanced with the low-noise optical amplifier and optical filter (Figure 3).

The frequency response of the EO probe is measured and the results are shown in Figure 4, exhibiting a broadband response from 1MHz to 18GHz, limited only be the photo-detector response. Z-axis has higher sensitivity due to its orientation favoring a closer placement of the test signal antenna.

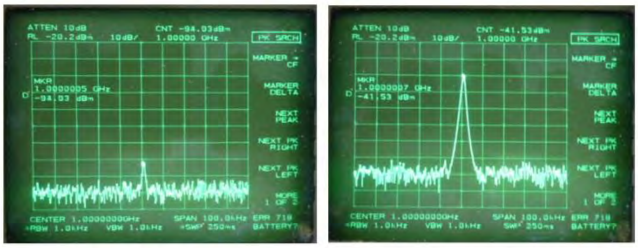

Without Optical Amplifier

With Optical Amplifier

Figure 3. Sensitivity enhancement with optical amplifier.

The results also suggested that the EO probe has a trend to have less sensitivity at lower frequency <1MHz. Indeed the EO probe has poor response for DC field. This can be explained by the fact that the crystal has no metallic contact and therefore a continuous DC electric-field would create a static charging effect, reversing the internal field in the crystal and results in reduction of the Pockel's effects.

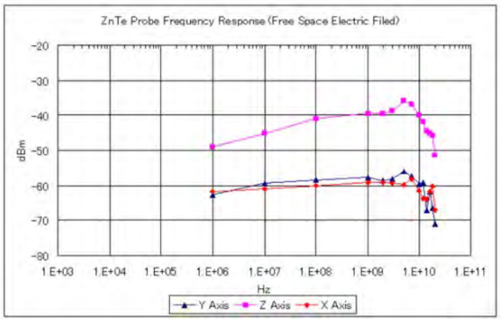

Figure 4. Frequency response of the 3-axis EO-

4. High-Speed Optical Sampling System

The sampling configuration is shown in Fig. 5. A polarization diversified fiber four-wave mixing gate is used as the ultra-fast sampling gate. The input signal is sampled by the free-running CNT mode-locked laser pulses via four-wave mixing, and the converted signal is filtered and detected using a photo-detector with 125MHz bandwidth and analog-to-digital (A/D) converted at 14bit into a long memory buffer. A fast algorithm similar to the one reported in [6] is used to recover the sampling internal for eye-diagram reconstruction.

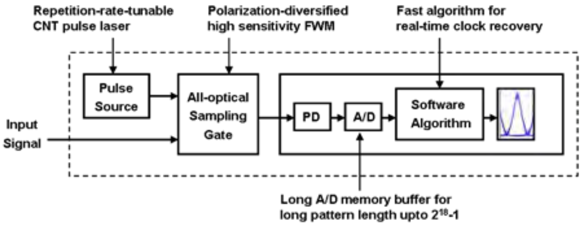

Figure 5. All-optical sampling system configuration.

The optical sampling system is used to measure (a) 40Gb/s RZ, and (b) 160Gb/s RZ signals. Both signals are optical time-domain multiplexed signals of 10Gb/s PRBS data streams. The real-time reconstructed eye-diagrams are shown in Fig. 6.

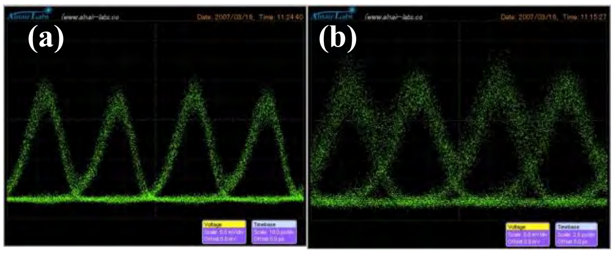

Figure 6. Waveforms of (a) 40Gb/s, and (b) 160Gb/s signals.

5. Summary

We have introduced a 3-axis EO probe which is completely non-metallic and therefore non-invasive. The EO probe has a broadband frequency response >18GHz, limited by the photo-detector used in the receiver. We proposed a technique to extend the frequency response using an all-optical sampling system and we expect the system to measure beyond 160GHz signals.

References

[1] N. Kuwabara, et al., “Development and analysis of electric field sensor using LiNbO3 optical modulator,” IEEE Trans. Electromagnetic Compatibility, vol. 34, no. 4, pp. 391-396, Nov. 1992.

[2] B. G. Loader, et al., “An optical electrical field probe for Specific Absorption Rate measurement,” 15th International Zurich Symposium on Electromagnetic Compatibility, 12C3, pp. 57-60, Zurich, Switzerland, 2003.

[3] T. Onishi, et al., “SAR measurement employing electro-optic (EO) probe without using metal,” in a joint meeting BioEM2005, Dublin, Ireland, June 2005.

[4] K. Tajima, et al., “Development of optical isotropic E-field sensor operating more than 10GHz using Mach-Zehnder interferometers,” IEICE Trans. Electron., Special Issue on Optical Fibers and Devices, vol. E85-C, no. 4, April 2002.

[5] H. Togo, et al., “Tip-on-fiber electro-optic probe for near field measurement,” NTT Technical Review, vol. 4, no. 1, Jan. 2006.

[6] T. Kiatchanog, et al., “Real-time all-optical waveform sampling using a free-running passively mode-locked fiber laser as the sampling pulse source” OFC’06, Anaheim, CA, paper OWN1,2006.

Coherent Detection of Terahertz-Wave by Parametric Up-Conversion at Room Temperature

Shin’ichiro HAYASHI* and Yoshinori UZAWA

National Institute of Information and Communications Technology, 184-8795, Koganei, Japan
*hayashi@nict.go.jp

Abstract – We demonstrate the coherent detection of terahertz-wave using parametric up-conversion in a nonlinear $LiNbO_3$ crystal. Nonlinear wavelength up-conversion techniques allow the terahertz waves to be visualized and their frequency and intensity determined directly. These results are very promising for extending applied research into the terahertz region, and we expect that these will open up new research fields such as information communications or nonlinear optics in the terahertz region.

Keywords – terahertz wave, nonlinear optics, wavelength up-conversion

1. Introduction

Over the past decade, there has been remarkable growth in the field of terahertz frequency science and engineering, which has become a vibrant, international, cross-disciplinary research activity [1]. Wavelength conversion in nonlinear optical materials is an effective method for generating and detecting terahertz waves owing to the high conversion efficiency, wide tunability, bandwidth, and room temperature operation. The large figure of merit of lithium niobate ($LiNbO_3$) makes this well-known nonlinear crystal ideal for such an application; terahertz wave parametric generation and detection are realized by stimulated polariton scattering via transverse optical phonons [2].

In this study, we propose up-conversion detection of terahertz waves in a $LiNbO_3$ crystal. The energy of one pumping photon split into two photons, a terahertz-wave and an idler wave. Mixing the terahertz-wave with the intense pumping beam at the input of the crystal, up-converted signal photons are created in difference-frequency mixing. Then, by injecting the terahertz-wave satisfying phase matching condition, the up-converted signal was seeded and parametrically amplified by the $LiNbO_3$ optical parametric amplifier.

However, a number of other nonlinear processes also occur when a high-intensity laser beam propagates through a nonlinear crystal. By exploiting a single-mode oscillated microchip Nd:YAG laser with a sub-nanosecond pulse width [3], a narrow linewidth, high-efficiency wavelength conversion can be performed by the SRS [4].

2. Experiment

In our experimental setup, shown in Figure 1, the pumping beam from the microchip Nd:YAG laser is amplified in two Nd:YAG rods in a double-pass configuration. The seeding beam from an external cavity

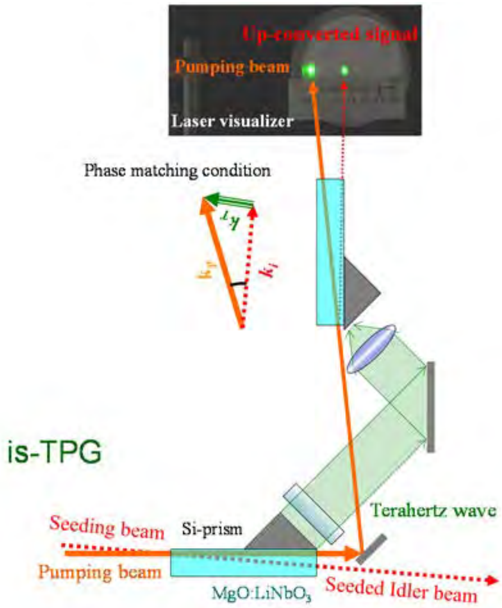

Figure 1. Experimental Setup. Terahertz waves are generated by an injection-seeded terahertz wave parametric generator (is-TPG).

diode laser is amplified by an Yb-doped fiber amplifier. The pumping and seeding beam diameter on the crystal are about 1.5 mm (FWMH). We used a 50-mm-long nonlinear MgO:LiNbO$_3$ crystal with a Si-prism as an efficient output coupler for the terahertz waves. Owing to the grating and confocal arrangement, the noncollinear phase matching condition is satisfied automatically when the wavelength of the seeding beam is changed. The terahertz-wave output extracted through the Si-prism was measured using a calibrated pyroelectric detector (THZ5I-MT-BNC; Gentec-EO) with two lenses (Tsurupica, Broadband Inc.), attenuators (TFA; CDP Corp.), an optical chopper, and a thick black polyethylene sheet for precise power measurements. The temporal waveform, wavelength, and linewidth of the terahertz wave were measured by a Schottky barrier diode and a pair of metal mesh plates. For the nonlinear up-conversion detection, the terahertz wave was focused onto another MgO:LiNbO$_3$ crystal. The incident angle between the terahertz wave and the pumping beam satisfies the noncollinear phase-matching conditions in the MgO:LiNbO$_3$ crystal. Mixing the terahertz wave with the pumping beam created a seeded difference-frequency up-converted signal, which was parametrically amplified by the MgO:LiNbO$_3$ optical parametric amplifier. The up-converted signals were visualized using an infrared laser visualizer (10VIZ-35; Standa Corp.) as visible green lights; the frequency and intensity were determined from the blinking position and intensity [5].

3. Results

Figure 2 shows the pictures of visualized up-converted signal on the laser beam visualizer and their positions as a function of the frequency of input terahertz wave. The red circles represent measured distance from the pumping beam, and the blue line represents the calculation results. The position and intensity of the up-converted signal depend on the frequency and intensity of the input terahertz wave respectively. As the frequency (intensity) of the input terahertz wave increases, the noncollinear phase-matching angle between the pumping beam and up-converted beam (intensity) also increase, which shifts the position (changes the brightness) of the signal. This is in good agreement with the calculation, and this makes it easy to identify the frequency and

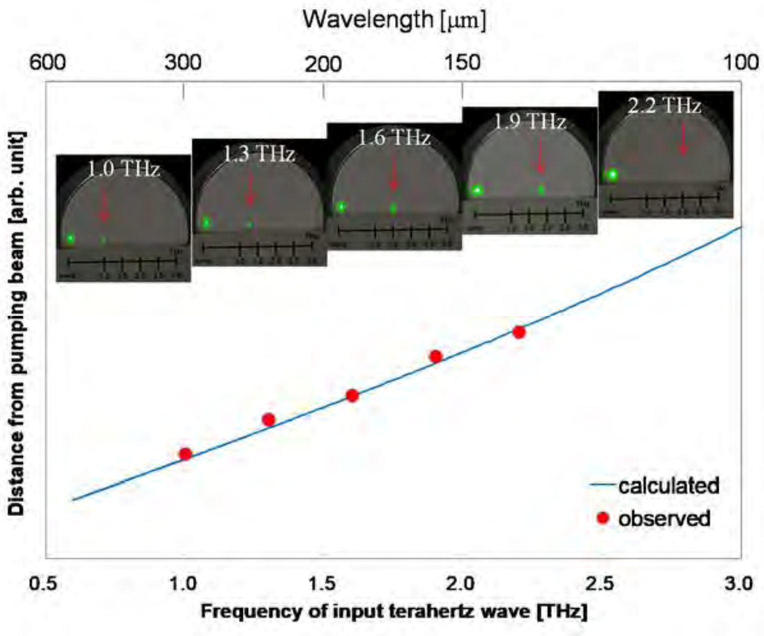

Figure 2. Pictures, observed and calculated position of the up-converted signals as a function of the frequency of input terahertz wave.

energy of the input terahertz wave from the position and intensity of the up-converted signal. When the energy of the input terahertz wave and pumping beam were 1 μJ/pulse at 1.9 THz and 10 mJ/pulse, respectively, the energy of the up-converted signal was 2 mJ/pulse at 1072 nm.

4. Conclusion

We demonstrated here the coherent detection of terahertz-wave by parametric up-conversion at Room Temperature, which is similar to a wavelength dispersive spectrometer. Additionally, this method also provides phase information of the terahertz wave through the interaction with a simultaneously generated terahertz wave and the idler beam, and furthermore, works as a terahertz wave amplifier by extracting the terahertz waves generated in a detection crystal. We speculate that the wavelength conversion techniques could be powerful tools not only for solving real world problems but also fundamental physics, such as real-time spectroscopic imaging, remote sensing, 3D-fabrication, and manipulation or alteration of atoms, molecules, chemical materials, proteins, cells, chemical reactions, and biological processes. We expect that these methods will open up new fields and tune up killer applications.

Acknowledgements

The authors would like to thank Dr. Minamide and Dr. Nawata of RIKEN, Prof. Kawase of Nagoya Univesity, Prof. Taira of IMS, and Prof. Ito of RIKEN for useful discussions. This work was partly supported by Collaborative Research Based on Industrial Demand of the Japan Science and Technology Agency (JST) and Grants-in-Aid for Scientific Research (KAKENHI 25220606, 25286075).

References

[1] E. Linfield, *"Terahertz applications - A source of fresh hope," Nat. Photonics*, **1**, 257–258 (2007).

[2] M. A. Piestrup, R. N. Fleming, and R. H. Pantell, *"Continuously tunable submillimeter wave source," APL*, **26**, 418 – 421 (1975).

[3] H. Sakai, H. Kan, and T. Taira, *">1 MW peak power single-mode high-brightness passively Q-switched* Nd^{3+}*:YAG microchip laser," Opt. Express*, **16**, 19891–19899 (2008).

[4] H. Minamide, S. Hayashi, K. Nawata, T. Taira, J. Shikata, and K. Kawase, *"Kilowatt-peak Terahertz-wave Generation and Sub-femtojoule Terahertz-wave Pulse Detection Based on Nonlinear Optical Wavelength-conversion at Room Temperature, JIMT*, **35**, 25-37, (2013).

[5] S. Hayashi, K. Nawata, T. Taira, J. Shikata, K. Kawase, and H. Minamide, *"Ultrabright continuously tunable terahertz-wave generation at room temperature," Scientific Reports*, **4**, 5045 (2014).

Remote Operating Point Control of Mach Zehnder Interferometer-Based Photonic Electric Field Sensors by Power Over Fiber

James E. TONEY[*], Andrea POLLICK, Vincent E. STENGER, and Sri SRIRAM

SRICO, Inc., 2724 Sawbury Blvd., Columbus, OH 43235, USA

*Corresponding author: jtoney@srico.com

Abstract – All-dielectric optical fiber coupled photonic probes offer many key benefits for electric field sensing. Benefits include ultra-high bandwidth from near DC to 100's of GHz, high spatial resolution on order of millimeters, and minimal perturbation of the measured field. Active remote biasing of such photonic probes is critical to maintain sensitivity and dynamic range performance over practical environmental test conditions. The challenge is in implementing active bias control without the use of field perturbing electric wires. In this paper, a commercially available power over fiber (PoF) component has been successfully used to control the bias of a lithium niobate Mach Zehnder interferometer (MZI) electric field sensor. Bias compensation over the entire Vpi characteristic of the sensor was demonstrated, completely mitigating any bias drift effects.

Keywords–photonic electric field sensor**;** bias control; power over fiber; Mach Zehnder Interferometer; lithium niobate

1. Introduction

The Mach Zehnder Interferometer (MZI) is one of the most widely used device structures for photonic electric field sensors. The MZI, implemented in lithium niobate ($LiNbO_3$) or similar materials, is a proven solution for electric field measurement from near DC to microwave frequencies. The primary challenge of the MZI is the tendency of the operating point to drift with environmental fluctuations, causing instability in the sensor response. Stabilization of the sensor response is crucial in applications that involve data acquisition over an extended time or over a wide range of operating temperatures. Near-field mapping of antenna radiation patterns is one such application. $LiNbO_3$ photonic E-field sensors have been demonstrated as near-field probes [1,2]. The ability to control and stabilize the operating point has the potential to substantially improve the performance of the sensors in near-field scanning applications.

In externally modulated analog optical links, bias drift of the MZI device is addressed by application of a DC bias voltage [3,4]. A feedback mechanism is used to adjust the bias and maintain a stable operating point. However, in electric field sensing, the electrical cables and wires needed to apply a bias voltage are undesirable, as they may perturb the electric field. Such perturbation obviates key benefits of an all-dielectric, fiber-coupled sensor. One solution, presented here, is remote bias control by a photovoltaic power-over-fiber module, which enables all-fiber sensor control and readout.

2. Drift Compensation

The same characteristic that gives the MZI high sensitivity to electric fields – its dependence on sub-wavelength variations in optical path between the two arms of the interferometer - makes it susceptible to operating point drift due to environmental fluctuations. Since the sensor response varies as the slope of the cosinusoidal MZI transfer function, this drift can lead to large variations in sensor response, making it difficult to extract the electric field from the measured signal. In particular, as the operating point approaches the null (zero optical transmission) or peak (maximum optical transmission) the slope approaches zero, and the sensor response becomes a quadratic function of the input field, resulting in frequency doubling [5]. Maximum response and maximum linearity occur when the operating point is at the quadrature point, where the optical transmission is one-half of its maximum value, and the slope is maximized.

One means of dealing with operating point drift is through post-processing of the measured signal based on monitoring of the received optical power. This technique has been demonstrated with electrode-free, z-cut sensors [6]. Correction of the measured field within a few percent is achievable even as the sensor operating point drifts over its entire range, with the exception of a narrow dead band around the null point, where the received optical power is too low to measure accurately.

While post processing can correct measurements that are well above the minimum detectable field, it cannot compensate for the loss of signal-to-noise ratio (SNR) as the operating point drifts far from the quadrature point. Active bias control must be implemented to maintain MZI probe sensitivity and dynamic range under varying environmental conditions. Commercially available bias controllers for electro-optic modulators are typically specified with phase stability of $\pm 1^{\circ}$ [7,8]. Even a much greater variation of $\pm 5^{\circ}$ around the quadrature point for an electric field sensor would result in less than 0.5 % variation in the measured field due to bias stability.

3. Bias Adjustment with Photovoltaic Power-Over-Fiber Module

For the remote electric field sensing application, the active bias control signal must be applied to the MZI sensor without the use of field perturbing electrical cables. One biasing method that avoids the need for an electrical cable is photovoltaic (PV) power-over-fiber (PoF) technology. The electrical output of a compact, fiber-coupled photovoltaic module is connected to the sensor electrodes. The output voltage of the photovoltaic is adjusted by varying the power of a remote, fiber-coupled optical source. In this proof-of-concept experiment, a 980 nm laser was used. The PoF module was a 6.0V unit produced by MH GoPower.

As an initial proof-of-concept, the PoF module was used to adjust the bias point of a commercial MZI telecommunications modulator. Figure 1 shows the experimental setup. Figure 2 shows the optical output power at 1550 nm of the modulator with the PV module connected to the bias electrode in parallel with a 1 MΩ load as a function of the current in the 980 nm laser. Once the current reaches the threshold of the 980 nm laser (approximately 25 mA) the modulator output decreases until the null bias point is reached, then increases as the current is increased further. The voltage output of the PV module at the null was 2.5 V. Beyond approximately 60 mA the output of the photovoltaic begins to saturate, producing the asymmetry in the curve.

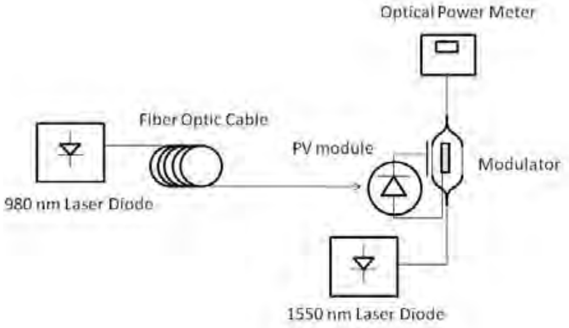

Figure 1. Experimental setup for demonstrating bias adjustment of a commercial MZI modulator using a power-over-fiber module.

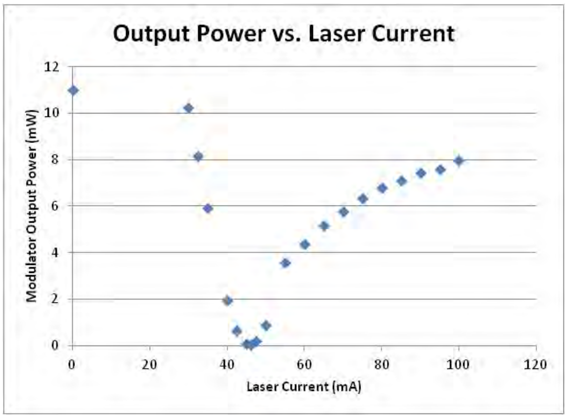

Figure 2. Optical output power of MZI modulator vs. current in the 980 nm laser.

4. Sensor Bias Control by Power-Over-Fiber

Once the feasibility of adjusting the bias point of a modulator was established, the PoF module was connected to the electrodes of an X-cut Ti:LiNbO$_3$ photonic electric field sensor to demonstrate optimization of sensor response. Details of sensor design and fabrication have been reported elsewhere [9].

The response of the sensor to a 300 MHz tone in a TEM test cell was measured as a function of the 980-nm laser current. The experimental setup was comparable to Figure 1, except that the output of the sensor was split by a 3-dB coupler, to enable simultaneous measurement of the received optical power and the RF signal. One output of the coupler was connected to the input of a high-speed photoreceiver. The photoreceiver output was connected through a low-noise amplifier to an RF spectrum analyzer (SA). The -20 dBm, 300 MHz calibration output of the SA was used to drive the TEM cell input.

The sensor operating point at room temperature was initially near the null (approximately 16 dB below the peak) at zero applied bias. Figure 3 shows the received optical power and the RF signal power vs. the laser current. The sensor's quadrature (maximum-slope) point was reached at approximately 25 mA. The discontinuity in slope at approximately 30 mA is due to crossing of the laser threshold current. The peak (zero-slope) operating point, where the sensor response becomes quadratic, was reached at approximately 45 mA. Beyond this point, the signal increased, but the increase was more gradual than the drop, due to saturation of the PV output voltage.

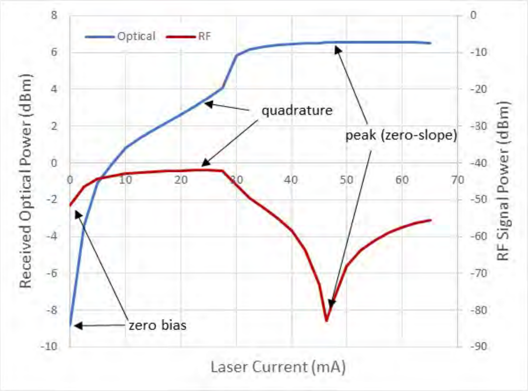

Figure 3. Received optical power and RF signal power vs. 980 nm laser current.

Figure 4 shows the measured output signal with zero bias applied, at the quadrature point, and at peak optical transmission (i.e. zero-slope point). An improvement of 10 dB was achieved at the quadrature point relative to the zero-bias point.

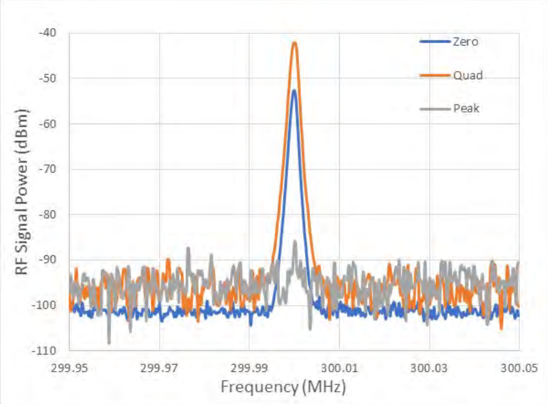

Figure 4. Sensor output signal at zero bias, at the quadrature point, and at the peak (zero-slope) operating point.

5. Conclusions

The use of a photovoltaic power-over-fiber module to adjust the bias point of a LiNbO$_3$ MZI electric field sensor has been demonstrated. This technique can be used to enhance sensor response by operating at a more favorable point on the MZI transfer function, as well as stabilize the sensor response against environmental fluctuations. In this demonstration, PoF active biasing was shown to compensate drifts over the entire characteristic Vpi range of the sensor. An improvement of 10 dB in sensor response was achieved by optimizing the operating point.

This initial proof-of-concept demonstration used a commercially available power-over-fiber photovoltaic element in a metallic package. Future work will focus on integration of a bare photovoltaic chip within the dielectric sensor package to virtually eliminate any field perturbing effects of the PoF element.

References

[1] Capozzolli, A., Curcio, C., D'Elia, G., Liseno, A., and Vinetti, P., Photonic Probes and Advanced (also Phaseless) Near-Field Far-Field Techniques, IEEE Antennas and Propagation Mag., 52 (5), 232-241.

[2] Walkenhorst, B., Rodriquez, V., Toney, J. and Fordham, J., Characterization of a Photonics E-Field Sensor as a Near-Field Probe, 39th Annual Meeting and Symposium of the Antenna Measurement Techniques Association, Atlanta, Oct. 15-20, 2017.

[3] Cho, P.S., Bias Control Techniques In: Broadband Optical Modulators, chapter 15, pp. 363-382; Chen, H. and Murpy, E.J. editors; Boca Raton, FL: CRC Press, 2012.

[4] Betts, G.E., Johnson, L.M., Cox, C.H., Optimization of Externally Modulated Analog Optical Links, Proc. SPIE 1562, Devices for Optical Processingd, San Diego, July 21, 1991.

[5] Toney, J.E., Lithium Niobate Photonics, pp. 106-108; Norwood, MA: Artech House; 2015.

[6] *ibid.*, pp. 192-193.

[7] Photonic Systems Inc. product information. Available at http://www.photonicsinc.com/modulator_bias_controller.html

[8] Pharad, LLC product information. Available at http://www.pharad.com/modulator-bias-controller.html

[9] Sriram, S. and Kingsley, S., Sensitivity Enhancements to Photonic Electric Field Sensor, Proc. SPIE 5435, Enabling Photonic Technologies for Aerospace Applications VI, Orlando, April 12, 2004.

Broadband Horn Antenna Calibration Using Optical Fiber Link Port Extender for Vector Network Analyzer

Sayaka MATSUKAWA[1*], Satoru KUROKAWA[1], Masanobu HIROSE[1*], Michitaka AMEYA[1], Yuanfeng SHE[1*], Yoshikazu TOBA [2], Masatoshi ONIZAWA [2], and Jun ICHIJO [2]
[1] National Institute of Advanced Industrial Science and Technology, Tsukuba, Ibaraki, 305-8563 Japan
[2] SEIKOH GIKEN Co.,Ltd., Matsuhidai, Maysudo, Chiba, 270-2214, Japan

*Corresponding author: sayaka-matsukawa@aist.go.jp

Abstract – We have developed a microwave measurement system using optical fiber link transceivers for a vector network analyzer. Our proposed system can extend the ports of the VNA by using optical devices and optical fibers. Further, it can measure S-parameters in a full 2-port calibration up to 4GHz. In order to validate our system, we demonstrate antenna property measurement for double ridged guide horn antenna. Difference of estimated antenna gain between using our proposed system and using coaxial cables is less than 0.3 dB from 1 GHz to 3.5 GHz.

Keywords – Vector network analyzer; Broadband antenna; Double ridged guide horn antenna; Antenna gain; Radio over fiber;

1. Introduction

We have already proposed the bi-directional type optical fiber link transceiver that can extend the port of vector network analyzer (VNA) [1][2][3]. Our system can replace the coaxial cables to optical fiber cables. Further, it can eliminate the unwanted influence of coaxial cables and decrease the attenuation of microwave signal.

In this paper, we explain the antenna measurement results using our proposed optical fiber link port extender of VNA. At first, we explain the outline of our proposed system. Second, we explain the antenna measurement results for double ridged guide horn antenna. Finally, we compare with the estimated antenna gain between using our transceiver and using the coaxial cables.

2. Outline of Bi-Directional Type Optical Fiber Link Transceiver

Our proposed bi-directional type optical fiber link transceiver can extend a port of VNA. It can measure S-parameters of microwave device under measurement in full 2-port calibration of VNA. In this section, we explain the outline of our proposed optical fiber link system. Figure 1 shows the outline of our system with VNA. Figure 2 shows a photo of our proposed system with VNA. Figure 3 shows the linearity of the system. In the case of attenuation is less than equal 60 dB, linearity of the system is less than 0.1 dB in the frequency range from 100 MHz to 4 GHz.

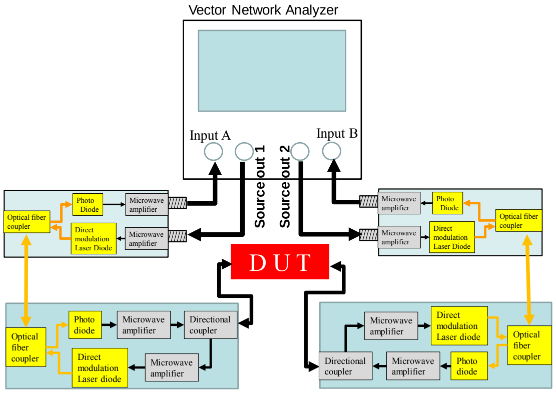

Figure 1. Our newly proposed optical fiber link port extender with VNA

Figure 2. Photo of Our newly proposed optical fiber link port extender with VNA

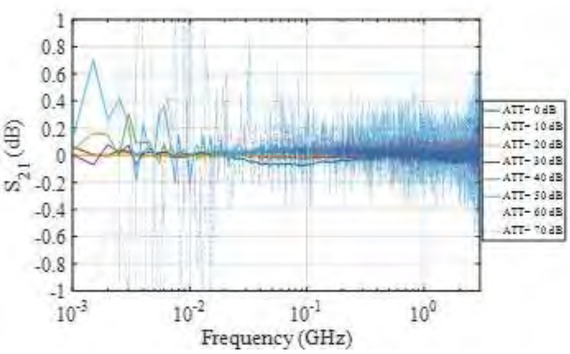

Figure 3. S_{21} linearity of the system

3. Antenna Gain Measurement for Double Ridged Guide Horn Antenna

In order to demonstrate the validity of our proposed optical fiber link transceiver with VNA, we carry out the antenna gain measurement of double ridged guide horn antenna (DRGH) 3115 of ETS-Lindgren Inc. [4] in full 2-port calibration of VNA. Two DRGH set face to face with the variable distance from 3 m to 5 m. S-parameters ($S_{11}(\omega)$, $S_{21}(\omega)$, $S_{12}(\omega)$, $S_{22}(\omega)$) are measured by our proposed system with VNA. Figure 4 , 5 and 6 show the outline of measurement setup, measured $S_{21}(\omega)$ magnitude and measured $S_{11}(\omega)$ magnitude.

Then we estimate the antenna gain $G(\omega)$ using Friis transmission formula [5] and three antenna method with fixed antenna face to face distance.

Figure 7, 8 and 9 show the estimated antenna gain using our system with VNA, using 10m coaxial cables with VNA and difference of estimated antenna gain between them. Difference of estimated antenna gain between them is less than 0.3 dB in the frequency range from 1 GHz to 3.5 GHz and is less than 1.0 dB in the frequency range from 0.5 GHz to 4 GHz.

4. Conclusion

We have proposed the optical fiber link port extender for VNA. It can measure S-parameters for microwave devices and antennas in full-2-port calibration of vector network analyzer. In order to validate our proposed system, we carry out the antenna gain measurement for double ridged guide horn antenna using Friis transmission formula and three antenna method. Difference of the estimated antenna gain between using our proposed system and using the coaxial cables with VNA is less than 0.3 dB in the frequency range from 1 GHz to 3.5 GHz. These results show the fact that our proposed system can measure *S*-parameters of antenna under test up to 3.5 GHz.

References

[1] M. Hirose, S. Kurokawa, K. Komiyama, ``Antenna Measurements by One-Path Two-Port Calibration Using Radio-on-Fiber Extended Port Without Power Supply, '' IEEE Trans. Instrum. Meas., vol.56, no. 2, pp. 397-400, Apr. 2007.

[2] S. Kurokawa, M. Hirose, Y. Toba, J. Ichijo`` Antenna Measurement system Using Bi-directional Optical Fiber Link system,'' in Proc. of EuMW 2016, Oct. 2016.

[3] S. Kurokawa, M. Hirose, Y. Toba, M. Onizawa, and J. Ichijo, ``Antenna Gain Estimation for a Single Antenna Measurement Using Bi-directional Optical fiber link transceiver,'' in Proc. of 2016 IEEE CAMA, Oct. 2016.

[4] 3115 Double ridged guide horn antenna. ETS-Lindgren Inc. http://www.ets-lindgren.com/3115

[5] R. E. Collin, Antennas and Radiowave Propagation, McGraw-Hill, pp. 303-304, 1985.

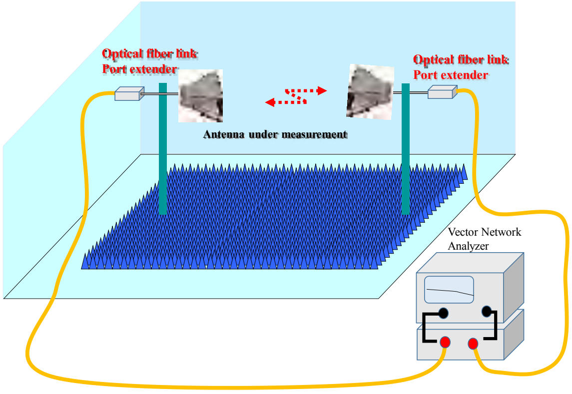

Figure 4. Antenna measurement setup for double ridged guide horn antenna using our proposed system

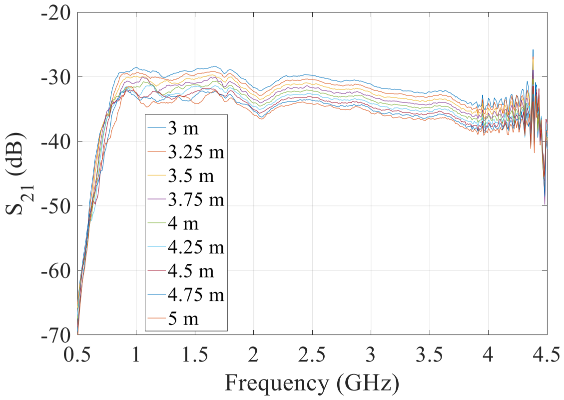

Figure 5. Measured frequency domain $S_{21}(\omega)$ magnitude

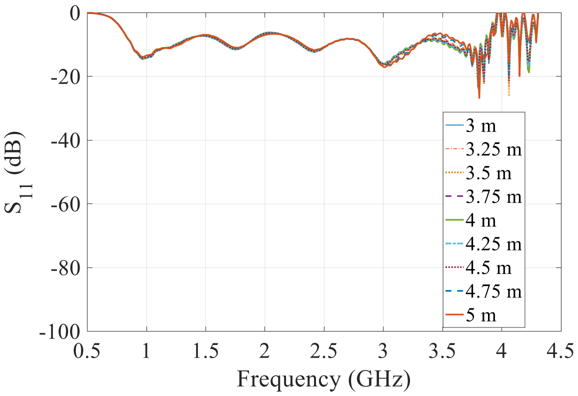

Figure 6. Measured frequency domain $S_{11}(\omega)$ magnitude

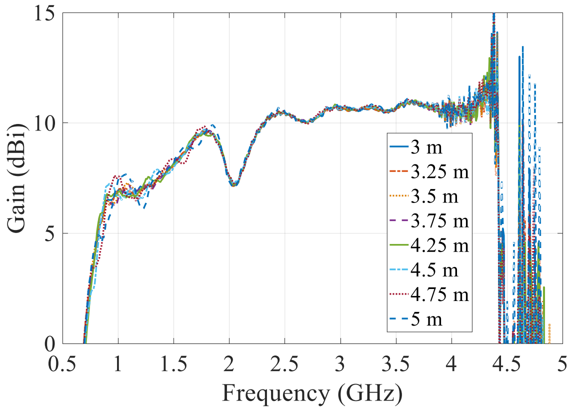

Figure 7. Estimated antenna gain of double ridged guide horn antenna using our proposed optical fiber link transceiver with VNA

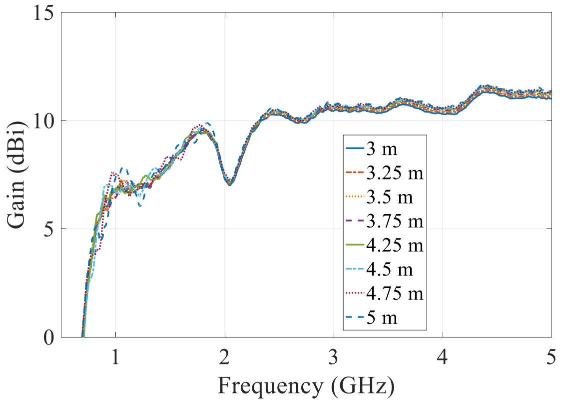

Figure 8. Estimated antenna gain of double ridged guide horn antenna using our 10 m coaxial cables with VNA

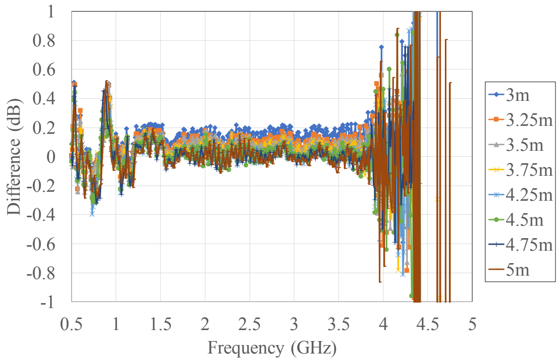

Figure 9. Difference of Estimated antenna gain between them

Antenna Design for Electric/Optical Sensors with High Sensitivity

Qiang CHEN

Department of Communications Engineering, Tohoku University, Sendai, Japan

chenq@ecei.tohoku.ac.jp

Abstract – An approach for designing antennas for Electric/Optical (E/O) sensors is introduced to develop an E/O measurement system with high position resolution and high sensitivity. The E/O measurement device including optical modulator, demodulator and active circuit is regarded as a 2-port equivalent circuit, and the scattering matrix of the equivalent circuit is obtained from measurement. The antenna is designed to make a trade-off between the sensitivity and the frequency bandwidth based on the scattering matrix. Performance of the designed antenna is demonstrated by experiment.

Keywords – Antenna; Small Antenna; Electric/Optical Sensor; Sensitivity; Impedance matching

1. Introduction

The problem of electromagnetic interference between electrical circuits and devices is becoming more and more serious because the clock frequency of the electrical circuits is increasing rapidly, and high-density packaging and multilayer printed circuit board (PCB) technologies are widely applied to PCB design. When a problem occurs in an electrical device, it is necessary to know in advance the near-field distribution of the electrical device in order to identify the location where the undesired electromagnetic wave is being radiated. The near-field distribution is usually measured directly by a small probe antenna. However, scattering of the metal cable of probes causes a interference problem and degrades the measurement accuracy largely.

Measurement of electromagnetic field using Electric/Optical (E/O) sensors has been studied for a long time [1]-[11]. Because the metal cable is placed by a optical fiber, the electromagnetic interference between the probe and the measured devices can be reduced largely and the measurement accuracy can be improved greatly. However, this method has a problem of low sensitivity. It is required to increase the sensitivity while keeping the low interference.

In this report, an approach for designing antennas for E/O sensors is introduced to develop an E/O measurement system with high position resolution and high sensitivity. The E/O measurement device including optical modulator, demodulator and active circuit is regarded as a 2-port equivalent circuit, and the scattering matrix of the equivalent circuit is obtained from measurement. The antenna is designed to make a trade-off between the sensitivity and the frequency bandwidth based on the scattering matrix. Performance of the designed antenna is demonstrated by experiment.

2. Equivalent Circuit

It is supposed to design a dipole antenna for E/O sensor using $LiNbO_3$ crystals. The dipole antenna is used to measure the near electric-field.

The measurement system using the E/O sensor is composed of probe antenna, optical modulator, demodulator, active circuit, and spectrum analyzer. Equivalent circuit of the sensor system is shown in Fig. 1, where V_0 is open voltage of the antenna, Z_a is input impedance of antenna, Γ_a is reflection coefficient between antenna and transmission line, Z_l is input impedance of spectrum analyzer, usually 50Ω. Γ_{in} is the

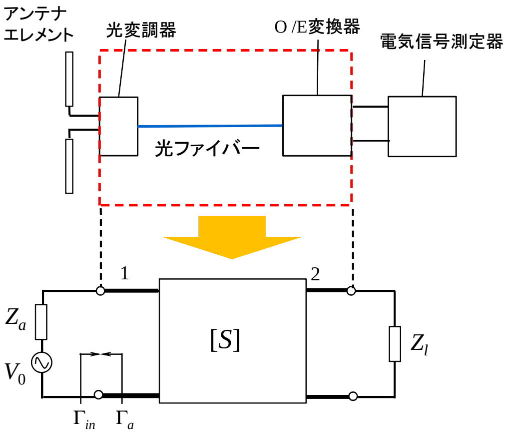

Figure 1. Equivalent circuit of measurement system using E/O sensors.

reflection coefficient at port 1,

$$\Gamma_{in} = S_{11} \tag{1}$$

when the impedance matching condition is satisfied at Port 2. In this case, the power consumed in Z_l is

$$P_l = \frac{1-|\Gamma_a|^2}{|1-\Gamma_a\Gamma_{in}|^2}|S_{21}|^2 P_{inc} \tag{2}$$

where R_a is the real part of Z_a , and P_{inc} is

$$P_{inc} = \frac{V_0^2}{4R_a} \tag{3}$$

The maximum P_l is obtained when the impedance matching condition

$$\Gamma_a = \Gamma_{in}^* \tag{4}$$

is satisfied. Then,

$$P_l = \frac{1}{1-|\Gamma_{in}|^2}|S_{21}|^2 P_{inc} \tag{5}$$

2.1 Antenna Design

Fig. 2 shows the antenna we designed for the E/O sensor. Fig. 3 shows the input impedance of the designed antenna which satisfies the impedance matching condition at about 1 GHz. Figure 4 shows the receiving power using the designed monopole compared with that of the conventional monopole antenna. The receiving power was increased about 17 dB at the operation frequency. It is also found that the operation bandwidth became narrower than that of normal monopole, indicating the trade-off design is required in the practical applications.

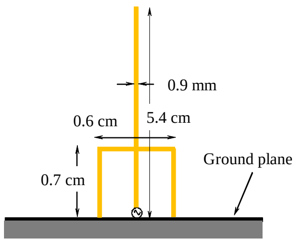

Figure 2. Monopole type of proposed antenna.

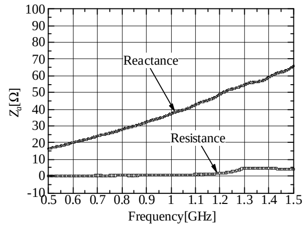

Figure 3. Input impedance of proposed antenna.

3. Summary

An approach for designing antennas for Electric/Optical (E/O) sensors was introduced to develop an E/O measurement system with high position resolution and high sensitivity. Receiving power of the sensor using the designed antenna was increased about 17 dB in a design example. It was shown that a trade-off consideration

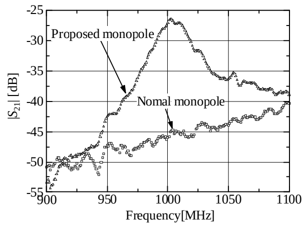

Figure 4. Received power of proposed monopole antenna and nomal monopole antenna.

is required between the sensitivity and the bandwidth in the practical applications.

References

[1] E. B. Larsen, J. R. Andrews, and E. E. Baldwin, "Sensitive isotropic antenna with fiber-optic link to a conventional receiver," Nat. Bur. Stand., Washington, DC, Rep. NBSIR 75-819, Sept. 1976.

[2] H. I. Bassen and R. J. Hoss, "An optically linked telemetry system for use with electromagnetic-field measurement probes," *IEEE Trans. Electromag. Compat.*, vol. EMC-20, pp. 483-488, 1978.

[3] H. Bassen, W. Herman, and R. Hoss, "EM probe with fiber optic telemetry system," *Microwave J.*, pp. 35-47, Apr. 1977.

[4] K. Munter, "An isolated sensor determining the Poynting vector in the near field of a radiating antenna,"*Conf on Precision Electromagnetic Measurements*, Boulder, CO, IEEE Cat. 82, CH 1737-6, June 1982, pp. P-14-P-15.

[5] H. Bassen and R. Peterson, "Complete measurement of electromagneticfields with electro-optical crystals," *Biological Egects of Electromagnetic Waves*, Selected Papers of USNU/URSI Annu. Meet.,1975, HEW publication (FDA) 77-8011, pp. 310-323, 1975.

[6] C. H. Bulmer, W. K. Burns, and R. P. Moeller, "Linear interferometric waveguide modulator for electromagnetic-field detection," *Opt.Lett.*, vol. 5, p. 176, 1980.

[7] S. K. Yao, T. Findakley, R. Cordero-Iannerella, S. Thaniyavarn, G.Hayward, and B. Chen, "Electromagnetic sensor using integrated optic channel waveguide modulator and polarization preserving fibers,"*Fiber Optic and Laser Sensors*, Emery L. Moore, O. Glenn Ramer, Ed., in Proc. SPIE, vol. 412, pp. 178-184, 1983.

[8] J. C. Wyss and S. T. Sheeran, "A practical optical modulator and link for antennas", *IEEE Journal of Light Wave Tech.*, vol. LT-3, No.2, pp. 316-321, 1985.

[9] V. B. Baglikov, R. Yu. Dolinin, E. M. Pelekhatyi, and R. F. dvlykaev,"Investigation of an electric field sensor based on an integr cd optical Mach-Zehnder modulator," *Sov. J. Quantum Electron.*, vol. 5, no. 10, pp. 1353-1355, Oct. 1988.

[10] C. H. Bulmer and S. C. Hiser, "Linear Ti:LiNb$_3$ Modulator it 1.3 pm for electromagnetic field sensing." *Integrated Optical Circuit Tran.*, SPIE, vol. 517, pp. 177-185. 1984.

[11] N. Kuwabara, K. Tajima, R. Kobayashi, and F.Amemiya, " Development and analysis of electric field sensor using LiNbO$_3$ optical modulator", *IEEE Transaction on Electromagnetic compatibility*, vol.34, no.4, pp.391-396, Nov. 1992.

This manuscript was made as a handout of the PEM2017 workshop, but not as a paper. The contents of the manuscript are collected from the published papers of the present author.

Photonic Measurement Technology for Electrically Small Antennas

Myles CAPSTICK[1*], Sven KUEHN[1], and Niels KUSTER[1,2]
[1]Foundation for Research on Information Technologies in Society (IT'IS), 8005 Zurich, Switzerland
[2] Swiss Federal Institute of Technology Zurich (ETHZ), 8092 Zurich, Switzerland
*Corresponding author: capstick@itis.ethz.ch

Abstract – In this paper, we describe in detail a low-perturbation method for measuring complex impedance for which full calibration of the measurement device can be achieved. The apparatus for measurement of electrically small antennas employs miniature photonically powered radio-frequency over fiber links to ensure that the electrical footprint of the measurement device is minimized. The challenge to achieve accurate measurement of electrically small antennas for communications bands up to 6 GHz is demonstrated, along with the ease of obtaining erroneous results for the impedance and resonant frequency when traditional methods are used.

Keywords – complex impedance measurement, electrically small antennas, optical coupling, radiofrequency over fiber links

1. Introduction

Modern wireless devices such as mobile phones and tablets support ever more standards across wider frequency ranges, with an increasing number of antennas integrated, requiring that the antennas be electrically small. The large vector network analyzers (VNAs) used at the frequency range applicable to portable wireless devices must be connected via coaxial cables, and methods for connection of an antenna directly to a VNA result in widely different and uncontrolled electrical sizes. The difficulties of making antenna measurements and the sorts of errors that can be encountered when a coaxial cable is connected to a small device are discussed in detail in [1] and [2]. The approaches used by experimenters (traps, chokes, ferrites, or other methods) to minimize the impact of cabling [3] introduce errors of varying and unknown magnitude. Methods proposed to allow antenna impedance to be indirectly measured [4] require special circuitry integrated in a device to perform the measurement, and the sensing antenna must be positioned close to the antenna under test (AUT). An experimental transmitter and method to measure the magnitude of the reflection coefficient of an antenna with a phase-locked loop voltage-controlled oscillator (PLL VCO) and directional coupler integrated into the portable device has been described [5]; an optical fiber link was used for the PLL reference frequency (10 MHz), and the measured return loss magnitude could also be conveyed optically to a computer, but impedance measurement was not possible. A hybrid fiber-optic system for measurement of radiofrequency (RF) reflection based on an external signal generator and fiber radio link to provide the RF source for the reflectometer has been described ([6] and [7]) and a patent application submitted [8]; log detectors capture the reflected signal, and a further optical link to a computer gives the reflection measure. This is, however, only a single-port scalar network analyzer, and the device is not small enough for integration into portable devices. A battery-operated optical extension for a VNA with a circulator rather than a directional coupler to separate forward and reverse signals, thereby limiting the frequency range to 700–1000 MHz, that could measure antenna impedance has been produced [9], but at 80 × 40 × 20 mm, is also too large to fit inside modern portable devices. Optical links described by others to measure the gain of small antennas [10] are large in comparison to modern wireless devices. Optical fibers that extend over the distance at which measurements can be performed have been proposed [11], but these also do not address the requirement of being electrically small.

The measurement device outlined in this paper represents an advance relative to the device reported in [12]. It is operated in conjunction with a two-port VNA (or signal source and vector measurement receiver) connected with only three optical fibers to the remote unit and VNA. The conductive part of the measurement head, only 9 × 9 × 4 mm, is electrically small enough to impose little impact for any but the most miniature of devices. A standard open-short-load protocol for calibration is presented together with expressions to use calibration standard data to correct experimental measurements.

2. Methods

A schematic diagram of the new measurement system configured for use with a VNA, shown in Figure 1, includes two RF-over-fiber (RFoF) links – one each for the forward and reverse directions (nominal power 1 mW) – and an optical power fiber link (~35 mW) to power a photovoltaic cell and remote circuitry. Forward signals from port 1 of the VNA, modulated on a direct current (DC) biased vertical cavity surface emitting laser (VCSEL) and transmitted over an optical fiber to the remote VNA head, are demodulated via reverse biased photo diode with 50 Ω bias resistor output impedance. The signals for excitation along the forward path of the remote head connect to the through line of the chip directional coupler via one of three MCE-15A connectors (Sunridge Corp., Taipei, Taiwan). The output of the through line connects to the AUT or measurement standards that allow calibration of the system, also via MCE-15A. The reflected power from the reflection port of the directional coupler is amplified and modulates the current through a VCSEL for transmission back to the base unit for demodulation and transmission to port 2 of the VNA.

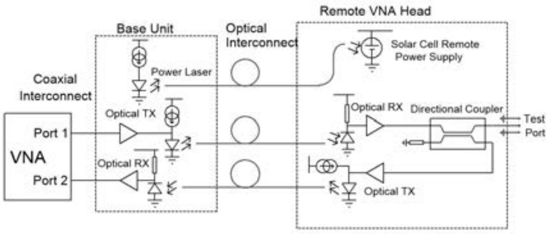

Figure 1. Schematic diagram of the measurement system.

Calibration of the device involves measurement of three known impedances – typically open, short, and a matched load with known S-parameters – such that the three unknown error correction terms can be determined. These standards of known complex impedance are measured, and the S21 measurement results are collected from the VNA for each standard. The output port is then connected to the AUT, and S21 data is collected. The correction parameters are calculated and applied to the antenna measurement data. It is then possible to consider any other parameter of interest, such as the influence of the hand, head, or body on antenna impedance with no interfering measurement interconnections.

A. Error Correction. Error correction here is based on standard terms modified for the two-path case, i.e., the two fiber radio links. The full signal flow diagram shown in Figure 2 can be simplified, as the fiber radio links are unidirectional, to provide the standard one-port error model shown in Figure 3, where e00 is the directivity error, e11 is the source match error, and e10.e01 is the reflection tracking error.

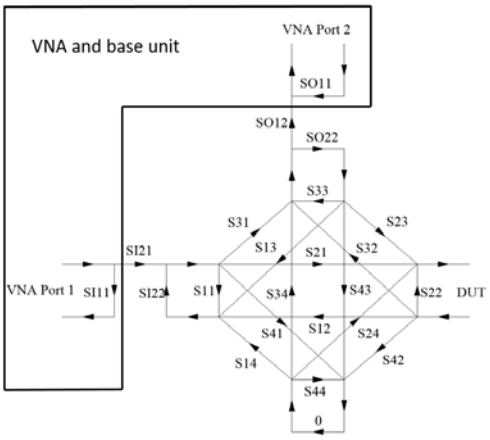

Figure 2. Signal flow diagram of the measurement device.

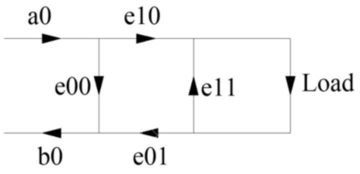

Figure 3. Error model after simplification.

For any load with reflection coefficient G_A, the uncalibrated/uncorrected device measures a reflection coefficient G_M:

$$G_M = \frac{e00 + (e10 \cdot e01) \cdot G_A}{(1 - e11 \cdot G_A)} \qquad (1)$$

Simultaneous solution of a measurement of three known standards allows e00, e11, and e10.e01 to be determined.

3. Results

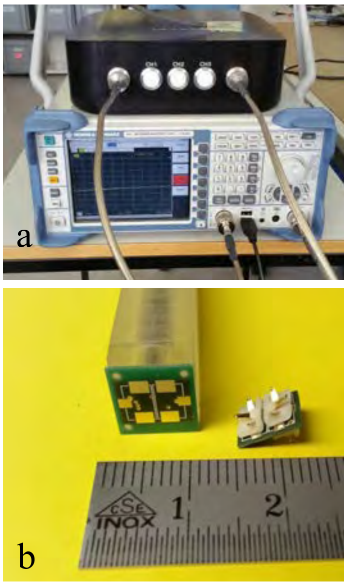

Figure 4. Optically coupled measurement device. a) Base unit and network analyzer; b) optical head, input and output ports, and directional coupler board with compression connectors; ruler numbering in cm with mm tick marks.

A. Measurement Device. The optically coupled antenna impedance measurement device prototype is shown in Figure 4; with the directional coupler included, the device covers the 1.5–3.5 GHz frequency range. The device was calibrated with nominal open, short, and 50 Ω loads, and error terms were determined.

B. Validation. Three known impedances were measured: 82 Ω in parallel with 1 pF, 120 Ω in parallel with 3.9 nH, and 20 Ω. The expected and measured values are shown in the Smith chart plots in Figure 5, where it can be seen that there is excellent agreement between actual and measured values for the phase and good agreement for the amplitude.

C. Bluetooth Antenna. A meandered inverted F antenna (IFA) was designed and fabricated to test the optically coupled VNA measurement head and illustrate the difficulties of measuring real antenna impedances via direct VNA connection. The antenna dimensions are shown in Figure 6; the overall electrical size of the antenna and ground plane is 25 × 30 mm with a ca. 10 mm extension due to an end fire SMA connector at the end of the microstrip feed line. The antenna was simulated with SEMCAD X Matterhorn, and the frequency response and impedance are shown in Figure 7.

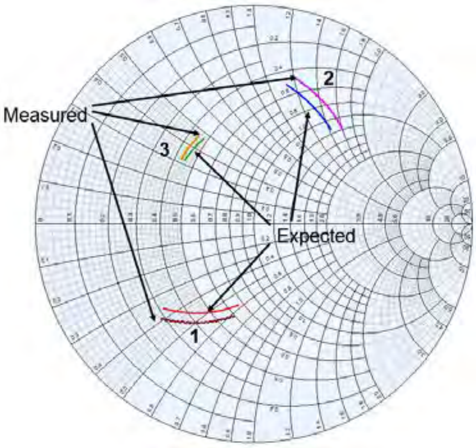

Figure 5. Measured and expected impedances of the validation loads.

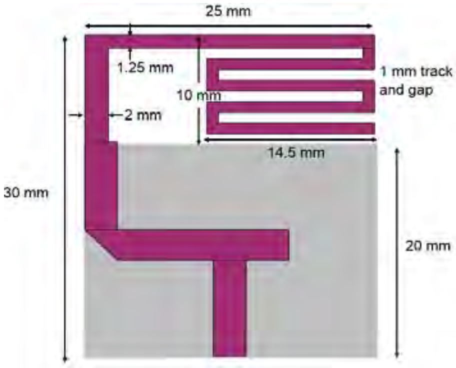

Figure 6. IFA and ground plane dimensions; 1.2 mm FR4 substrate; the matching stub is 5.1 mm long from the center of the T; microstrip lines are 50 Ω.

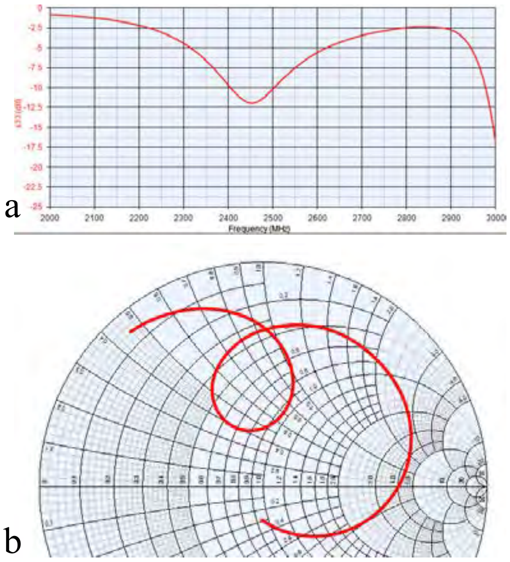

Figure 7. Simulated a) frequency response and b) impedance of the bluetooth antenna.

D. Direct Measurement of the Antenna with a VNA. Figure 8 shows the responses obtained with the antenna connected directly to port 1 of the VNA or with varying lengths of coaxial

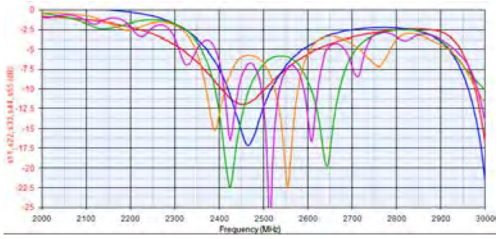

Figure 8. Possible response magnitudes of the bluetooth antenna reflection coefficient measured via connection to a VNA either directly or with coaxial cables 0 (blue), 30 (green), 50 (orange), and 100 cm (magenta) long.

cable, calibrated to the end, running directly away from the VNA. The response complexity increases with electrical size of the counterpoise, due to increasing cable length, illustrates the difficulties in measuring small antennas. The complexity of the frequency response is due not to reflections in the cable (each is individually calibrated) but to the increase in electrical size and the currents flowing along the outer perimeter of the cable. Although the addition of ferrite clamps to the cable close to the antenna improves the situation, it remains unclear how much improvement has been afforded.

E. Measurement of the Antenna with the Optical VNA Head. The optical VNA head is relatively small electrically, only 9 × 9 × 4 mm including the directional coupler board, though large enough to allow the optical fibers to be connected and supported. The all dielectric remaining materials have limited influence on performance. The measurement of the antenna with substrate required that appropriate footprint pads be included, and the connection frame was glued to the substrate for alignment and interconnection (Figure 9); a sharp scalpel was used to cut the line connecting the SMA. An additional length of 50 Ω line was added between the interconnection point for the optical VNA head and the connector; the additional phase shift is removed mathematically to bring the phase reference for both measurement sets to the same location. The optical head and VNA combination were calibrated with the known open, short, and matched loads, and the error terms were determined.

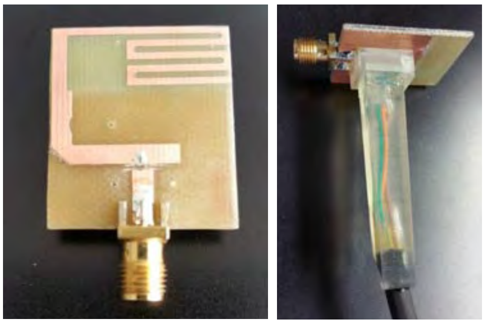

Figure 9. The antenna and the optical head connected to the antenna.

Figure 10 shows the antenna as measured by the optical VNA head; the simulation and measurement at the fundamental frequency are in good agreement. The resonance at 3 GHz is shifted by <0.5%, but this may be because the antenna was manufactured by milling away the copper and some of the top surface of the substrate; also, the internal corners are curved rather than right angled. More importantly, as the current through the return RF link laser diode is not stabilized, the amplitude is sensitive to temperature, particularly when handled; changes of up to 1 dB were common. An 0.8 dB correction of the baseline return loss improves the match between simulation and measurement, which is more in line with observations made with direct VNA connections remote from the resonance.

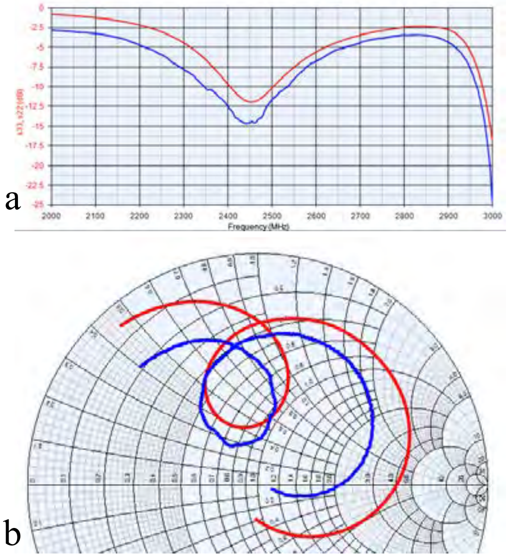

Figure 10. a) Reflection coefficient of the antenna and b) impedance as measured with the new device; red: simulation, blue: measurement.

4. Conclusions

An optically coupled add-on to an existing VNA or vector measurement system was designed and tested. The device has a very small electrical footprint for low perturbation measurement of electrically small antennas. The calibration method developed and implemented provides good performance. The dynamic range is adequate even for cases of low reflected power. Although the stability of the output power level of the return link laser diode could be improved to boost performance and accuracy, the device represents a useful measurement tool.

References

[1] Kotterman WAT, Pedersen GF, Eggers P. Cable-Less Measurement Set-Up for Wireless Handheld Terminals. Personal, Indoor and Mobile Radio Communications Conference, Sep 30–Oct 3, 2001, San Diego CA, USA, pp. B112–B116.

[2] Yanakiev B, Nielsen JO, Pedersen GF. On Small Antenna Measurements in a Realistic MIMO Scenario. Fourth European Conference on Antennas and Propagation, EuCAP, Apr 12–16, 2010, Barcelona, ES, pp.1–5.

[3] Icheln C. Krogerus J., Vainikainen P. Use of Balun Chokes in Small Antenna Radiation Measurements. IEEE Trans. Instrum. Meas. 2004; 53(2): 498– 506.

[4] Capstick MH, Jekkonen JO, Marvin AC, Flintoft ID, Dawson L. A Novel Indirect Method to Determine the Radiation Impedance of a Handheld Antenna Structure. IEEE Trans. Instrum. Meas. 2009; 58(3): 578–585.

[5] Eskelinen P. Introduction to RF Equipment and System Design, Artech House, Inc. Norwood MA, USA, pp. 228–229; 2004.

[6] Clow N., Morrow I.L. ESA measurements using the Hybrid Fibre-Optic Reflection Measurement System. Antennas & Propagation Conference LAPC, Nov 16–17, 2009, Loughborough, UK. pp. 793–796.

[7] Clow N, Morrow I.L. Towards the Development of Electrically Small Antenna Measurements Systems Technology, Antenna Applications Symposium, Sep 22–24, 2009, Monticello Il, USA, pp. 16–39.

[8] Clow N., Perkins SJ, Morrow IL. Hybrid Reflectometer System (HRS). WIPO Patent Application WO/2011/023933, 2011.

[9] Fukasawa T, Shimomura K, Ohtsuka M, Makino S, Accurate and Effective Measurement Method for Small Antenna using Fiber-Optics, in Proc. International Union of Radio Science (URSI), Oct. 2005.

[10] Alexander M, Hong Loh T, Betancort AL. Measurement of Electrically Small Antennas via Optical Fibre. Antennas & Propagation Conference LAPC, Nov 16–17, 2009, Loughborough, UK, pp. 653-656.

[11] Keysight Technologies, "Extending the Measurement Plane up to 1 km in Vector Network Analysis", http://literature.cdn.keysight.com/litweb/pdf/5991-1828EN.pdf

[12] Capstick, Myles, Sven Kuehn, and Niels Kuster. "Low perturbation measurement of electrically small antennas." 2016 10th European Conference on Antennas and Propagation (EuCAP). IEEE, 2016.

Accurate Frequency Measurement of Terahertz Radiations by Electrooptic Sampling Using a Modulator-Based Optical Comb Generator for Frequency Stabilization of CW-Terahertz Sources

Isao MOROHASHI[1*], Mayu KIRIGAYA[2], Ikufumi KATAYAMA[2], Yoshihisa IRIJMAJIRI[1], Takahide SAKAMOTO[1], Norihiko SEKINE[1], Akifumi KASAMATSU[1], and Iwao HOSAKO[1]

[1]National Institute of Information and Communications Technology, 184-8795 Tokyo, Japan [2]Yokohama National University, 240-8501 Kanagawa, Japan

*Corresponding author: morohashi@nict.go.jp

Abstract – We propose a method for phase-locking of THz sources by electro-optic sampling (EOS) using optical combs and demonstrated accurate frequency measurement of THz waves as a first step of the phase-locking. By using an EOS system with a Mach-Zehnder-modulator-based flat comb generator (MZ-FCG), frequency measurement of a 600 GHz-band signal was successfully demonstrated.

Keywords – optical comb; terahertz wave; Mach-Zehnder modulator

1. Introduction

With recent progress in semiconductor device fabrication technologies, oscillators operating in the terahertz (THz) frequency range such as quantum cascade lasers and resonant tunneling diodes are available, and then being applied to remote sensing and wireless communications. The linewidth of such devices is generally few megahertz, which does not fulfill that required in the applications mentioned above, so that they need to be stabilized by phase locked loop techniques. Thus, electric field measurement is also important in the THz range. For the phase locking of the THz oscillators, frequency mixers are generally used. However, the frequency mixers have a limited bandwidth. On the other hand, electro-optic sampling (EOS) is capable of broadband detection in the range from microwave to THz waves in room-temperature [1-3]. In this paper, we propose a method for frequency stabilization of THz sources and demonstrate accurate frequency measurement of THz waves based on EOS using a Mach-Zehnder-modulator-based flat comb generator (MZ-FCG).

2. Basic Concept of Frequency Control by Optical Combs

Figure 1 shows the basic concept for frequency stabilization of cw-THz sources. This method is based on optical heterodyne, where optical combs are used as the local oscillator and an EO crystal acts as the mixer. When an optical comb with a mode spacing of f_{rep} is input to the mixer, it is down-converted from the optical domain into the THz domain, creating a THz comb which covers the frequency range from DC to the THz region while preserving the mode spacing. By mixing the optical comb with an incoming THz wave, f_{THz}, the THz

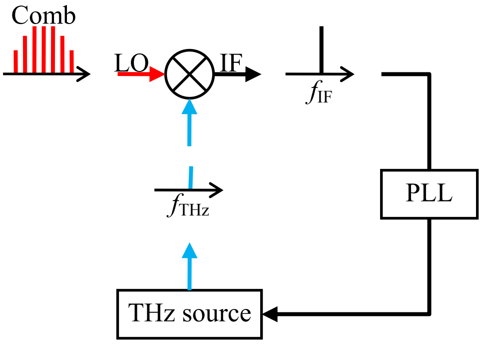

Figure 1. The schematic of frequency stabilization of THz sources by EOS using the MZ-FCG.

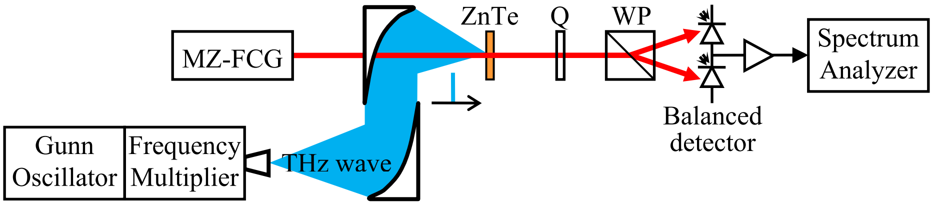

Figure 2. The experimental setup for the frequency measurement of a 600 GHz-band signal. Q: quarter-wave plate, WP: Wollaston prism.

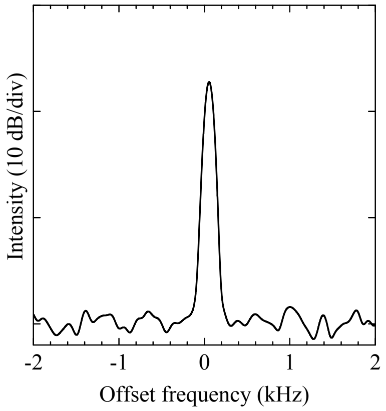

Figure 3. A spectrum of a THz signal with a frequency of 624 GHz.

wave is down-converted to the RF region, outputting an intermediate frequency (IF) signal. By feeding back the IF signal as the error signal to the THz source through PLL systems, the THz source is locked to the optical comb.

3. Accurate Frequency Measurement of THz Waves

As a first step to accomplish the phase-locking of THz sources, accurate frequency measurement of THz waves using the EOS is important. By adopting an optical-modulator-based comb source as an optical local signal, highly accurate spectrum measurement can be realized. Thus, we used the MZ-FCG as the LO source in the optical heterodyne system. Figure 2 shows the setup for EOS-based frequency measurement system using the MZ-FCG.

The THz source was composed of a Gunn oscillator and a frequency multiplier chain, which emits a signal with a frequency of 624 GHz. On the EO crystal, 10 GHz-spaced optical combs generated by the MZ-FCG [4] are modulated by the THz signal, which creates optical sidebands. By detecting the modulated optical comb using a balanced photodetector and a spectrum analyzer (SA), spectra of THz signals are observed.

Figure 3 shows a spectrum of a detected THz signal. In this case, the frequency of rf signal driving the MZ-FCG was set to which the frequency difference between the THz wave and the corresponding comb modes ($\Delta f = f_{\mathrm{THz}} - 63 f_{\mathrm{rep}}$) was 100 kHz. An extremely sharp line was successfully observed. The linewidth was narrower than 1 Hz, and the signal-to-noise ratio was greater than 20 dB (at the resolution bandwidth of 100 Hz).

4. Conclusion

We proposed a method for phase-locking of THz sources by EOS, which is based on optical heterodyne using optical combs for the LO source and an EO crystal for the mixer. As a first step for the phase-locking, we demonstrated accurate frequency measurement of THz waves. By using the EOS system with the MZ-FCG, frequency measurement of a 600 GHz-band signal was successfully demonstrated.

Acknowledgements

This work is supported by "Development of electric field detection technique using broadband ultrashort pulse lasers (No. 145003103),” Strategic Information and Communications R&D Promotion Programme (SCOPE) of Ministry of Internal Affairs and Communications Japan. Also, this work is partly conducted as a part of the project “R&D on amplifier technology in 300 GHz band, in a part of R&D program on key technology in terahertz frequency bands”, funded by the Ministry of Internal Affairs and Communications, Japan.

References

[1] A. Sasaki and T. Nagatsuma, "Millimeter-Wave Imaging Using an Electrooptic Detector as a Harmonic Mixer," J. Sel. Top. Quamtum Electron., vol 6, no. 5, pp. 735-740, October 2000.

[2] S. Barbieri, P. Gellie1, G. Santarelli, L. Ding, W. Maineult, C. Sirtori, R. Colombelli, H. Beere, and D. Ritchie, "Phase-locking of a 2.7-THz quantum cascade laser to a mode-locked erbium-doped fibre laser," Nat. Photon., vol. 4, pp. 636-640, Sep. 2010.

[3] S. Hisatake and T. Nagatsuma, "Continuous-wave terahertz field imaging based on photonics-based self-heterodyne electro-optic detection," Opt. Lett., vol. 38, no. 13, pp. 2307-2310, July 2013.

[4] T. Sakamoto, T. Kawanishi, and M. Tsuchiya, "10 GHz, 2.4 ps pulse generation using a single-stage dual-drive Mach-Zehnder modulator," Opt. Lett., vol. 33, no. 8, pp. 890-892, April 2008.

Removing the Cable Effect from Antenna Radiation Pattern Measurements with a Radiofrequency-over-Fiber Link

Sven KUEHN[1,2*], Beyhan KOCHALI[1], Andrea TONINI[1], and Niels KUSTER[2,3]
[1]Schmid&Partner Engineering AG, 8004 Zurich, Switzerland
[2]Foundation for Research on Information Technologies in Society (IT'IS), 8005 Zurich,
[3]Swiss Federal Institute of Technology Zurich (ETHZ), 8092 Zurich, Switzerland
[*]Corresponding author: kuehn@itis.ethz.ch

Abstract – Radiation pattern measurements of electrically small antennas are often impaired by the connected cabling. We have numerically modelled and measured the radiation pattern of a commercially available 915 MHz reference helical antenna design. We show that a cable attached to the antenna can significantly impair the antenna radiation pattern. Our study shows that this effect can be removed by the use of an active microphotonic radiofrequency-over-fiber transducer.

Keywords – radiofrequency over fiber, antenna measurement

1. Introduction

Radiation pattern measurements of electrically small antennas are impaired by the connected feed cabling [1]. Even the use of chokes or ferrite beads cannot always fully remove these effects. To fully eliminate these effects, a radiofrequency (RF) interconnect that does not extend the electrical size of the antenna is desirable. In this paper, we show that the use of an active microphotonic RF-over-fiber transducer can remove the cable effect from antenna radiation pattern measurements.

2. Methods

We selected a commercially available helical antenna operating at 915 MHz [2]. This antenna was modelled numerically with SIM4LIFE (ZMT ZurichMedTech AG, Switzerland). In the numerical model, the antenna was modelled with and without and without the feeding cable to study its effect on the radiation pattern (Figure 1). The numerical model is validated by means of azimuthal radiation pattern measurements in a 2-D measurement system. For the isolated antenna measurements, we use an active microphotonic RF-over-fiber transducer (RFoF1P, SPEAG, Switzerland) shown in Figure 2.

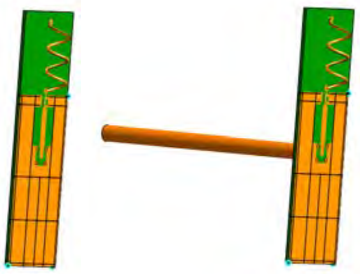

Figure 1. Numerical model of the the helical antenna, left: without feed cabling, right: with feed cabling.

The system (Figure 3) uses direct laser modulation for signal transmission of the RF signal fed to the 50Ω SMA input of the probe. The *RFoF1P* probe and the *Remote Unit* are optically linked exclusively by fiber optics. A power laser is used to illuminate a photovoltaic converter inside the probe head via the fiber optics. The electrical energy from the photovoltaic cell drives a small current-stabilized laser inside the sensor head. The input RF signal modulates the optical output power of the vertical cavity surface emitting LASER (VCSEL). This signal is then transmitted to the remote unit over an optical fiber. At the remote unit, the optical signal is demodulated again with a fast photodiode, and the RF signal received is amplified by a transimpedance amplifier and made available with a standard 50 Ω output used to connect RF equipment.

Figure 2. Helical antenna operating at 915 MHz connected to an isolating RF-over-fiber transducer and with a spectrum analyzer to remotely receive the signal.

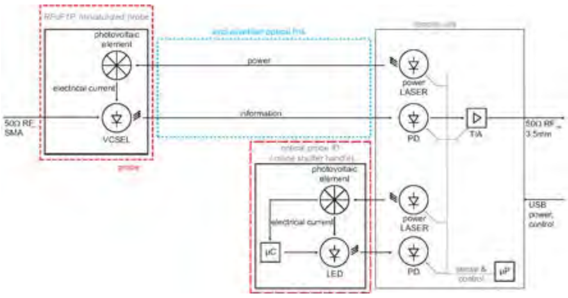

Figure 3. Schematic representation of the RFoF1P active microphotonic RF-over-fiber system.

3. Results

Figure 4 shows the test results of the antenna's radiation pattern in the azimuthal plane with and without a cable attached. It is very apparent that the RF cable has a significant effect on the antenna radiation pattern. From the results of the 3D full-wave simulation (Figure 5), it is obvious that the attachment of the conductive cable introduces a tilt in the entire radiation pattern, resulting in a large change in azimuthal plane radiation pattern.

4. Conclusions

We show that an attached RF coaxial cable can significantly impair the radiation pattern of electrically small antennas in comparison to the isolated case. As electrically small antennas are very commonly used in mobile and body-worn devices, this impairment poses a significant challenge to designers developing prototype antennas. In this study, we propose the use of an active microphotonic RF-over-fiber transducer to eliminate the effect of the cable. Final experimental validation results will be presented.

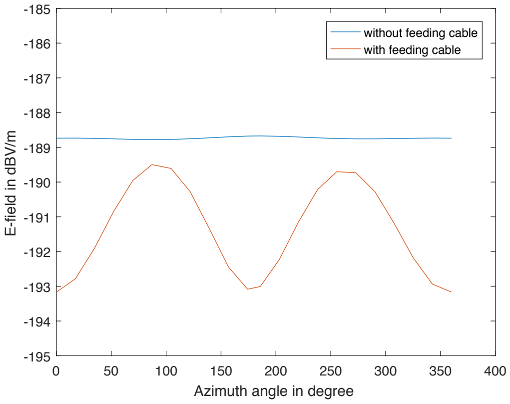

Figure 4. Azimuthal radiation pattern of the 915 MHz antenna with a traditional RF coaxial cable connected (red) and in the isolated case without the feed cable (blue).

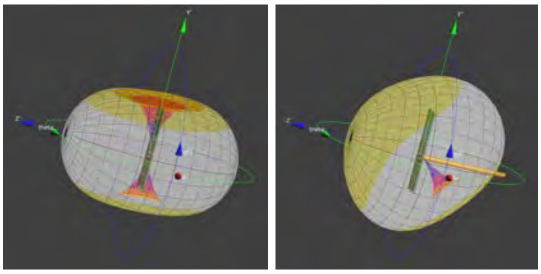

Figure 5. Numerical 3D radiation pattern of the 915 MHz antenna without (left), and with (right) a cable attached modelled in SIM4LIFE.

References

[1] Saario S, Thiel DV, Lu JW, O'Keefe SG. An Assessment of Cable Radiation Effects on Mobile Communications Antenna Measurements. IEEE Antennas and Propagation Society International Symposium, Jul 13–18, 1997 Montreal, CAN, pp. 550–553.

[2] TI. Sub-1 GHz and 2.4 GHz Antenna Reference Designs, CC-ANTENNA-DK-RD [Internet];

2017 [cited 2017 June 10]. Available from: http://www.ti.com/tool/CC-ANTENNA-DK-RD#Technical%20Documents.

Reflection Property Measurement of Skin in Terahertz Range Using Spectrometer with Photoconductive Antennas

Maya MIZUNO*, Kensuke SASAKI, and Soichi WATANABE
Applied Electromagnetic Research Institute, National Institute of Information and Communications Technology, Tokyo 184-8795, Japan

*Corresponding author: mmizuno@nict.go.jp

Abstract – The terahertz pulse electric field reflected from porcine skin was measured using a reflection time-domain spectrometer with photoconductive antennas. We observed two signals reflected from the skin surface and probably from the interface between the epidermis and dermis. To analyze the reflection properties, the average complex refractive indexes of the epidermis and dermis were measured using a transmission spectrometer in the band from 0.2 to 1 THz, and the reflectance was calculated from a flat double-layer model and the absorption coefficient in each layer. We indicated that the property differences between the skin and the flat double-layer model were caused by the refractive index difference between the upper and lower epidermis, and the measured values were reasonable in terms of geometrical optics. This finding suggests that the comparison between the reflection and transmission measurements was useful for verifying the optical property distribution of skin.

Keywords – terahertz pulse electric field; photoconductive antenna; epidermis; dermis

1. Introduction

Nondestructive inspection using terahertz waves with frequencies from 0.1 to 1 THz are emerging technologies [1–3]. For the inspections of biological tissues such as skin, a reflection terahertz time-domain spectrometer with photoconductive antennas is frequently used [4]. To evaluate the spectrometer, the biological phantoms having optical properties similar to those of tissues are useful. However, there is no appropriate phantom in the terahertz band. We therefore measured the reflectance of skin tissues (epidermis and dermis) with reflection terahertz time-domain spectrometers to design a phantom of skin. We considered an appropriate method for verifying the optical property distribution of skin as a first trial.

2. Measurement Specimens and Systems

We prepared a frozen porcine skin block, from which the epidermis surface was slightly shaved to remove hair. The block was thawed and then used for reflection measurement using a terahertz time-domain reflection spectrometer (T-Ray 4000, Luna Innovations Inc.). To measure the complex refractive index of the epidermis and dermis for input to the flat double-layer model, thin epidermis and dermis samples were prepared. Note that the optical property of the epidermis was almost the same with that of dermis at 0.2 THz when the free-water content was the same [5]. The complex refractive index spectra of the epidermis and dermis samples were measured using a transmission terahertz time-domain spectrometer (Rayfact SpecTera RS-01020, Tochigi Nikon) in the band from 0.2 to 1 THz.

3. Measurement Results

To verify the terahertz reflection properties of skin tissue consisting of the epidermis and dermis, as shown in Figure 1, we compared terahertz pulses reflected from the skin block and an aluminum plate (Figure 2). The time waveforms include the components of frequencies from approximately 0.2 to 1 THz. The peak frequency was around 0.2 THz. Porcine skin 1 was a single layer not including the epidermis, used for comparison with Porcine skin 2 having the double layer. As shown in the inset of Figure 2, the differential time waveform between the Porcine skins 1 and 2 had two negative peaks. This finding indicated that the waveform of Porcine skin 1 differed from that of Porcine skin 2; the time waveform of Porcine skin 2 included a signal reflected from the interface between the epidermis and dermis (R_2). The values of R_l and R_2, calculated from the square of the ratio of the electric field reflected from the sample to that from the metal, were 12.7 and 0.29%, respectively. From R_l (=0.127) and the interval between the negative peaks Δt, the epidermis thickness d_e was estimated to be 0.0134 cm from Equation (1). Here, the refractive index of the epidermis n_e was derived from R_l excluding the extinction coefficient of the epidermis κ_e. We therefore considered that d_e was underestimated.

$$d_e = c\Delta t / 2n_e \qquad (1)$$

To establish whether the above consideration is reasonable, we acquired the average complex refractive index spectra of the epidermis and dermis (Figure 3), and then calculated reflectance R_1, R_2 and absorption coefficient α at approximately 0.2 THz. R_2 was derived from Equation (2).

$$R_2 = (1-R_l)^2 \times \exp(-\alpha_e \times 2d_e) \times |(n_e - i\kappa_e - n_d + i\kappa_d)/(n_e - i\kappa_e + n_d - i\kappa_d)|^2 \qquad (2)$$

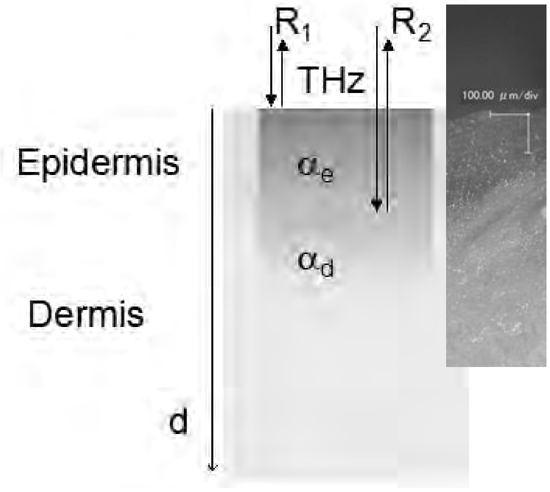

Figure 1. Schematic and microscope image of skin sample. R and α indicate the reflectance and absorption coefficient, respectively. Subscripts e and d respectively denote the epidermis and dermis.

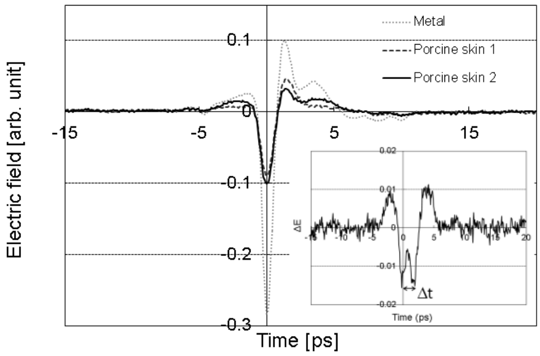

Figure 2. Time waveforms of terahertz electric field reflected from metal and two porcine skin blocks. The inset shows the differential electric field between the skin samples 1 and 2.

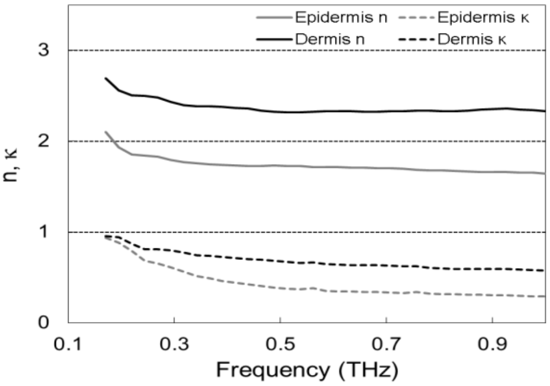

Figure 3. Refractive index and extinction coefficient of the epidermis and dermis

Table 1. Reflection and absorption properties of porcine skin block and double-layer model

	R_l (%)	α_e (cm^{-1})	R_2 (%)	α_d (cm^{-1})	d_e (cm)
Tissue	12.7	-	0.29	-	0.0134
Model	15.4	72.7	0.16	80.2	0.015

d_e was estimated to be 150 μm using microscope at 200 times magnification (Figure 1). As shown in Table 1, R_l for the skin block was smaller than that for the flat double-layer model. We considered that the skin block had a keratin layer, reducing the refractive index. The estimated d_e was smaller as mentioned above. R_2 for the flat double-layer model was smaller than that of the skin block owing to a large value of R_1 estimated from average complex refractive index. These results indicated that the differences in the reflection properties between the skin block and the flat double-layer model were caused by the refractive index difference between the upper and lower epidermis, and the measured values were reasonable in terms of geometrical optics.

4. Summary

Reflection properties from porcine skin were measured in the terahertz band using a reflection time-domain spectrometer. Comparing with the properties of a flat double-layer model based on a transmission measurement, we indicated that the refractive indices of the upper and lower epidermis differed, and the measured values were reasonable in terms of geometrical optics. This finding suggests that the comparison between the reflection and transmission measurements was useful for investigation of the optical property distribution of skin for phantom design in the terahertz band.

Acknowledgment

A part of this work was supported by the Ministry of Internal Affairs and Communications, Japan.

References

[1] Ajito K. Terahertz Spectroscopy for Pharmaceutical and Biomedical Applications. IEEE Transactions on Terahertz Science and Technology. 2015; 5: 1140–1145.

[2] Fukuchi T, Fuse N, Fujii T, Okada M, Fukunaga K, Mizuno M. Measurement of Topcoat Thickness of Thermal Barrier Coating for Gas Turbines Using Terahertz Waves. Electrical Engineering in Japan. 2013; 183 (4): 1–9.

[3] Fuse N, Naganuma A, Fukuchi T, Hori Y, Mizuno M, Fukunaga K. Underfilm Corrosion of Transmission Tower Cross-Arms Service-Used in a Pacific Coast Area. Corrosion. 2015; 71 (11): 1387–1397.

[4] Wilmink G. J, Ibey B. L, Tongue T, Schulkin B, Laman N, Peralta X. Roth G, C. C, Cerna C. Z, Rivest B. D, Grundt J. E, Roach W. P. Development of a Compact Terahertz Time-domain Spectrometer for the Measurement of the Optical Properties of Biological Tissues. Journal of Biomedical Optics. 2011; 16(4): 047006-1–10.

[5] Mizuno M, Yaekashiwa N, Watanabe S. Distinction of Dermal Conditions Related to Collagen State Using THz Spectroscopy. Millimeter and Terahertz Waves IRMMW-THz 2017; Aug. 29, 2017, Cancun, Mexico, TD.6, pp. 1–2.

Development of Optically-Based Sensors for Electric Field Measurement

－Review of Available Systems and Applications－

Benjamin G. Loader
Electromagnetic Technologies Group, National Physical Laboratory, TW11 0LW, UK
benjamin.loader@npl.co.uk

Abstract – Optical-based electric field sensors have been commercially available for more than a decade, yet their uptake in industry has been relatively slow, principally due to their higher cost and fragility compared to antennas or diode/thermocouple probes. However, the EMF environment is evolving rapidly and for some applications these sensors now offer specific advantages or unique capability. This paper provides an over-view of the current state-of-art of commercially available optical-based field sensor systems, their principle of operation and performance achieved. Further, specific application examples are developed for which the use of optical-based sensors justifies the additional costs of the systems.

Keywords – Electric field sensor, Pockels effect, VCSEL, EMF, autonomous vehicle

1. **Introduction**

Optical-based field sensors can be small, minimally perturbing and yield both magnitude and phase of the E- or H-field components being measured (i.e. full time-domain sensors). They are ideal for use in harsh EMF environments as the sensors can withstand high fields (i.e. 10kV/m) and the fibre optic cable is immune to EMF interference. Bandwidths in excess of 10 GHz can be achieved with 100 dB dynamic range and excellent linearity. Also, the signal attenuation for rf-on-fibre will be lower than for coaxial cable.

These sensor have been available commercially for more than a decade, and yet their uptake in industry has been relatively slow. Their high cost, fragility and difficulty in achieving high stability in real-world environments are factors in this. Detector bandwidths of a few Hz may be required for measuring weak fields, which is incompatible with measuring broadband signals and spectra. This paper examines three commercially available optical-based field sensor systems and examines specific application areas where their use is warranted.

2. **Commercially Available Systems**

The systems detailed represent state-of-the-art performance, and illustrate the different methods for achieving rf modulation of the optical carrier.

(a) Seikoh-Giken (Japan)

The Seikoh-Giken sensors [1, 2, 3] utilize the Pockels effect, whereby the refractive index of an electro-optic material changes linearly with applied electric field. The sensor consists of a Michaelson interferometer (reflections type) infused onto an electro-optic substrate, as shown in Fig. 1. An electrode structure applies the incident field differentially across the two optical tracks of the interferometer resulting in amplitude modulation of the optical signal. The modulated signal is reflected from the end of the modulator chip by an angled mirror so that it passes back down the input fibre and is diverted to the photodiode by a circulator. The rf output is then amplified and measured with a suitable receiver.

The main specifications for the Seikoh-Giken sensors are given in Table 1. A 6 mm diameter single axis sensor (model NLD) is also available.

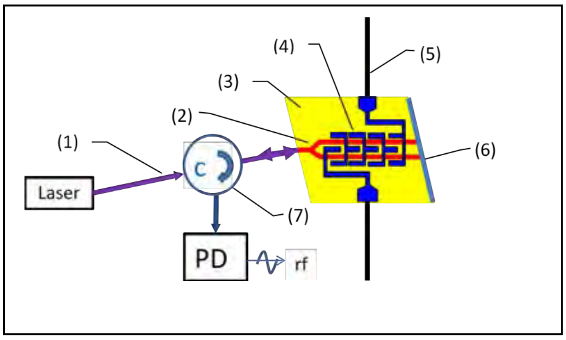

Figure 1. Schematic of single axis optical electric field sensor. In the diagram (1) is the input fibre (2) is optical waveguide, (3) is the lithium niobate substrate, (4) is the electrode structure, (5) antenna elements, (6) is a mirror and (7) is a circulator. PD is the photo-detector.

Table 1. Seikoh-Giken OEFS- sensor types and their specifications

Parameter	**Sensor model**		
	SH-03EX	SH-10EX	SH-10EL
Type	3-axis, high sensitivity	3-axis, broadband	3-axis, compact
Frequency	100 kHz to 3 GHz	100 kHz to 10 GHz	100 kHz to 10 GHz
Sensor size	30 mm Ø × 90 mm	40 mm Ø × 90 mm	12 mm Ø × 80 mm
E-field range(1)	2 mV/m to 100 V/m	10 mV to 500 V/m	0.5 V/m to 25 kV/m
Isotropy (typical)	± 1 dB	± 1 dB	± 0.5 dB

(1) With 10 Hz detector bandwidth

(b) Kapteos Field Sensor

The Kapteos system uses an optical cavity with mirrored surface opposite to the input fibre. Modulation of the optical carrier is achieved using changes in polarization state in the cavity. This method achieves a high sensitivity with a relatively short interaction length, yielding bandwidths of up to 40 GHz. The optimal choice of modulator material and polarization state are described in [4, 5]. The sensor is housed in a hermetic case, allowing it to be used in liquids and plasmas.

The DC output of the optoelectronic detector correlates to the sensor temperature and is used to correct for changes in sensitivity due to temperature. The rf output provides the amplitude and phase of one component of the incident electric field. Table 2 lists the main system specifications. Three separate sensors can be connected to the controller unit so that isotropic field levels can be determined. Note that the E-field sensor is unaffected by magnetic fields up to 4.7 T.

Table 2. KAPTEOS sensor specifications

Parameter	Specification
Sensor type	Single axis, linear polarised
Dimensions	Ø = 5 mm, L = 35 mm
Field range	0.05 V/m to 2 MV/m
Damage level	E-field: >10 MV/m
Operating temperature	0 to 50°C and changes of up to 30°C/minute
Bandwidth of sensor	10 GHz or 40 GHz versions
Controller (3-channel)	LF controller: 40 Hz to 30 MHz MF controller: 1 kHz to 1 GHz HF controller: 3 kHz to 40 GHz

(c) SPEAG TDS System

The SPEAG TDS system is based on direct modulation of a high speed solid state laser VCSEL (vertical cavity surface emitting LASER) [6]. The signal from the field sensor is amplified and used to modulate the VCSEL laser. The modulated optical signal passes along the fibre-optic cable and is demodulated using a photodiode. This approach achieves outstanding sensitivity for the small size of sensor and the sensing elements is very close to the tip of the probe.

Fig. 2 shows a magnetic field sensor comprising loop antenna, low noise amplifier, VCSEL laser and photovoltaic cell (PV) used to power the electronics in the sensor head. These are contained within a probe tip having dimensions 4 mm by 4mm^2. The system has single-axis E-field and H-field probes and their key specifications are given in Table 3. Probes are designed to be use as handheld nearfield probes for locating EMC emissions in PCB, and also with an automated scanning system [7].

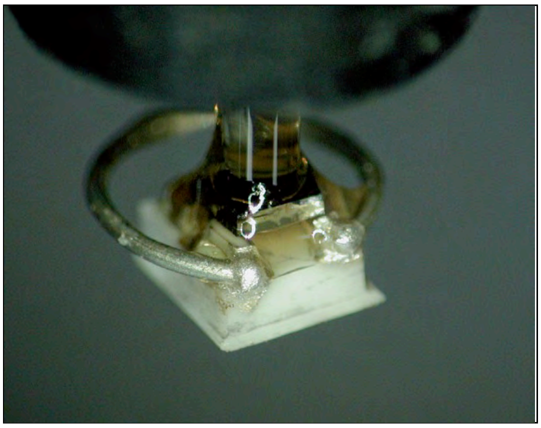

Figure 2. Showing the H-field sensor. This incorporates the loop, amplifier, VCSEL and photo-voltaic (PE) cell. This structure fits within a cube having linear dimensions 4 mm.

Table 3. SPEAG TDS system specifications

	E1TDS	H1TDS
Type	Single axis E-field (1)	Single axis H-field(1)
Measurement range (2)	0.3 mV/m to 300 V/m	0.3 µA/m – 1 A/m at 2 GHz
Frequency range	10 MHz to 10 GHz	10 MHz to 10 GHz
Tip dimensions	4 mm by 4 mm^2	4 mm by 4 mm^2
Sensor element	2.8 mm dipole	2 mm by 2mm loop

(1) Sensitivity may be radial or parallel to the probe axis dependent on version.

(2) Low level sensitivity corresponds to a detector r.b.w. of 1 Hz.

3. Application Examples

Optical-based field sensors have been applied to a number of research areas including plasmas, railway transformer harmonics, automotive EMC, shielding effectiveness tests, MRI scanners, and monitoring base stations on HV pylons. They have also been used for field measurements in close proximity to circuit boards (EMC emission) and absorbers (radar stealth applications). In this section, three application examples for the optical-based field sensors are presented.

(a) Magnetic Resonance Imaging (MRI)

Optical-based field sensors are ideally suited for use in the MRI environment, and can measure the rf signals in the presence of high static and switched gradient magnetic fields. Optical sensors have been applied for B-field shimming within the bore and artefact location. They can also be used for local specific absorption rate (SAR) assessment in implant heating.

For patient safety it is necessary to test an implants MR compatibility, and in particular the tissue heating that occurs when it is exposed to the rf fields from the scanner. This involves submerging the implant in a gel phantom, and measuring the temperature rises recorded during a 15-minute exposure [8]. The local SAR at the measurement positions is then assessed, normally by thermal methods. Time constraints when using MRI scanners mean that the phantom is normally cooling down from the implant test when the local SAR is assessed, and this results in an error of around -1.2W/kg (-30%). Using the optical-based E-field probe eliminates this error and reduces the measurement time. Note that the electric field in the phantom is predominately along the axis of the scanner bore, so that a single axis probe is sufficient.

(b) Mobile Phone Handset EMF Safety Assessment

The method for assessing SAR from handsets involves measuring E-fields over a 2D surface and 3D cube within a phantom to give the spatial peak 1g or 10g mass-averaged SAR from the device [9]. The probe positioning is accomplished using a robot. The testing time for a modern SMART phone, which may have thirty or more transmission bands/protocols embedded within it, is excessive. As a result, systems that “image” the electric field distributions using arrays of electric field sensors (magnitude and phase) embedded in a phantom have been developed. However, it is difficult and costly to establish calibration and validation of the sensor arrays and to quantify the uncertainties.

Using a two-axis optical-based field sensor on the scanning system reduces the test times compared to scanning measurements with a diode-based probe. This is because field reconstruction algorithms allow the fields in volumes to be determined from the complex fields measured on a 2D plane. However, it is much simpler to establish traceable calibration of the single probe system than for the array. The use of a full time domain sensor also means multiple frequency bands can be tested in a single scan, and MIMO devices can be assessed more accurately. Further, the vector probe can be retro-fitted to existing SAR measurement systems with robots, reducing the costs of implementation.

(c) High Data-Rate Up Link in Wireless Communications

Most consumer applications in mobile communications require high data download rates, for example video streaming or mobile internet applications. However, there are some that require high data bandwidth for the uplink, which can be achieved using rf-over-fibre. This is particularly attractive if the existing fibre-optic networks can be utilized. The large bandwidth (10 GHz or more) of the optical-based field sensors offer the potential as the transducer for this application. Specific examples are: Spectrum monitoring for license enforcement and dynamic spectrum allocation, mobile TV broadcast unit data links for live coverage of sporting events, and real time monitoring of sensor and image data from a number of driverless vehicles at road junctions to analyse their performance. RF-on-fibre systems are also of great interest for use in satellites because they have potential to reduce the weight and power budget. VCSEL devices are particularly suited to this application.

4. Conclusions

Very high performance optical-based field sensors are available commercially, and these employ a number of different approaches to modulating the optical carrier with the rf signals. They are small, minimally perturbing and provide full time domain measurement capability (magnitude and phase). However, they are expensive due to the complexity of their fabrication and low volume of production (their main use has been in research applications). The EMF spectrum, usage and applications are evolving rapidly, and this affords great opportunities for the use of these sensors in a number of important application areas.

References

[1] Kuwabara N, Tajima K, Kobayashi R, Amemiya, F. Development and Analysis of Electric Field Sensor Using LiNbO3 Optical Modulator. IEEE Trans. Electromagn. Compat. 1992; 34(4), 391–396.

[2] Torihata S, Loader B. The New Principle E-Field Sensor for Automotive Immunity Testing. Automotive EMC Conference 2003, Nov. 6, 2003, Milton Keynes, UK.

[3] Loader B, Gregory A, Bownds D, Siefert F. Evaluation of an Optical Electric Field Sensor for Measurement of Specific Absorption Rate (SAR) during Magnetic Resonance Imaging. 2012 International Symposium on Electromagnetic Compatibility (EMC EUROPE) Sept. 17–21, 2012, Rome, Italy.

[4] Duvillaret L, Rialland S, Coutaz J-L. Electro-Optic Sensors for Electric Field Measurements I: Theoretical Comparison among Different Modulation Techniques. J. Opt. Soc. Am. B. 2002; 19(11), 2692–2703.

[5] Duvillaret L, Rialland S, Coutaz J-L. Electro-Optic Sensors for Electric Field Measurements II: Choice of the Crystals and Complete Optimization of Their Orientation. J. Opt. Soc. Am. B. 2002; 19(11), 2704–2715.

[6] Kramer A, Müller P, Lott U, Kuster N, Bomholt F. Electro-Optic Fiber Sensor for Amplitude and Phase Detection of Radio Frequency Electromagnetic Fields. Opt. Lett. 2006; 31(16), 2402–2404.

[7] Kuehn S, Wild M, Gomez M, Grobbelaar E, Sepan P, Kochali B, et al. EMC/EMI Near-Field Testbed for EM Phasor Measurements Using Active Optical Sensors. 2015 Asia-Pacific International Symposium on Electromagnetic Compatibility (APEMC) May 25–29, 2015, Taipei, Taiwan, pp. 402–405.

[8] ASTM F2182 – 11, Standard Test Method for Measurement of Radio Frequency Induced Heating on or near Passive Implants during Magnetic Resonance Imaging. ASTM International, West Conshohocken, PA, 2011, www.astm.org.

[9] IEC 62209-1:2016, Measurement Procedure for the Assessment of Specific Absorption Rate of Human Exposure to Radio Frequency Fields from Hand-Held and Body-Mounted Wireless Communication Devices - Part 1: Devices Used Next to the Ear (Frequency Range of 300 MHz to 6 GHz), Ed 2, 2016.

Photonics-Based Millimeter and Terahertz Wave Visualization Techniques for Industrial Applications

Shintaro HISATAKE[1*]
[1]Department of Electrical, Electronic and Computer Engineering, Gifu University, 501-1193 Gifu, Japan
[*]Corresponding author: hisatake@gifu-u.ac.jp

Abstract – We present two photonics-based millimeter and THz wave visualization systems for industrial applications. Synchronized coherent measurement system reveals not only the antenna radiation pattern but also several unique phenomena such as wavefront conversion by a metal hole array and a sub-wavelength compressed beam generation by a dielectric cuboid. Asynchronous measurement system visualizes the near-field of the electric field radiated from the antennas integrated with self-oscillating generators such as CMOS oscillators, Gunn oscillators, resonant tunneling diodes, and quantum cascaded lasers. Asynchronous measurement system enables us to diagnose and characterize the on-chip antenna devices without antenna detachment.

Keywords – electrooptic measurement; non-polarimetric technique; self-heterodyne technique: antenna characterization

1. Introduction

Recently, millimeter (mm) and terahertz (THz) waves have attracted significant attention owing to their applications in radar systems [1], 5G networks [2], THz wireless communication [3], etc. In these higher frequency regions, the electromagnetic (EM) waves are inevitably used as beams and beam quality becomes more important compared with the microwaves. Short wavelength makes antenna small, and on-chip antenna devices, in which the antennas are integrated with peripheral circuits have been extensively studied [4]. Near-field mapping or visualization has proven to be a powerful technique to diagnose the antennas and characterize the beam quality in the microwave frequency range. Visualization systems for EM beams in mm and THz frequency band will become an important key to their industrial utilization.

In this paper, we introduce the two photonics-applied visualization systems for mm and THz waves; synchronized coherent measurement system and asynchronous measurement system (Fig. 1). We measure the amplitude and phase of the EM waves by the electrooptic (EO) probes. The key techniques are (1) non-polarimetric EO down conversion technique [5, 6], (2) self-heterodyne technique [7], and (3) phase noise cancellation technique [8]. Non-polarimetric EO down conversion technique has solved an intrinsic problem of the conventional polarimetric EO detection technique, in which the sensitivity of the measurements can be changed drastically by the fluctuation of the polarization state of the optical local oscillator signal (LO signal) for the EO detection. Self-heterodyne technique enable us to measure the amplitude and

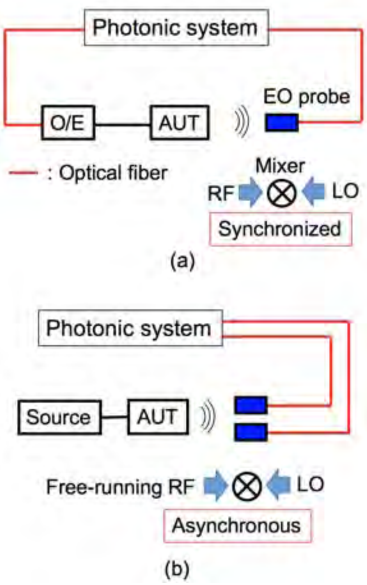

Figure 1. Two measurement systems. (a) synchronized coherent measurement system and (b)asynchronous measurement system.

phase of the mm-wave and THz wave precisely with wide frequency tunability using free-running laser diodes (LDs). The phase noise cancellation technique cancels out the relative frequency/phase fluctuation between the EM wave (RF signal) and LO signal in the measurement system to measure the relative phase of EM waves generated by the free-running self-oscillating sources.

2. Synchronized Coherent Measurement System

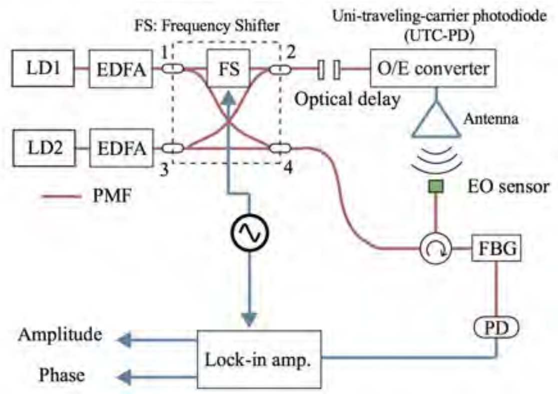

Figure 2. Synchronized coherent measurement system. The RF and LO signals are generated based on the self-heterodyne technique. The EO detection is based on the non-polarimetric EO down conversion technique.

Figure 2 shows the schematic of the synchronized coherent measurement system. The RF and LO signals are generated based on the self-heterodyne technique. The EO detection is based on the non-polarimetric EO down conversion technique. Two free-running 1.55 μm LDs are used for the RF signal generation and also used for the probe beam as an LO signal. The frequencies of the LDs were f_1 and f_2, and combined using polarization-maintaining fiber (PMF) couplers to produce a beat note at a frequency of $f_2 - f_1 - f_s$ for THz wave generation (RF). Here, an EO frequency shifter was used to shift the frequency of the LD1 (f_1) by f_s.

A uni-travelling-carrier photodiode (UTC-PD) was used as an optical-to-electrical (O/E) converter. As shown in Fig. 3, the EM field to be measured is up-converted to the optical frequency region through the phase modulation of the probe beam. Then, the generated sideband is down-converted to the IF frequency band by the optical coherent detection. The amplitude and phase information of the EM field to be detected is copied to those of the IF signal and detected by a lock-in amplifier.

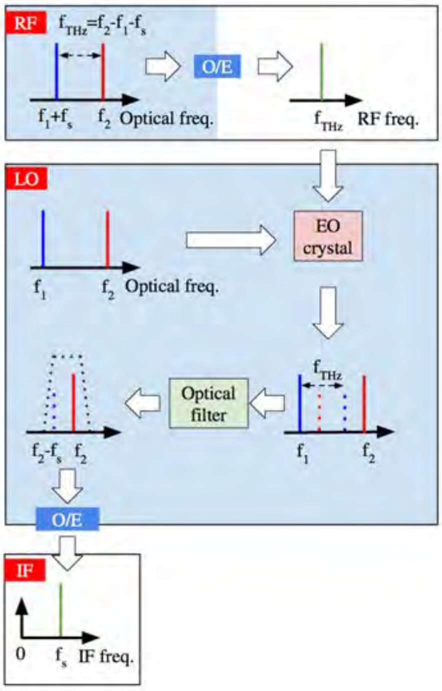

Figure 3. Principle of the non-polarimetric EO down conversion.

The synchronized coherent measurement system is suitable for the measurements of such as (1) EM response of the devices, (2) propagation, diffraction, and scattering of EM beams, and (3) antennas which can be detached from the generators. Figures 4(a) and (b) show the examples of the visualized THz waves (125 GHz) re-emitted from a metal hole array (MHA) and Teflon cuboid, respectively. The MHA is excited by the THz wave with a quasi-spherical wavefront at the resonant frequency. As shown in Fig. 4(a), the excited EM field oscillates in-phase at the surface of the MHA, as a result, the plane wave is re-emitted from the MHA. This result suggests that MHA can be used as a wavefront manipulator [8]. On the other hand, the cuboid with a refractive index of n=1.46 at 125 GHz generates terajet as shown in Fig. 4(b).

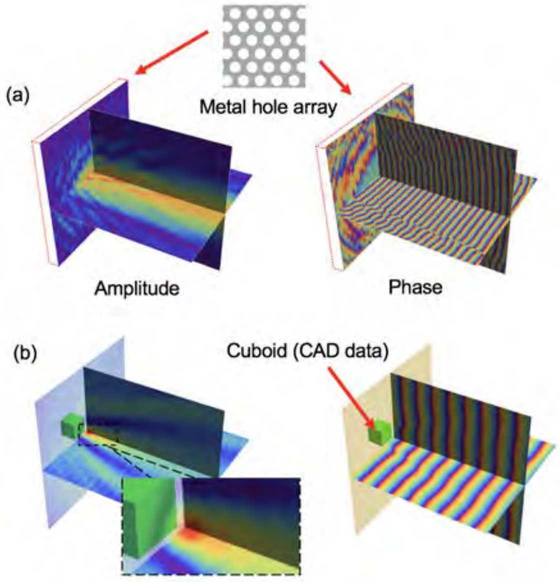

Figure 4. Experimentally visualized THz waves (125 GHz). (a)Metal hole array converts the quasi-spherical wavefront to the plane wavefront. (b)Cuboid focuses the EM wave in sub-wavelength region.

The subwavelength compressed beam and the Gouy phase shift phenomena of the terajet are directly observed. We found that the intensity enhancement of about 7.4 dB and full width at half maximum of 0.6λ are obtained at the distance 0.5λ from the cuboid [9]. We have applied this phenomenon to the THz imaging application [10].

3. Asynchronous Measurement System

Asynchronous measurement system enables us to visualize the spatial distribution of the EM field emitted from self-oscillating devices. Figure 5 shows the schematic of the system. The RF signal is down converted by the non-polarimetric EO down conversion technique. In the phase noise cancellation stage, the frequency of IF signal1 is up-converted by f_s, using an electrical mixer and then down-converted to f_s, by mixing with IF signal2. With this double-stage mixing process, the common mode phase noise is cancelled-out and only the phase difference between IF signal1 and signal2 are measured by lock-in detection with a local reference signal, f_s.

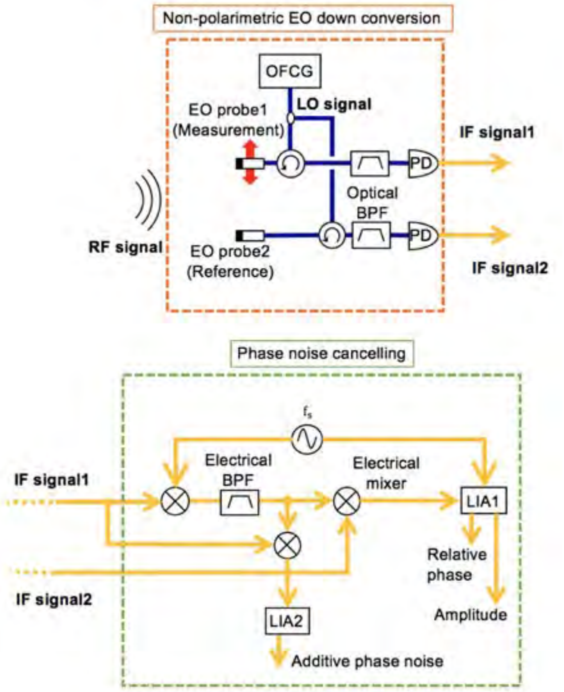

Figure 5. Schematic of the asynchronous measurement system.

Figure 6 shows visualized relative phase distribution of the mm-wave (77 GHz) generated by the self-oscillating Gunn diode. The long-term frequency fluctuation and short-term frequency drift were 1 MHz and ± 300 kHz, respectively. In this experiment, the mm-wave was divided by a rectangular-waveguide-type power divider. Port1 of the divider was connected to the pyramidal horn antenna, whereas, port2 was kept open for the phase reference measurement. Note that the pyramidal horn antennas in Fig. 6 are simulation models.

We also confirmed that our asynchronous measurement system can measure the relative phase distribution with the theoretically limited sensitivity restricted by a signal-to-noise ratio of the amplitude measurement. Without detaching the antennas from the chip, our system visualizes the near field. The far-field radiation pattern can be calculated from the measured near-field data.

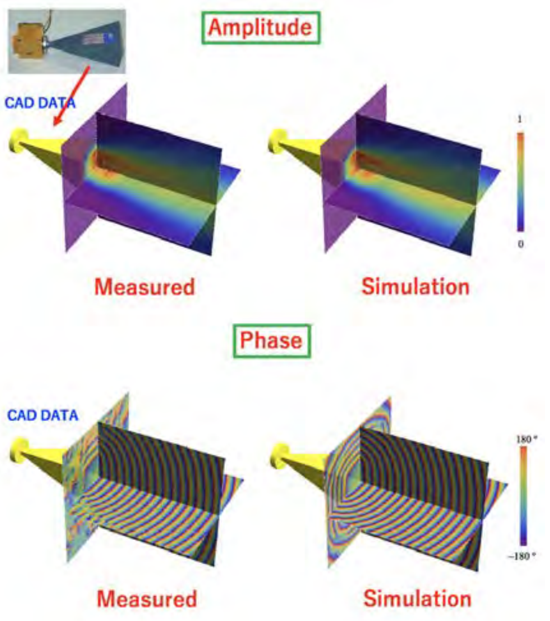

Figure 6. Amplitude and phase distribution of the mm-wave (77 GHz) generated by a free-running Gunn diode. The mm-wave was emitted by a pyramidal horn antenna. (a) Measured results and (b) simulated results.

4. Conclusion

We demonstrated two systems for the EM wave visualization. The photonics technology is the key in both systems. The synchronized coherent measurement system is suitable for the measurements of the devices which can be detached from the source. Asynchronous measurement system enables us to visualize the spatial distribution of the EM field emitted from self-oscillating devices without detaching the antennas. We believe that both measurement systems pave the way for mm wave and THz wave industrial applications, where the beam quality becomes more important compared with the microwaves.

Acknowledgements

The author thanks to H. H. Nguyen Pham, H. Nakajima, K. Yamaguchi, and Prof. T. Nagatsuma of Osaka University, K. Miyaji, M. Tojyo, and Y. Oikawa of Think Lands Co. Ltd., Dr. H. Uchida of Arclry Inc., and Profs. I. V. Minin and O. V. Minin of National Research Tomsk State University for their encouragement, help, and support. This work was supported in part by JSPS KAKENHI Grant Number 15K13383 and SENTAN, JST.

References

[1] J. Grzyb, K. Statnikov, N. Sarmah, B. Heinemann, and U. R. Pfeiffer, "A 210-270-GHz circularly polarized FMCW radar with a single-lens-coupled SiGe HBT chip," IEEE Transactions on Terahertz Science and Technology, vol. 6, pp. 771-783, 2016.

[2] T. S. Rappaport, S. Sun, R. Mayzus, H. Zhao, Y. Azar, K. Wang, G. N. Wong, J. K. Schulz, M. Samim, and F. Gutierrez, "Millimeter wave mobile communications for 5G cellular: It will work!," IEEE access, vol. 1, pp. 335-349, 2013.

[3] T. Nagatsuma, G. Ducournau, and C. C. Renaud, "Advances in terahertz communications accelerated by photonics," Nature Photonics, vol. 10, pp. 371-379, 2016.

[4] H. M. Cheema and A. Shamim, "The last barrier: on-chip antenna," IEEE Microwave Magazine, vol. 14, pp. 79-90, 2013.

[5] S. Hisatake and T. Nagatsuma, "Nonpolarimetric technique for homodyne-type electrooptic field detection," Appl. Phys. Express, vol. 5, 012701, 2012.

[6] S. Hisatake, H. H. Nguyen Pham, and T. Nagatsuma, "Visualization of the spatial-temporal evolution of continuous electromagnetic waves in the terahertz range based on photonics technology," Optica, vol. 1, pp. 365-371, 2014.

[7] S. Hisatake, G. Kitahara, K. Ajito, Y. Fukada, N. Yoshimoto, T. Nagatsuma, "Phase-Sensitive Terahertz Self-Heterodyne System Based on Photodiode and Low-Temperature-Grown GaAs Photoconductor at 1.55μm." IEEE Sensors Journal, vol. 13, pp. 31-36, 2013.

[8] S. Hisatake, H. Nakajima, H. Uchida, K. Miyaji, and T. Nagatsuma, "Amplitude and phase mapping of millimeter-waves generated by a free-running Gunn diode oscillator," 41st International Conference on Infrared, Millimeter, and Terahertz waves (IRMMW-THz 2016), T5P.09.13 , 2016.

[9] H. H. Nguyen Pham, S. Hisatake, I. V. Minin, O. V. Minin, and T. Nagatsuma, "Three dimensional direct observation of Gouy phase shift in a terajet produced by a dielectric cuboid," Appl. Phys. Lett., vol. 108, 191102, 2016.

[10] H. H. Nguyen Pham, S. Hisatake, O. V. Minin, T. Nagatsuma, I. V. Minin, "Enhancement of spatial resolution of terahertz imaging systems based on terajet generation by dielectric cube," APL Photonics, vol. 2, 056106, 2017.

94-GHz IQ Radar System Using an Optical FM-CW Signal Generator

Atsushi KANNO*, Norihiko SEKINE, Akifumi KASAMATSU, Kaori FUKUNAGA,
Naokatsu YAMAMOTO, and Tetsuya KAWANISHI†
National Institute of Information and Communications Technology, 184–8795 Tokyo, Japan.
†Waseda University, 169–0072 Tokyo, Japan.
*Corresponding author: kanno@nict.go.jp

Abstract – A frequency-modulated continuous-wave (FM-CW) radar system at 94 GHz with a bandwidth of 2 GHz is configured by an optical millimeter-wave synthesizer for the short-range ranging application. Obtained bin resolution for detection is approximately 10 cm, which is caused by a sampling rate of the detector. The millimeter-wave front-end with an IQ detector and an antenna separation feature is configured with A4-size foot-print designed for the hand-held application.

Keywords – millimeter-wave, FM-CW radar, optical millimeter-wave synthesizer, antenna pattern measurement.

1. Introduction

Nondestructive imaging (NDI) technologies are highly demanded to enhance public safety and security; for instance, security checkpoints at airports and logistic centers require to detect burnable, explosive, dangerous, and prohibited items without any damages. X-ray NDI systems are already developed and installed in worldwide with a high image resolution; however, high energy of the X-ray photons may cause severe damages to the inspected items, including human bodies. Therefore, low-energy photons, such as microwave and millimeter-wave radios, has become an alternative solution for NDI emitters [1, 2]. For precise imaging, including ranging, a high-precision signal source for radio waves is required, but it has large SWaP generally, and therefore, the hand-held system is hard to be configured. Especially in millimeter-wave signals, the extremely high transmission loss of the transmission media such as coaxial cables and rigid waveguides avoids making any connections between the signal source and a radio front-end.

In the study, millimeter-wave signal synthesizer based on an optical modulation technique is configured and applied for remote access from the source to the radio front-end via an optical fiber cable. In addition, in the front-end, an IQ downconverter is used for detection with high common-mode rejection ratio under a frequency-modulated continuous-wave (FM-CW) radar configuration.

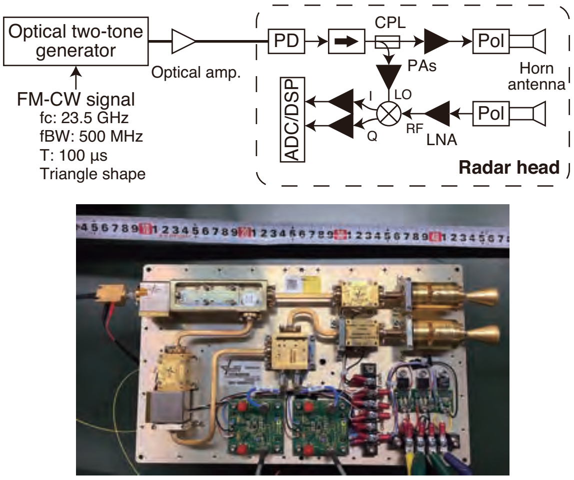

Figure 1. (top) Schematic diagram of an experimental setup and (bottom) photo of an radar head.

2. System Configuration

Figure 1 shows a schematic configuration of the system. An optical two-tone generator based on an optical modulator is driven by an input FM-CW signal at a center frequency of 23.5 GHz with an FM-CW sweep bandwidth of 500 MHz and a triangle-type FM-CW duration of 100

μs [3]. An optical amplifier optimizes a power of the optical FM-CW signals launched into a high-speed photodiode (PD) at a radar head. Since an optical carrier-suppressed second-order harmonic generation is configured by the two-tone generator, the PD regenerates the radio signal at 94 GHz with 2-GHz bandwidths by an optical frequency quadrupling technique. In the radar head, 94-GHz signals are passed through an isolator to split into two components by a directional coupler (CPL); one is for a transmitter and the other for a local oscillator (LO) component in a receiver. A power amplifier (PA) boosts up the signal to 10 mW, and then, a conical horn antenna with a polarization switch (Pol) irradiate the signal into the air. A reflected signal from targets is collected by the other antenna with the Pol. A low noise amplifier (LNA) optimizes the input level of the signal into an IQ mixer, which is operated by the LO component amplified by the PA. Down-converted I and Q signals, which power levels are optimized by instrumentation amplifiers are captured by an analog-to-digital converter (ADC). In the proof-of-concept demonstration, digital signal processing (DSP) including fast Fourier transform (FFT) and peak detection by a constant threshold value for ranging is performed by offline processing using a personal computer.

3. Results

For proof-of-concept demonstration, we evaluate an FM-CW radar performance under short-distance ranging configuration. A metal plate is used as a target under test. Figure 2 shows obtained peak structures in various target distances from the facet of the antennas. Obtained IF peaks follow linear relationships between the target distances and expected target distances estimated by the IF frequency. Differences between estimated and actual distances from the target are caused by the mismatch of the IF and RF electrical path lengths in the radar front end; calibration can compensate the mismatches. Quantization of the obtained peaks is caused by the FFT size of 1024 with 25-Ms/s ADC, which provides a bin size of approximately 24 kHz. The resolution by the FFT is obtained about 10 cm, which is comparable to an FM-CW resolution of 7.5 cm described by $c/2f_{BW}$. Super-resolution technique might be applicable for improvement of the resolution.

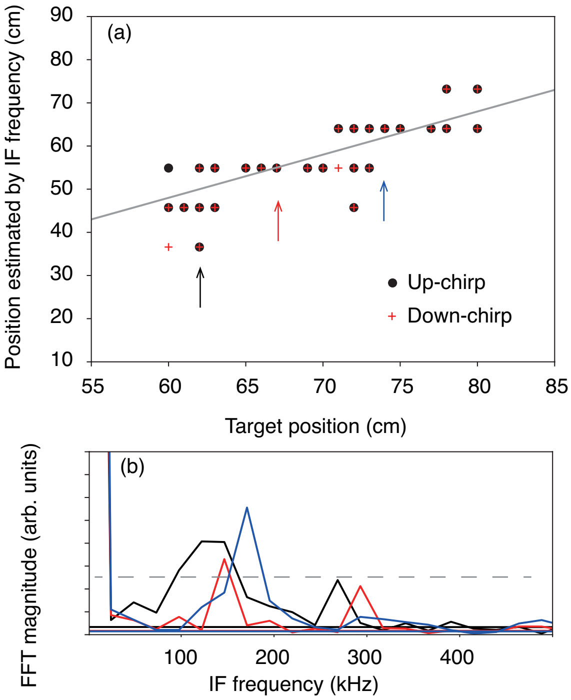

Figure 2. (a) Estimated target positions with various distances from the antenna facet under up-chirp (black circle) and down-chirp (red cross) waveforms and (b) corresponding IF frequency spectra at the distance indicated in (a) with colored arrows. Gray dashed line shows a threshold of the peak detection in the DSP.

Spatial resolution is also a key for obtained images. Figure 3 shows obtained beam profiles of irradiated beams with different distances from the facet of the antenna. A terahertz camera with 64 × 64 pixels is used as a beam profiler of the millimeter-wave signal with a pixel pitch of 1.5 mm [4]. At proximal position, obtained beamwidths seem to be constant because of a near-field region. At far from 10 cm, beamwidths increase with an increase of the distance between the camera and the antenna facet. Estimated slope of 0.24 corresponds to the beamwidth of approximately 14 degrees. It is consistent with the beamwidth of a conical horn antenna with an antenna gain

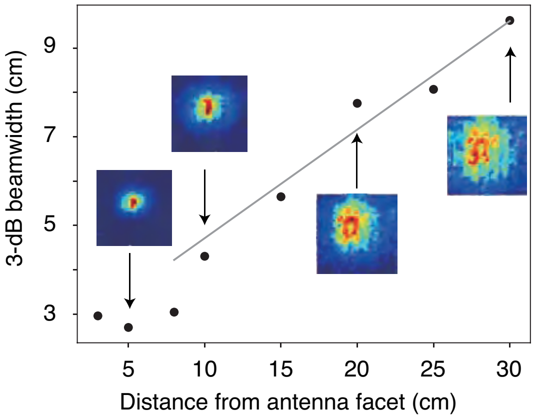

Figure 3. 3-dB beamwidths of the irradiated millimeter-wave signal at different observed positions. Beam profiles are also shown in the figure.

of 21 dBi. The 3-dB beam diameter is estimated of 21 cm when the target distance from the antenna is 80 cm; for precise imaging, antenna gain should be increased to 30 dBi or more.

4. Conclusion

An optical fiber-connected 94-GHz FM-CW radar with IQ detection is demonstrated with 2 GHz bandwidth. The obtained resolution is limited by the sampling rate of the receiver, not by the FM-CW bandwidth. Low SWaP operation at the radar heads is applicable for hand-held ranging applications such as an NDI for construction health monitoring and inspections of ancient arts [5, 6].

Acknowledgement

This work is partially conducted as a part of the project entitled “Research and development for expansion of radio wave resources," funded by the Ministry of Internal Affairs and Communications, Japan, and JSPS Grants-in-Aid for Scientific Research Grant Number JP16K06406.

References

[1] McMakin, D., and Sheen, D., “Millimeter-wave advanced imaging technology," 2011 Joint American Assoc. Physicists in Medicine and Canadian Org. Med. Physicists (AAMP/COMP), Vancouver, Canada, WE-G-301-4 (August 2011).

[2] Ahmed, S. S., “The state of the art in personnel screening with mm-wave technology for security checkpoint," Defense, Security and Space Forum in Euro. Micorw. Week 2014, Rome, Italy (September 2014).

[3] Kanno, A., and Kawanishi, T., “Broadband frequency-modulated continuous-wave signal generation by optical modulation technique," J. Lightw. Technol. 32(20), 3566–3572 (2014).

[4] Kanno, A., Sekine, N., Kasamatsu, A. and Yamamoto, N., “W-band transmission imaging by photonics-based millimeter-wave synthesizer and high-power traveling-wave-tube amplifier," Intl. PEM Workshp, Kyoto, Japan, paper SB-2 (November 2015).

[5] Fukunaga, and K., Picollo, M., “Characterisation of works of art," *Terahertz Spectroscopy and Imaging*, 521–538, Springer, 2012.

[6] Guillet, J. P., Roux, M. Wang, K., Ma, X., Fauquet, F., Darracq, F., and Mounaix, P., “Art Painting Testing with Terahertz Pulse and Frequency Modulated Continuous Wave," Proc. PIERS, St. Petersburg, Russia, 725, May 2017.

Development of GHz-Band Optical E-Field Sensor Calibration System in NMIJ

Michitaka AMEYA[1*] and Satoru KUROKAWA[1]
[1]Research Institute for Physical Measurement,
National Institute of Advanced Industrial Science and Technology, Tsukuba, 805-8563, Japan
*m.ameya@aist.go.jp

Abstract –To assure the reliability of the electric-field sensors for 5G mobile communication and assessing the human exposure limit, GHz-band electric-field calibration system is required in Japan. Our institute is now developing the electric-field calibration system for optical electric-field sensor and conventional electric-field sensor in the frequency range above 2 GHz. In this paper, we report the progress of performance evaluation of electric-field generating equipment and electric-field sensor itself. From the evaluation results, the optical electric-field sensor with spectrum analyzer has bigger thermal dependency compared to the conventional electric-field sensor. On the other hand, it is observed that the linearity of the optical electric-field sensor is better than that of the conventional electric-field sensor. The field uniformity in *z*-axis and *xy*-plane is also discussed in the paper.

Keywords – electric-field sensor calibration, time-stability, field uniformity, uncertainty evaluation.

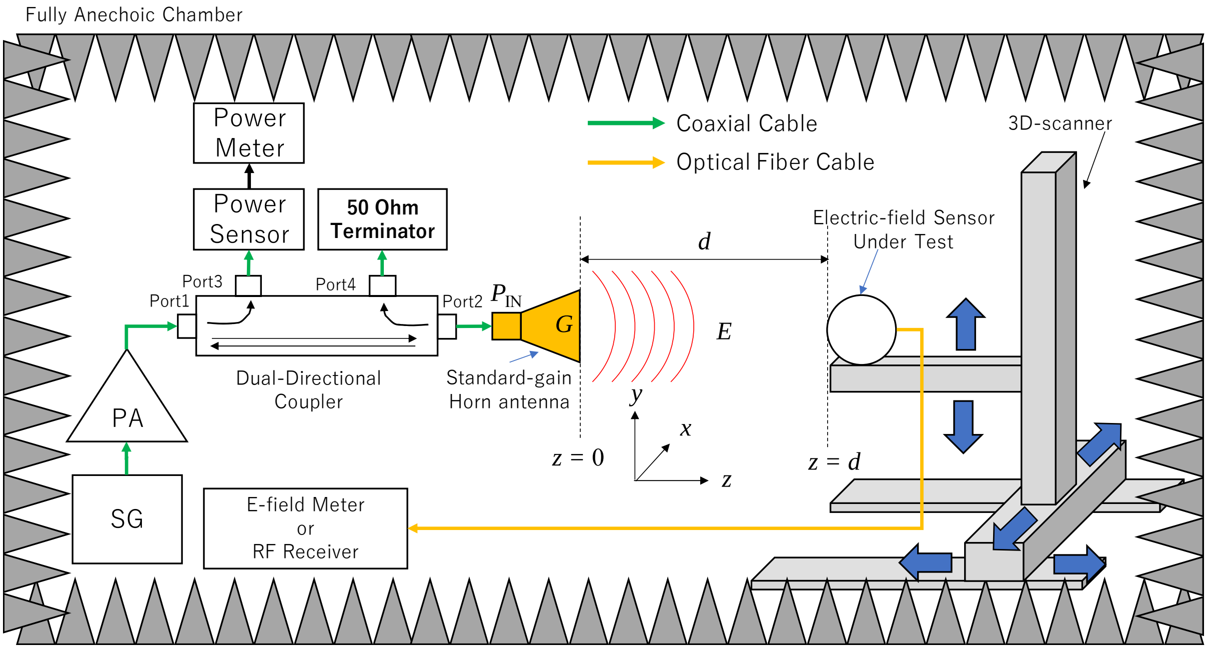

Figure 1. Setup of electric-field sensor calibration system in NMIJ.

1. Introduction

The reliable GHz-band electric-field sensor is required for developing the 5G mobile network and assessing the human exposure limit of electric-field in GHz [1]. To assure the reliability of the electric-field sensor, the sensor should be calibrated by the manufacturer of the sensor or an accredited calibration laboratory. Our NMIJ is only the national metrology institute in Japan. We establish a lot of metrology standard for the domestic user and other neighbor countries. The electric-field calibration service up to 2 GHz is already available from 2015. Now we are developing the calibration system above 2 GHz for the GHz-band electric-field sensor. In this paper, we report the progress of developing the GHz-band (especially in the frequency range from 4 to 6 GHz) electric-field sensor calibration system in our institute.

2. Electric-Field Sensor Calibration System Using Standard Gain Horn Antenna

According to the IEEE Std 1309-2013[2], the use of standard gain horn antenna is recommended for calibrating the electric-field sensor operated in GHz-band. The setup of our calibration system is shown in Figure 1. Basically, the electric-field generated from the antenna can be calculated by the equation.

$$E_{\mathrm{RMS}} = \frac{\sqrt{30PG}}{d} \qquad (1)$$

where E_{RMS} is generated electric field strength in rms value, d is the distance between antenna and the electric-field sensor, P is the input power to the antenna and G is the antenna gain of standard gain horn antenna.

To develop a calibration system for electric-field sensor, we should evaluate the performance of electric-field generating system and the electric-field sensor itself. In addition, the measurement uncertainty should be estimated for issuing the calibration certificate. There are a lot uncertainty factors for electric-field sensor calibration system. The list of uncertainty factors is shown in Table 1.

Table 1. Uncertainty factors for electric-field sensor calibration

Uncertainty factors	TX or RX
Time stability	both
Field uniformity	TX
Non-linearity	both
Thermal effect	both
Cable flexure	TX
Effect of supporting jig	TX
Reflection from the environment	TX
Multiple reflections	both
Mismatch effect	TX
Power measurement	TX
Antenna gain	TX
Probe positioning	both
Spectrum purity	TX

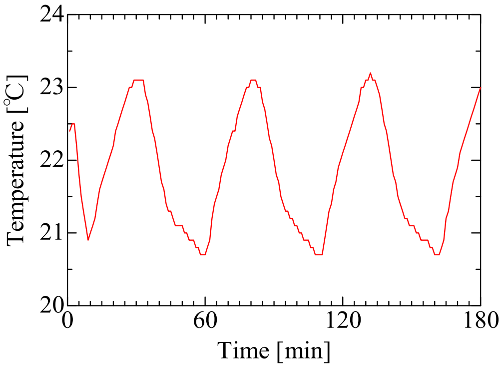

(a) Room Temperature

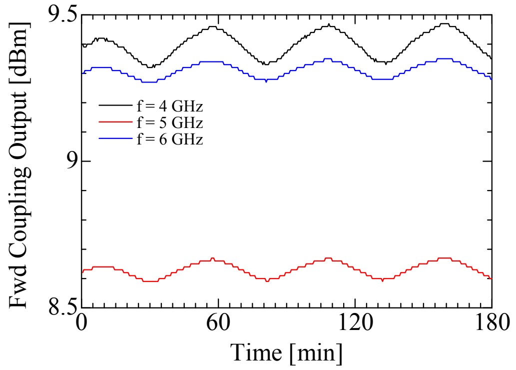

(b) Coupler Output Power

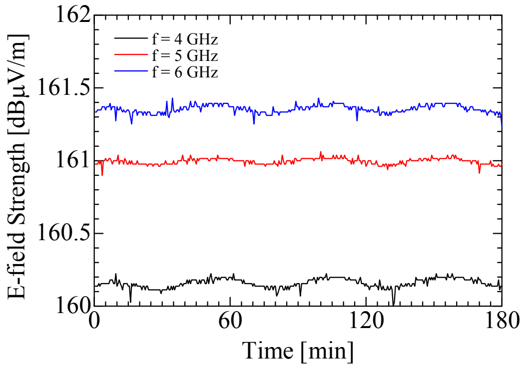

(c) Conventional Electric-Field Sensor Output

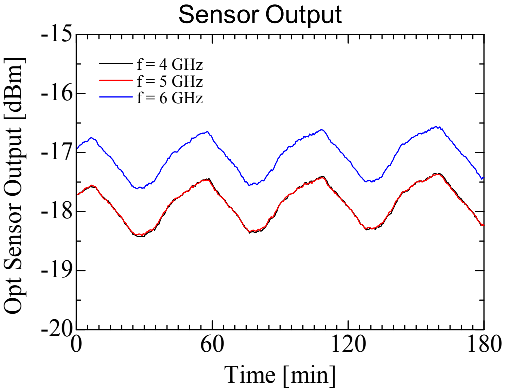

(d) Optical E-field Sensor Output with Spectrum Analyzer

Figure 2. Time-stability of calibration system and electric-field sensors

3. Performance Evalution of Calibration System and Electric-Field Sensors

For evaluating the performance of the calibration system, time-stability and field uniformity of electric-field generating system and electric field sensor itself is quite important. To check the time-stability, we measured the electric-field at same position in 3 hours. Figure 2(a) to (d) show the measured time-stability of room temperature, output power from coupler forward port, output from conventional electric-field sensor, and output from optical electric-field sensor with spectrum analyzer, respectively. The temperature stability is 22 ºC ±1 ºC. Compared to the room temperature fluctuation, the variations of the output from coupler forward port and conventional electric-field sensor are about ±0.1 dB. On the other hand, the variation of the output from optical electric-field sensor with spectrum analyzer is about ±0.5 dB. As a result, the temperature dependence of our optical electric-field sensor is higher than that of generated electric-field and conventional electric-field sensor.

To check the field-uniformity of the calibration system, we measured the 1D distribution along the *z*-axis and 2D distribution in *xy*-plane at *z* = 3000 mm. We set the x = 0 and y = 0 to the center position of standard-horn antenna and set the z = 0 mm to the antenna aperture of horn antenna. The results of 1D distribution measurement are shown in figure 3. The figure 3(a) shows the maximum electric-field strength in 4, 5 and 6 GHz from *z* = 1750 mm to 3250 mm. The figure 3(b) shows the normalized electric-field distributions in 5 GHz measured by conventional electric-field sensor and optical electric-field sensor. In both figures, the sensor is located at the center of the antenna (x = 0 mm and y = 0 mm). The simulation results calculated by MoM [3] are also shown in figure 3(b). From figure 3(a), the calibration system can generate more than 100 V/m (=160dBuV/m) electric-field at 3 m distance from the horn antenna aperture in the frequency range from 4 to 6 GHz. The non-linearity region around 164 dBuV/m is observed in the figure. From figure 3(b), the calculated results and the measured results of optical sensor quite agree each other. On the other hand, there are some discrepancies between the calculated results and the measured results of conventional electric-field sensor. These discrepancies come from the non-linearity of the conventional electric-field sensor. From these results, the linearity of the optical electric-field sensor is quite better compared to that of the conventional electric-field sensor.

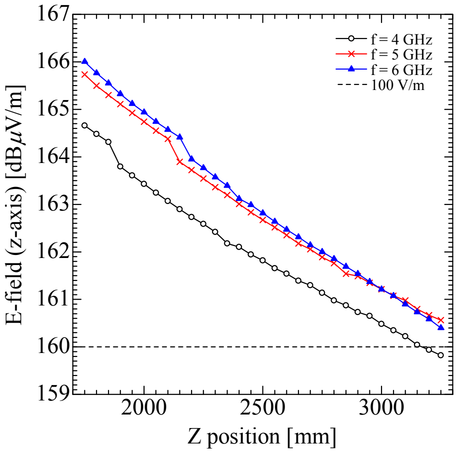

(a) Absolute electric-field strength measured by conventional sensor in dBuV/m

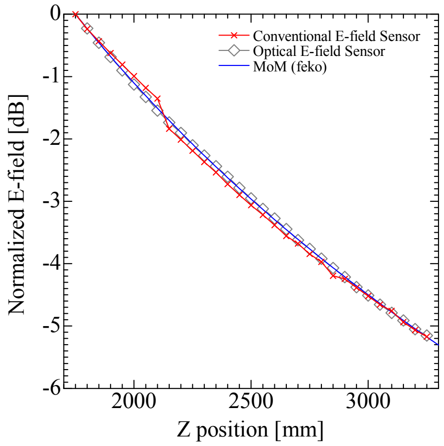

(b) Normalized electric-field of measured results and calculated results

Figure 3. 1D field uniformity evaluation in *z*-axis from *d* = 1750 mm to 3250 mm

Figure 4 shows the 2D distribution in *xy*-plane at *z* = 3000 mm in the frequency range from 4 to 6 GHz. The measured area is from –200 mm to +200 mm in both *x* and *y* direction. The MoM simulation results draw concentric circles around the center of the antenna aperture ($x = 0$ and $y = 0$). The distribution measured by the conventional sensor and optical sensor are quite different from MoM simulation results. The reasons of the difference will be explained at the presentation in detail.

4. Conclusions

In this paper, we report the results of evaluation of time-stability and field uniformity of electric-field calibration system and sensor itself. Other uncertainty factors should be evaluated for starting the calibration service of electric-field sensor in GHz-band in Japan.

References

[1] E.van Rongen, "ICNIRP exposure limits above 6 GHz", Mobile Manufacturers Forum Workshop, BIOEM 2016, 2016.

[2] IEEE Std 1309-2013, "IEEE Standard for Calibration of Electromagnetic Field Sensors and Probes (Excluding Antennas) from 9 kHz to 40 GHz., IEEE Electromagnetic Compatiblity Society, 2013.

[3] R.F. Harrington, Field Computation by Moment Methods, IEEE Press, 1993.

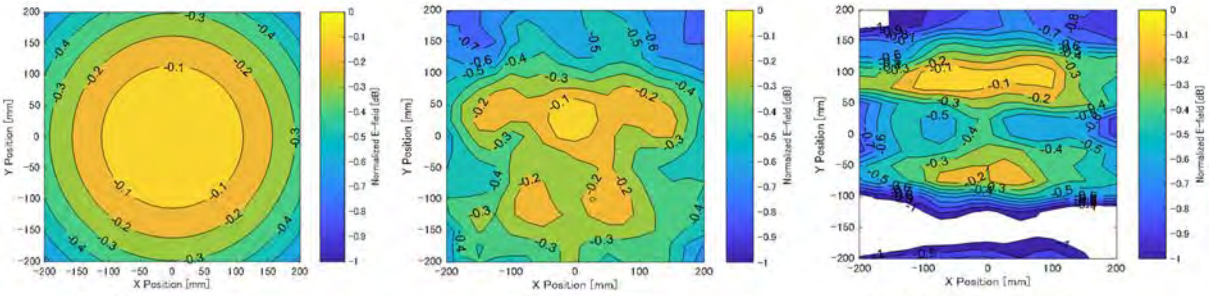

(a-1) MoM results

(a-2) Conventional E-field Sensor

(a-3) Optical E-field Sensor

(a) Frequency = 4 GHz

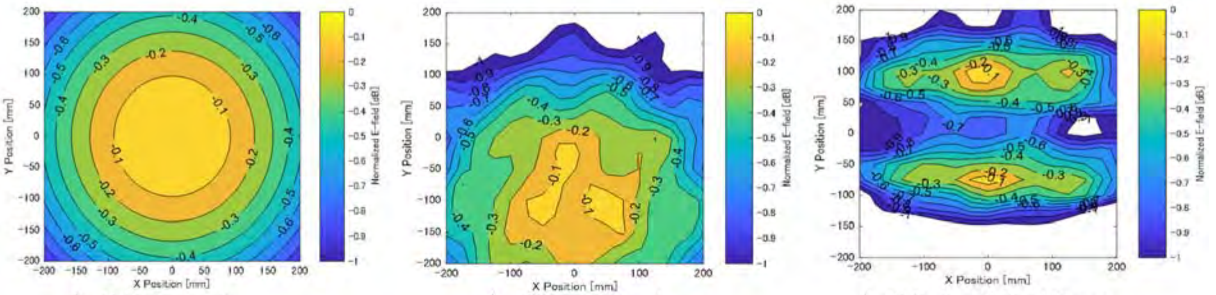

(b-1) MoM results

(b-2) Conventional E-field Sensor

(b-3) Optical E-field Sensor

(b) Frequency = 5 GHz

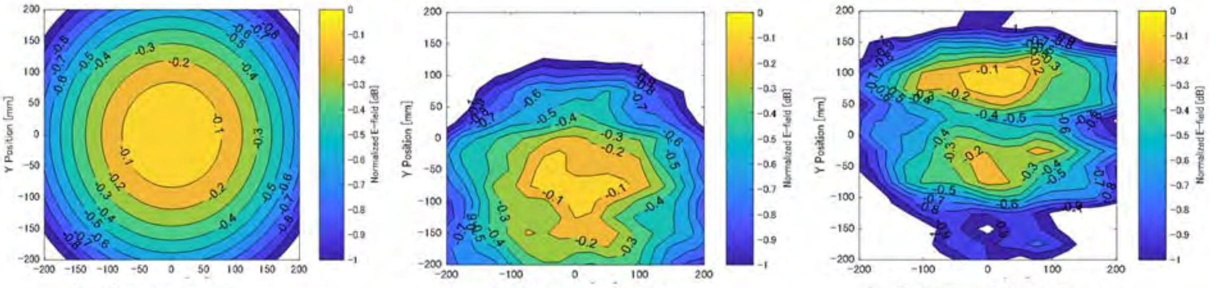

(c-1) MoM results

(c-2) Conventional E-field Sensor

(c-3) Optical E-field Sensor

(c) Frequency = 6 GHz

Figure 4. 2D field uniformity evaluation in x-axis and y-axis in the area of ±200 mm at z = 3000 mm

Development of Electro-Optic Chromophores and Polymers for Applications to THz-Wave Generation and Detection

Toshiki YAMADA[1*], Takahiro KAJI[1], Isao AOKI[1], Yoshihiro TAKAGI[1],
Chiyumi YAMADA[1], Maya MIZUNO[2], Shingo SAITO[3], and Akira OTOMO[1]
[1]Advanced ICT Research Institute, National Institute of Information and Communications Technology,
Kobe 651-2492, Japan
[2]Applied Electromagnetic Research Institute, National Institute of Information and Communications Technology,
Koganei, Tokyo 184-8794, Japan
[3]Advanced ICT Research Institute, National Institute of Information and Communications Technology,
Koganei, Tokyo 184-8794, Japan

*Corresponding author: toshiki@nict.go.jp

Abstract – After brief introduction of our recent development of new high-hyperpolarizability chromophores and electro-optic polymers, we report the dielectric properties of EO polymers in a broad band THz frequency region (90 GHz to 7 THz) by using THz-TDS as well as the absorption coefficient (α_{THz} [cm^{-1}]) of EO polymers in a broader frequency region up to 20 THz obtained by far-infrared spectroscopy (FIR). We compare the efficiency for THz-wave generation from the viewpoints of the material figure-of-merit, coherence length, and absorption coefficient between EO polymers, typical inorganic and organic EO crystals (ZnTe, $LiNbO_3$, and DAST), and discuss the advantageous points of EO polymers. We found that the EO polymer is one of the excellent materials for ultra-high speed optical modulation and THz-wave generation and detection.

Keywords – electro-optic chromophores; electro-optic polymers; THz-wave generation and detection; dielectric properties.

1. Introduction

On the past several decades, considerable attention has been paid to the development of organic and polymeric electro-optic (EO) materials due to their potential applications in ultrahigh-speed optical modulators and switches, optical interconnect technology, electric field sensing, and THz-wave generation and detection. Recent advances in the molecular design and synthesis have yielded a variety of EO polymers with high hyperpolarizability (β) chromophores and excellent thermal and chemical stability [1]. We have developed EO polymers with new high-β chromophores comprising amino-benzen with additional alkyloxy groups as the donor unit [2,3], thienyl-di-vinylene with ethylendioxy as the π-electron bridge [4], and the tricyanofuran (TCF) derivatives (TCF, CF_3-TCF, and CF_3-Ph-TCF) as the acceptor unit. Our EO polymers exhibited a large EO coefficient r_{33} and an excellent thermal stability. In this paper, we briefly introduce recent development of our EO chromophores and polymers. We also report the dielectric properties of EO polymers in a broad band THz frequency region (90 GHz to 7 THz) by using THz-TDS as well as the absorption coefficient (α_{THz} [cm^{-1}]) of EO polymers in a broader frequency region up to 20 THz obtained by far-infrared spectroscopy (FIR) [5]. We also compare the efficiency for THz-wave generation from the viewpoints of the material figure-of-merit ($FOM_{THz}=r^2n_{opt}^6/16n_{THz}$) [6], coherence length (l_c), and absorption coefficient (α_{THz} [cm^{-1}]) between EO polymers, typical inorganic and organic EO crystals (ZnTe, $LiNbO_3$, and DAST), and discuss the advantageous points of EO polymers.

2. Experimental

The synthesis procedures for our EO chromophores were shown elsewhere [2-4], and chemical structures of the EO chromophores will be shown later. β values of the EO chromophores are evaluated by Hyper-Rayleigh scattering (HRS) measurements. The apparatus used in the experiment and procedure for HRS were described in detail elsewhere [2-4].

The transmission ellipsometric method without an aperture was utilized for simple and reliable evaluation of electro-optic coefficient r_{33} of EO polymers [7,8] and the long-term thermal stability of r_{33} was evaluated by the same method.

The dielectric properties of EO polymers in a broad band THz frequency region (90 GHz to 7 THz) were obtained by using THz-TDS, and the absorption coefficient (α_{THz} [cm^{-1}]) of EO polymers in a broader frequency region up to 20 THz were obtained far-infrared spectroscopy.

3. Results and Discussion

Figure 1 shows the chemical structures of the EO chromophores used in our studies. Table 1 show β values obtained from the HRS measurements and the maximal absorption wavelength for the EO chromophores. The typical experimental error in HRS measurements is 10 to 15%, depending on the EO chromophores. The improvement of linear and nonlinear optical properties was found in electro-optic chromophores with benzyloxy and/or ethylenedioxy compared with the chromophores without these groups. The data obtained from HRS, absorption spectrum, and ^{1}H-NMR measurements indicate the improved structural stability of π-conjugation unit, which may be induced by intra-molecular hydrogen bounding and/or the steric effect.

Using EO polymers with the new EO chromophore comprising amino-benzen with a benzyloxy group as the donor unit, thienyl-di-vinylene as the π-electron bridge, and the tricyanofuran-based acceptor unit (CF_3-Ph-TCF), we obtained a large EO coefficient r_{33} of about 100 pm/V [8]. Furthermore, for the high-Tg side-chain EO polymers, we found an excellent long-term thermal stability of EO activity in the poled polymers by the Telcordia GR-468 high temperature storage test, in which test EO coefficient is measured for 2000 hours for the poled polymers stored at 85ºC.

Figures 2(a) and 2(b) show the refractive index and absorption coefficient for a side-chain EO polymer, in which the chemical structure of the side-chain EO polymer is also illustrated. We focus on the refractive index at around 100 GHz. The refractive index at around 100 GHz is 1.75 to 1.8 for the side-chain EO polymer. The refractive index at the optical wave (1.532 mm) for the side-chain EO polymer is 1.683. We found that the refractive index at around 100 GHz

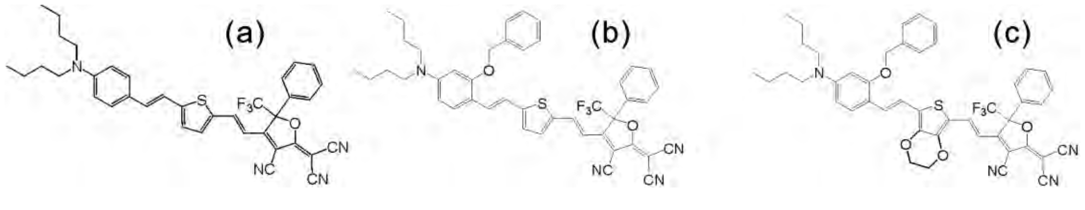

Figure 1. Chemical structures of EO chromophores

Table 1. Hyperpolarizabilities and maximal absorption wavelength of EO chromophores

Sample	β_{HRS} (10^{-30} esu) (@1952 nm)	β_{zzz} (10^{-30} esu) (@1952 nm)	$\beta_{0,zzz}$ (10^{-30} esu)	$\beta_{EO,zzz}$ (10^{-30} esu) (@1.55 μm)	λ_{max} (nm)
(a)	1090	2630	798	1310	780
(b)	1660	4010	950	1670	823
(c)	1930	4660	988	1780	839

β_{zzz} was calculated by the relation $\beta_{zzz}=(35/6)^{1/2}\beta_{HRS}$. The two-state model was assumed to obtain $\beta_{0,zzz}$ at zero frequency. The hyperpolarizability $\beta_{EO,zzz}$ for electro-optic (EO) effect ($\beta_{zzz}(-\omega,\omega,0)$) under the two-state model was calculated from the $\beta_{0,zzz}$, using the relation $\beta_{EO,zzz}=\beta_{0,zzz}\omega_{eg}^2(3\omega_{eg}^2-\omega_{EO}^2)/(3(\omega_{eg}^2-\omega_{EO}^2)^2)$, where ω_{eg} and ω_{EO} are transition angular frequency and angular frequency of optical wave used for EO, respectively.

is a little larger than that at the optical wave, and the difference between the two is approximately 8%. The near match of the intrinsic material indices at 100 GHz and the optical wave is highly desirable for velocity matching between the modulation microwave and optical wave for ultra-high speed EO modulation. We focus on the absorption coefficient at around 100 GHz for the side-chain EO polymer. The data indicates that the loss of microwaves around at 100 GHz by the intrinsic materials is very small. This characteristic is also desirable for ultra-high speed EO modulation.

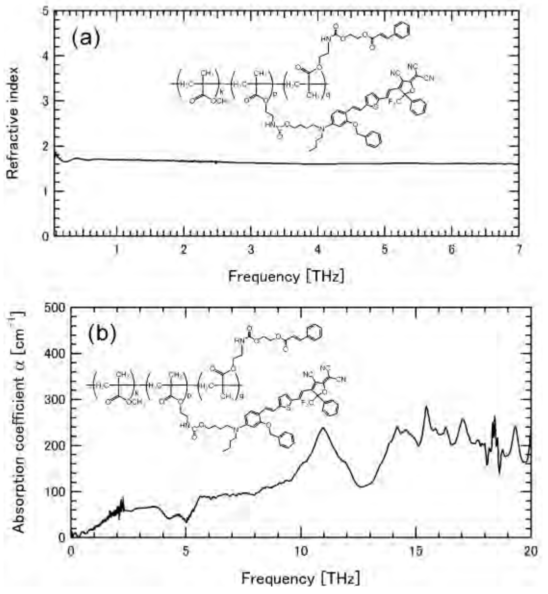

Figure 2. (a) refractive index and (b) absorption coefficient α_{THz} [cm^{-1}] for a side-chain EO polymer

We examine on the frequency dispersion of the refractive index n_{THz} in the broad frequency region (90 GHz to 7 THz). n_{THz} tends to decrease slightly when the frequency increases with being about 1.6 at the highest frequency (7 THz) in this study. The difference between n_{opt} and n_{THz} is very small. Thus, better phase matching between the THz wave and optical wave is expected, which leads to a longer coherence length. Therefore, the EO polymer with a large electro-optic coefficient is one of the promising materials for THz generation and detection. We also examine the absorption coefficient (α_{THz} [cm^{-1}]) in the broad frequency region (90 GHz to 20 THz). The EO polymer has broad absorption bands, although α_{THz} in the low THz frequency region is small. The structure of main-chain polymer may need to be reconsidered, especially for application in long THz waveguide devices.

Finally, we compare the efficiency for THz-wave generation from the viewpoints of the material figure-of-merit, coherence length, and absorption coefficient between EO polymers, typical inorganic and organic EO crystals (ZnTe, $LiNbO_3$, and DAST). We found that EO polymer is an advantageous material from these viewpoints.

4. Conclusions

We designed and developed new high β EO chromophores utilizing the intramolecular hydrogen bonding and steric effect. The poled polymer with the new EO chromophore showed a large EO coefficient r_{33} of about 100 pm/V. For the high-Tg side-chain EO polymers, we found an excellent long-term thermal stability of EO activity. We investigated the dielectric properties of EO polymers in a broad band THz frequency region (90 GHz to 7 THz) by using THz-TDS as well as the absorption coefficient (α_{THz} [cm^{-1}]) of EO polymers in a broader frequency region up to 20 THz obtained by far-infrared spectroscopy (FIR). The data indicate that EO polymer is one of the excellent materials for ultra-high speed optical modulation and THz wave generation and detection.

References

[1] Dalton LR, Sullivan PA, and Bale DH. Electric Field Poled Organic Electro-Optic Materials: State of the Art and Future Prospects. Chem. Rev. 2010; 100(1): 25-55.

[2] Yamada T, Aoki I, Miki H, Yamada C, and Otomo A. Effect of Methoxy or Benzyloxy Groups Bound to an Amino Benzene Donor Unit for Various Nonlinear Optical Chromophores as Studied by Hyper-Rayleigh Scattering. Mater. Chem. Phys. 2013; 139: 699-705.

[3] Yamada T, Miki H, Aoki I, and Otomo A. Effect of Two Methoxy Groups Bound to an Amino Benzene Donor Unit for Thienyl-di-vinylene Bridged EO Chromophores. Opt. Mater. 2013; 35: 2194-2200.

[4] Yamada T, Aoki I, Yamada C, and Otomo A. Important Role of the Ethylenedioxy Group Bound to the Thienyl-di-vinylene π-conjugation Unit of Tricyanofuran-Based Donor-Acceptor Electro-Optic Chromophores. Opt. Mater. Express 2016; 6(9): 3020-3035.

[5] Yamada T, Kaji T, Aoki I, Yamada C, Mizuno M, Saito S, Tominari Y, Tanaka S, Otomo A. Terahertz Time Domain and Far-Infrared Spectroscopies of Side-Chain Electo-Optic Polymers. Jpn. J. Appl. Phys. 2016; 55: 03DC11-1-5.

[6] Dalton LR, Günter R, Jazbinsek M, Kwon OP, Sullivan PA. Organic Electro-Optics and Photonics, chapter 10, pp.234-238; Cambridge, UK: Cambridge University Press; 2015.

[7] Yamada T, Otomo A. Transmission Ellipsometric Method without an Aperture for Simple and Reliable Evaluation of Electro-Optic Properties. Opt. Express 2013; 21(24): 29240-29248.

[8] Yamada T, Otomo A. Usefulness of Transmission Ellipsometric Method for Evaluation of Electro-Optic Materials. IEICE Trans. Electron. 2015; E98-C(2): 143-146.

Measurement of Electric Fields from Devices in Intermediate Frequencies Using an Optical Sensor

Kanako WAKE[1*], Jerdvisanop CHAKAROTHAI[1],Takuji ARIMA[2], Toru UNO[2],
and Soichi WATANABE[1]

[1]Electromagnetic Compatibility Laboratory, National Institute of Information and Communications Technology,
* Tokyo 184-8795, Japan
[2]Graduate School of Engineering, Tokyo University of Agriculture and Technology, Tokyo 184-8588, Japan
Corresponding author: kana@nict.go.jp

Abstract –Recently, there are growing concern about possible health effect of electromagnetic fields in intermediate frequency (IF) band due to the widespread use of the equipment operating in these frequencies such as wireless power transfer (WPT) systems, induction heating (IH) hobs, electronic article surveillance (EAS) systems and so forth. In this study, we constructed electric field measurement system with optical electric field sensor and measured near-field of two types of fabricated WPT systems. Measured electric fields were compared to that evaluated with numerical simulation.

Keywords – intermediate frequency; optical electric field sensor; dosimetry; wireless power transfer

1. Introduction

Recently, the devices using radio waves in the intermediate frequency band (300 Hz – 10 MHz) are increasing such as wireless power transfer (WPT) systems, induction heating (IH) hobs, electronic article surveillance (EAS) systems and so forth. A large electric power in the order of kW is sometimes applied to those systems. In consequence, a strong electromagnetic (EM) near-field can be produced around the system. Therefore, the confirmation of the exposure level to biological body is essential.

International guidelines have been established for the safety use of radio waves [1][2]. In the intermediate frequency band, there are two major biological effects needed to be considered as direct effects. One is a thermal effect defined in terms of specific absorption rate (SAR) for a frequency higher than 100 kHz. The other is a stimulus effect defined in terms of induced electric field strength for a frequency lower than 10 MHz. Incident electric and magnetic field strength are also defined as reference level, since the SAR and induced electric field inside biological bodies are difficult to evaluate.

We have measured EM fields around our fabricated WPT system and calculated induced electric field and SAR inside human in the vicinity of the system [3][4]. We found that the maximum allowable input power (MAIP) for EM reference level are much lower than that for basic restrictions. Especially the limitation due to incident E field is dominant for MHz band WPT systems. In the guidelines, limitation of contact current is also defined as indirect effect. The electric field reference levels for general public exposure up to 10 MHz is shown to prevent adverse indirect effects (contact current) for more than 90% of exposed individuals. Therefore, evaluation of electric fields around those systems is also important.

In this study, we constructed electric near-field measurement system with optical electric field sensor and measured the incident electric fields in the vicinity of WPT systems operating in MHz band.

2. Measurement System

We have constructed a electric near-field measurement system as shown in Fig, 1.

Electric field is measured with optical electric field sensor (Seikoh Giken, SH- 03EX) having three antennas arranged in the mutually perpendicular directions [5]. |S21| between power supply to the WPT systems and output of the optical electric field sensor is measured with a vector network analyzer (Agilent, E5071C). The system also contains a PC to acquire data and to control three-dimensional positioner. This system allows us to measure not only amplitude but also phase for each axis.

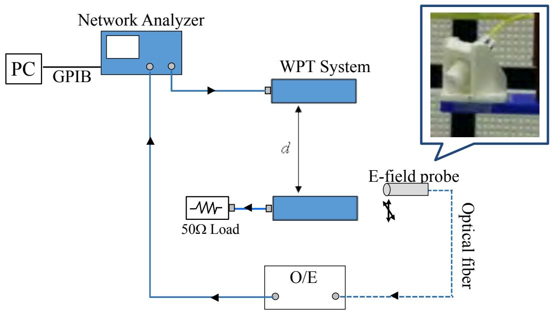

Figure 1. Measurement system for electric field.

3. Measurement Condition

We have fabricated two types of WPT systems operating around 10 MHz. Figure 2 shows (a) solenoid-type and (b) spiral-type WPT systems. The solenoid-type WPT system is composed of two single loops for feed and load terminals, and two 6-turn solenoidal coils having a radius of 30 cm and a height of 20 cm. The spiral-type WPT system consists of two single loops and two 13-turn spiral coils. Power transfer efficiency with the spacing of transmitting and receiving coils of 20 cm is summarized in Table 1.

Figure 3 illustrate the measurement region assuming human stand in the vicinity of the systems. Electric fields are measured in a volume of 35 x 70 x 180 cm^3 with measurement interval of 5 cm. The distance from the system to the measurement region was 20 and 15 cm for solenoidal type and spiral type, respectively. The input power was 1 W.

Table 1. Resonant frequency and efficiency of fabricated WPT systems.

System	Frequency [MHz]	Efficiency [%]
Solenoid	8.62	83
	9.79	79
Spiral	6.35	94
	7.74	90

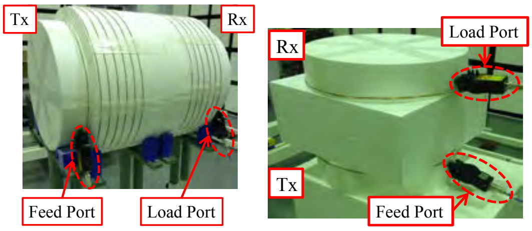

(a) Solenoidal type (b) Spiral type

Figure 2. Fabricated WPT systems.

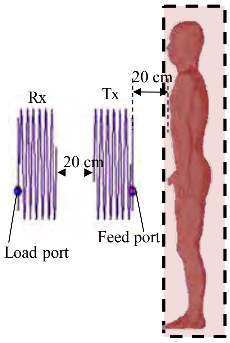

Figure 3. Illustration of measurement region.

4. Results

Figure 4 shows distributions of measured electric field (a) Ex, (b) Ey, and (c) Ez, in the vicinity of the spiral type WPT system at 6.35 MHz. In Fig. 4, the measured distributions for both magnitude and phase were compared with those of numerically calculated by method of moments. It was observed that both measured and calculated distributions are in good agreement for both amplitude and phase of each component.

The values of measured and calculated were compared with the reference levels and shown in Fig. 5. For the spiral type WPT system, differences in maximum value are 36.2 and 43.6 % at 6.35 and 7.74 MHz, respectively. The differences are 33.9 and 37.1 % at 8.62 and 9.79 MHz for solenoidal type. The difference may be attributed to fabrication errors of the WPT coils.

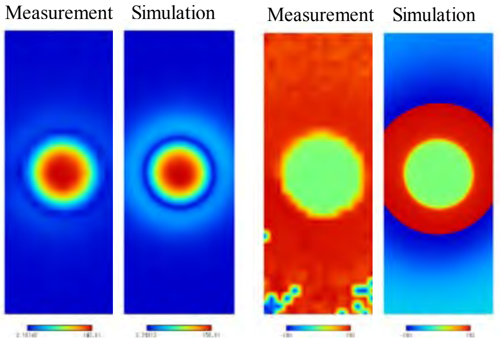

(a) Ex

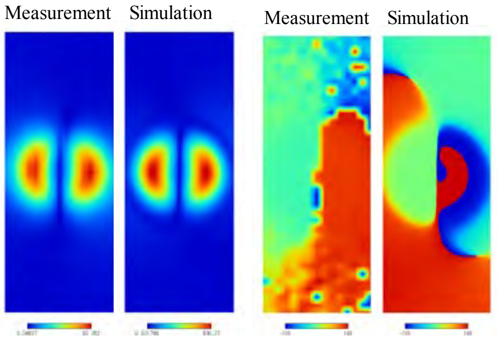

(b) Ey

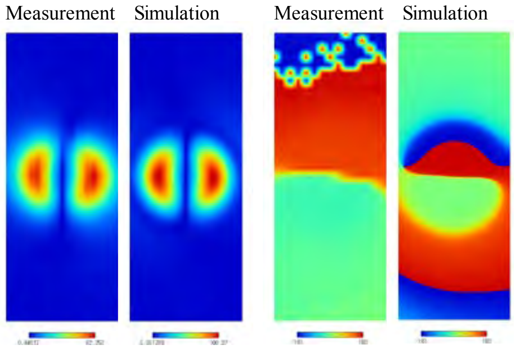

(c) Ez

Figure 4. Distributions of amplitude and phase measured and calculated at 6.35 MHz for spiral type WPT system.

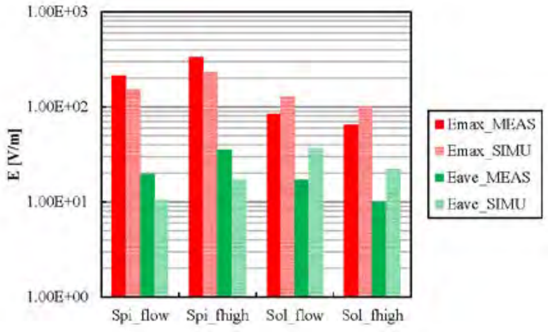

Figure 5. Comparison of measured electric field values to calculated ones.

5. Conclusion

We have constructed near-field measurement system with the electric field optical sensor. This system allows us to measure three directional distributions of both amplitude and phase. Electric near-field radiated from the WPT systems were measured with the system and compared with the numerically calculated ones.

References

[1] ICNIRP, "Guidelines for limiting exposure to time-varying electric, magnetic and electromagnetic fields (Up to 300 GHz)," Health Physics, vol. 74, no. 4, p. 494-522, 1998.

[2] ICNIRP, "Guidelines for limiting exposure to time-varying electric and magnetic fields (1 Hz to 100kHz)," Health Physics, vol. 99, p. 818-836. 2010.

[3] J. Chakarothai et al., "Exposure assessment of two different types of wireless power transfer systems at MHz-frequency band," BioEM2015, PB-40, p. 410, 2015.

[4] J. Chakarothai et al., "Electromagnetic near-field measurement system for safety evaluation of wireless power transfer system, " Korea-Japan Joint Conference on EMT/EMC/BE, pp. 183-186, 2015.

[5] B. Loader et al., "Development of optical electric field sensors for EMC measurement," EMC'14 Tokyo, 16P3-H1, pp. 659-661, 2014.

Non-Invasive Temperature Elevation Measurement under Millimeter Wave Exposure with Transparency Phantom Including Micro-Encapsulated Thermo-Chromic Liquid Crystals

Yukihisa SUZUKI[1*]
[1]Graduate School of Science and Engineering, Tokyo Metropolitan University,
1-1, Minamiosawa, Hachioji, Tokyo, 192-0397, Japan
*Corresponding author: y_suzuki@tmu.ac.jp

Abstract – A new non-invasive method to measure the temperature distribution due to high frequency electromagnetic field power absorption is proposed. A micro-encapsulated thermo-chromic liquid crystal (MTLC) is employed as the temperature probe because of its nature of high resolution and high sensitivity. In this paper, we show the temperature visualization with transparency phantom including MTLC for the dosimetry under millimeter-wave exposure. As the preliminary investigation, a non-linear coordinate transformation method and a feedforward neural network method are examined to quantify the temperature distribution from the visualization image.

Keywords – millimeter-wave; micro-encapsulated thermo-chromic liquid crystal; temperature visualization; feedforward neural network

1. Introduction

Millimeter-waves (MMWs) exposure causes highly localized temperature elevation in the surface of biological tissues, because the penetration depth of MMWs is smaller than 1 mm into the biological tissues [1]. In order to measure this local temperature change, micro-encapsulated thermo-chromic liquid crystals are proposed as the method of temperature measurement [2]. The diameter of MTLC is about 20 to 30 micrometers. The cholesteric liquid crystal, which has suitable nature of high resolution and high sensitivity to detect the changes of temperature, is encapsulated within urea resin or gelatin capsule. Wavelength of scattered light from MTLC is changes as the environmental temperature surrounding MTLCs. Therefore temperature distribution is observed by the color image.

The purpose of this study is to show the feasibility of MTLC method to detect the temperature distribution changes due to MMW frequency band exposures. in situ experiments are performed with transparency gel phantom to visualize the temperature elevation, and temperature distribution is tried to quantify by a non-linear coordinate transformation method and a feedforward neural network method.

2. Experimental Setup

MTLCs, which is produced by Japan Capsular Products, used in this experiment is toned depending on the environment temperature from 25 to 30°C. This MTLC scatters red light at 25°C and scatters blue light at 30°C for the observation angle of 90° to the incident direction of the slit light.

Transparency gel phantoms containing MTLCs are made for this experiment. This phantom is composed of 0.06 wt% MTLC, 2.0 wt% carrageenan, 30.0 wt% sucrose, 0.5 wt% KCL and 67.5 wt% water. It has a cuboid form with the size of 50 mm × 50 mm × 45 mm, and is sustained by itself without any container. Here, "carrageenan? denotes the material which is extracted from seaweed and has high transparency.

Figure 1 shows the block diagram of the exposure system that was used in this preliminary experiment. One of the lateral surfaces of the phantom is irradiated by 40 GHz MMWs with an open-ended waveguide.

The schematic view of measurement setup is shown in Fig. 2. The distance between the phantom and the open-ended waveguide is 5 mm. We irradiated 40 GHz MMWs whose input power into the open-ended waveguide

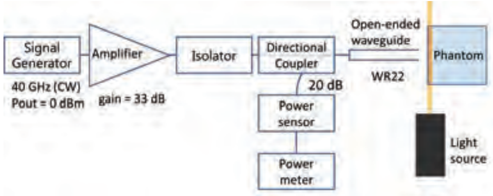

Figure 1. Block diagram of the exposure setup.

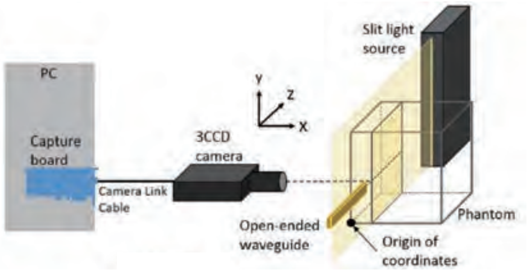

Figure 2. Schematic view of the exposure experiment for the visualization of temperature distribution inside the transparency phantom.

is 27.9 dBm. The inner cross-section of phantom was illuminated by a slit light. The change of MTLC's coloring distribution was recorded by a digital camera. The slit light source was located at the counterposition of open-ended waveguide as shown in Fig. 2.

3. Visualization and Quantification of Temperature Distribution

Figure 3 shows an example of visualization of temperature distribution inside the transparency phantom at 600 s from the onset of exposure. The penetration depth is approximately 500 μm for the high water content phantom exposed to 40 GHz MMW. It is found that temperature distribution caused by conduction, whose heat source is absorbed power of MMW, is visualized in the relatively tiny area of 10.3 × 4.6 mm.

In this study, a feedforward neural network (NN) as shown Fig. 4(a) is examined to quantify temperature distribution from recorded visualized images. A NN is composed by one input layer, one hidden layer and one output layer, and each layer has 4 (including a bias unit), 1000, and 1 units, respectively. Temperature distribution estimated by NN is shown in Fig. 4(b).

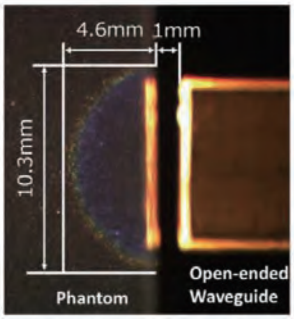

Figure 3. An example of visualization of temperature distribution inside the phantom.

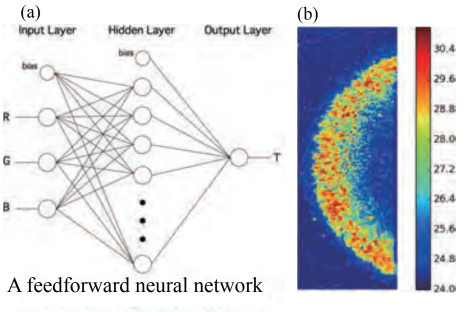

Figure 4. Quantification of temperature distribution by a feedforward neural network. (a preliminary study)

4. Conclusion

We have examined temperature visualization caused by MMW exposure with non-destructive MTLC method. As an preliminary investigation, quantification of temperature distribution inside phantom is performed by the feedforward NN, and the feasibility of this method is shown.

References

[1] O. P. Gandhi, A. Riazi, "Absorption of Millimeter Waves by Human Beings and its Biological Implications," IEEE Transactions on Microwave Theory and Techniques, Vol. 34, pp.228-235, 1986.

[2] Y. Suzuki, M. Taki, K. Fukunaga, and S. Watanabe, "Imaging the 3D Temperature Distributions Caused by Exposure of Dielectric Phantoms to High-Frequency Electromagnetic Fields," IEEE Transactions on Dielectrics and Electric Insulation, Vol. 13, pp.744-750, 2006.

Silicon Photonic Resonator for Sensitive Bio-Sensing Applications

Ukrit MANKONG[1,2*], Nattapol ITTHIPRATHEEP[1], Suruk UDOMSOM[3],
Toshimasa UMEZAWA[2], Atsushi MATSUMOTO[2], and Naokatsu YAMAMOTO[2]
[1]Department of Electrical Engineering, Faculty of Engineering, Chiang Mai University, Thailand
[2]National Institute of Information and Communications Technology, Tokyo, Japan
[3]Biomedical Engineering Program, Faculty of Engineering, Chiang Mai University, Thailand
*Corresponding author: ukrit.m@cmu.ac.th

Abstract – Recently there have been great interests in applying silicon photonic resonator in bio-sensing, it has potential to achieve high sensitivity. Bio-sensing applications rely on the principle of changing the effective refractive index of silicon waveguide resulting in resonant wavelength shift. In this paper, we discuss the design factors affecting the sensing sensitivity include coupling efficiency between input or output waveguides and the resonating cavity as well as the cavity effective refractive index change. Then we measure the results on our resonators comparing with simulations. The procedure to coat antibody for bio-analyte detection is also outlined and demonstrated.

Keywords – Silicon photonic; silicon photonic resonator; biosensor; resonator based sensor

1. Introduction

Silicon photonic resonator based devices have received attention recently in bio-sensing applications. The resonant wavelength shift of the resonator is responsive to the effective refractive index change occurred through bio-material binding at the sensor surface such as antibody-antigen binding. This technique is called label-free sensing as opposed to the label sensing using fluorescent dye. The label-free sensing is quantitative and more sensitive to the concentration of the target bio-analyte, thus it is promising to be used in early diagnosis [1-3].

Resonator for bio-sensing purpose should satisfy the design requirement in two aspects. Firstly, the sensor should have high quality factor with large extinction ratio. Secondly, the interaction of the combined receptor molecules and the target bio-analyte with light in the resonator cavity should be high. This paper presents the discussion of the issues in silicon photonic ring resonator design and fabrication in the context of bio-sensing. We present the simulated and measurement results of our racetrack ring resonators with large coupling gap between silicon nanowires, thus the device can be fabricated using low resolution lithography.

2. Theory

Silicon photonic ring resonator has the advantage of high index contrast between silicon nanowire which has refractive index of 3.45 and the oxide cladding (SiON or SiO_2) with refractive index of approximately 1.5. The theory of standard ring resonator is well established where, due to phase-matching condition, the resonant wavelengths (λ_m) and free-spectral range (FSR) depend on the effective index (n_{eff}), group refractive index (n_g) and the length (L) of the resonant cavity as in the following relationships,

$$\lambda_m = n_{eff} L / m, \tag{1}$$

$$FSR = \lambda_m^2 / n_g L. \tag{2}$$

In sensing application, large quality (Q) factor is desirable since the wavelength shift can be detected more precisely. The Q factor is typically defined as the ratio of the stored energy to energy loss per round trip and it indicates the width of the resonant peak. The Q factor depends on the coupling coefficient from waveguide to the resonator and the intrinsic loss of resonator as the followings,

$$Q = \left[\frac{\lambda_0}{2\pi} \left(\frac{\alpha}{n_g} + \frac{|\kappa|^2}{\tau_{rt}} \right) \right]^{-1}, \qquad (3)$$

where λ_0 is the cavity free-space resonance wavelength, α is the loss coefficient of the cavity, κ is the coupling coefficient and τ_{rt} is the roundtrip propagation time.

3. Challenges in Silicon Photonic Resonator in Bio-Sensing Applications

3.1. Waveguide to Resonator Cavity Coupling

As summarized in the previous section, coupling coefficient is among the design parameters that need to be considered. In traditional CMOS fabrication with low resolution lithography, the gap between Si nanowires, parameter g as shown in Figure 1, can be rather large in the order of 0.3-0.5 µm. Longer coupling section is required for larger gap which results in racetrack design.

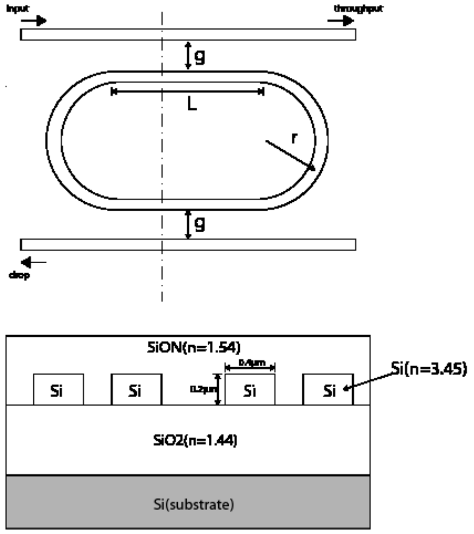

Figure 1. Top view and cross-section of a racetrack Si Photonic ring resonator.

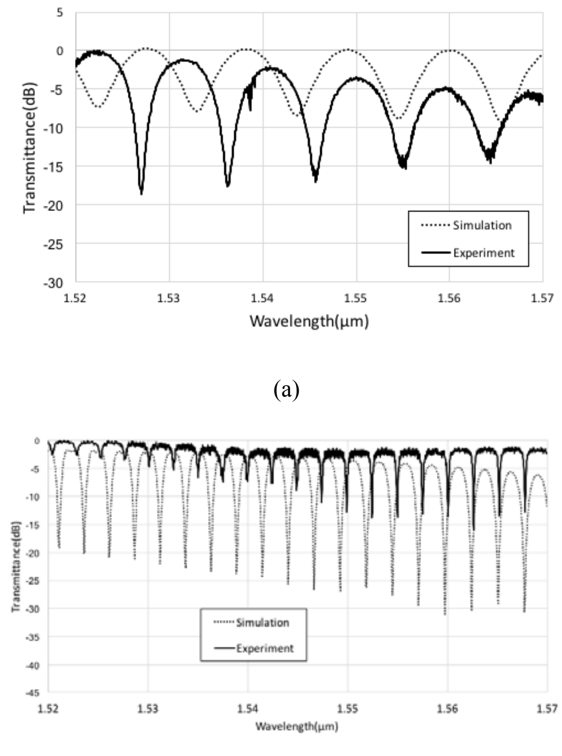

(a)

(b)

Figure 2. Experimental results of silicon ring resonator with coupling gap (a) 0.3 µm and (b) 0.5 µm

We have fabricated and measured device performance of such design. Our devices use edge coupling by spot size converter using inverted taper coupler design to minimize fiber to chip loss. The results are shown in Figure 2 (a) and (b) for two coupling gaps, 0.3 and 0.5 µm, compared with simulated results using commercial OptiFDTD software. Note that with larger gap, longer coupling length is required which also results in longer resonant cavity and narrower free spectral range. Large Q factor can be achieved but careful design is required between coupling coefficient and cavity loss which has been increased.

3.2. Evanescent Field Interaction with Target Biomaterial

The principle of bio-sensing relies on interaction of optical field with the combined antibody and bio-analyte, which then causes changes in effective refractive index. Thus we can simulate to the wavelength shift to the percentage change of refractive index, as shown in Figure 3, for two extreme cases, i.e. when the resonator cavity refractive index is changed and when the cladding refractive index is changed. The slope of $\Delta\lambda / \Delta n$ reflects how sensitive the sensor is. For actual sensing we can expect the slope to be between these two cases. To increase the sensitivity it is important to increase the interaction area, i.e. the antibody and bio-analyte binding surface.

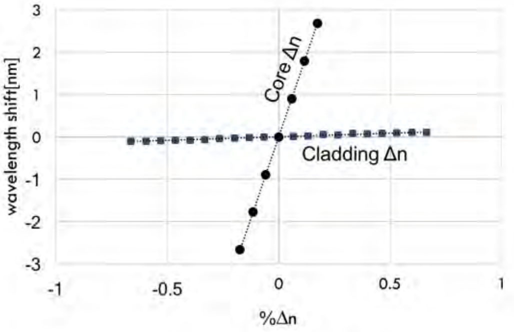

Figure 4. Wavelength shift due to ring resonator and cladding refractive index change

4. Procedure of Antibody Coating

In this section we summarize a procedure of antibody coating onto silicon resonator. The silicon device surface is cleaned in methanol and 1 M HCl at room temperature and thoroughly rinsed with deionized water. The salinization procedure is then performed by applying the method in [4]. Initially, the cleaned silicon device is immersed in 10% 3-aminopropyl-triethoxysilane (APTES) in ethanol and a small amount of deionized water at room temperature over a long period Figure 5 (a). These sensors would be rinsed with deionized water and dried. Then, the silanized silicon devices will be coupled with 2.5% glutaraldehyde (GA) and 160 mM sodiumcyanoborohydride in PBS, pH 7.4 at room temperature and will be wash with deionized water. The APTES-GA modified Silicon devices is then immersed in antibody solution, in our case we use anti-human IgG antibody, at room temperature, excess antibody is washed out by phosphate buffer saline (PBS). We then achieved functionalized silicon resonator as in Figure 5 (b), which is ready for bio-analyte detection.

5. Acknowledgment

The author would like to thank Joint Research Laboratory for Photonic Network of NICT Asia Center and Dr. Tuptim Angkaew and her student for facilitating our measurement.

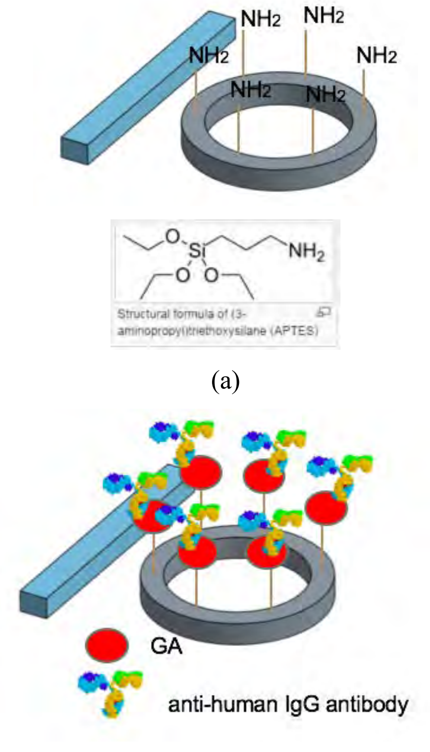

(a)

(b)

Figure 5. Antibody coating procedure

References

[1] Y. Q. Chen, F. Yu, C. Yang, J. Y. Song, L. H. Tang, M. Y. Li, *et al.*, "Label-free biosensing using cascaded double-microring resonators integrated with microfluidic channels," *Optics Communications,* vol. 344, pp. 129-133, Jun 1 2015.

[2] E. Skotadis, K. Voutyras, M. Chatzipetrou, G. Tsekenis, L. Patsiouras, L. Madianos, *et al.*, "Label-free DNA biosensor based on resistance change of platinum nanoparticles assemblies," *Biosensors & Bioelectronics,* vol. 81, pp. 388-394, Jul 15 2016.

[3] M. K. Park, J. S. Kee, J. Y. Quah, V. Netto, J. F. Song, Q. Fang, *et al.*, "Label-free aptamer sensor based on silicon microring resonators," *Sensors and Actuators B-Chemical,* vol. 176, pp. 552-559, Jan 2013.

[4] P. Saengdee, W. Chaisriratanakul, W. Bunjongpru, W. Sripumkhai, A. Srisuwan, C. Hruanun, *et al.*, "A silicon nitride ISFET based immunosensor for Ag85B detection of tuberculosis," *Analyst,* vol. 141, pp. 5767-5775, 2016.

Microphotonic Voltage Probe Used in MRI Environments for Medical Implant Immunity Testing

Sven KUEHN[1,3*], Livio PONATO[1], Oliver MUNZ[1], Maria CABANES[2] ,
and Niels KUSTER[3,4]
[1]Schmid&Partner Engineering AG (SPEAG), 8004 Zurich, Switzerland
[2]ZMT Zurich MedTech AG (ZMT), 8004 Zurich, Switzerland
[3]Foundation for Research on Information Technologies in Society (IT'IS), 8005 Zurich, Switzerland [4]Swiss Federal Institute of Technology Zurich (ETHZ), 8092 Zurich, Switzerland
[*]Corresponding author: kuehn@itis.ethz.ch

Abstract – Certification of active medical implants for use in magnetic resonance imaging machines requires the testing of immunity with respect to radiofrequency voltage induced into the active electronics of the implant. Immunity is tested on the bench by injection. The injection voltage must be determined under real exposure conditions. We have developed an optical differential voltage probe to be used in electromagnetically hostile environments like magnetic resonance imaging that is able to deliver the full complex-valued voltage signal with a dynamic range of 120 dB and a frequency range from 100 kHz to 1 GHz and with a total measurement uncertainty of 1.14 dB.

Keywords – implant safety; magnetic resonance imaging; MRI; immunity testing

1. Introduction

Magnetic resonance imaging (MRI) scans of a patient with an active implantable medical device (AIMD) may result in radiofrequency (RF) induced malfunction caused by the induced voltages that are coupled via the leads into the AIMD. Clause 15 of [1] describes the procedure for determination of the fields induced by elongated leads. To date, proprietary solutions provided by the implant manufacturers or relatively large external probes that monitor the induced absolute voltage [2] are available. All existing monitoring solutions lack the ability to capture the complex voltage signal required for Tier 3 evaluations according to [1].

In this paper, we present the RFoF1P4MED, which offers a completely optically isolated active differential RF probe capable of acquiring the complex voltage signal at frequencies from 100 kHz to 1 GHz. When connected to the terminals inside the AIMD, this probe enables induced RF voltages to be monitored with minimal parasitic pickup under MRI exposure conditions.

2. Sensor System Design

The system (Figure 1) uses direct laser modulation for signal transmission of the RF signals fed to the 300 kΩ, <1 pF differential input of the probe. The RFoF1P4MED probe and the remote unit are optically linked exclusively by fiber optics. A power laser is used to illuminate a photovoltaic converter inside the probe head via fiber optics. The electrical energy from the photovoltaic cell drives a small current-stabilized laser and a differential amplifier inside the sensor head. The input RF signal, amplified by the differential amplifier, modulates the optical output power of the vertical cavity surface emitting LASER (VCSEL). This signal is then transmitted to the remote unit over an optical fiber. At the remote unit, the optical signal is demodulated again by means of a fast photodiode, and the received RF signal is amplified by a transimpedance amplifier and made available via a standard 50 Ω output to connect to standard RF equipment. Calibration of the voltage probe system is accomplished by means of a calibration device (Figure 2) that enables system calibration with any standard vector network analyzer (VNA).

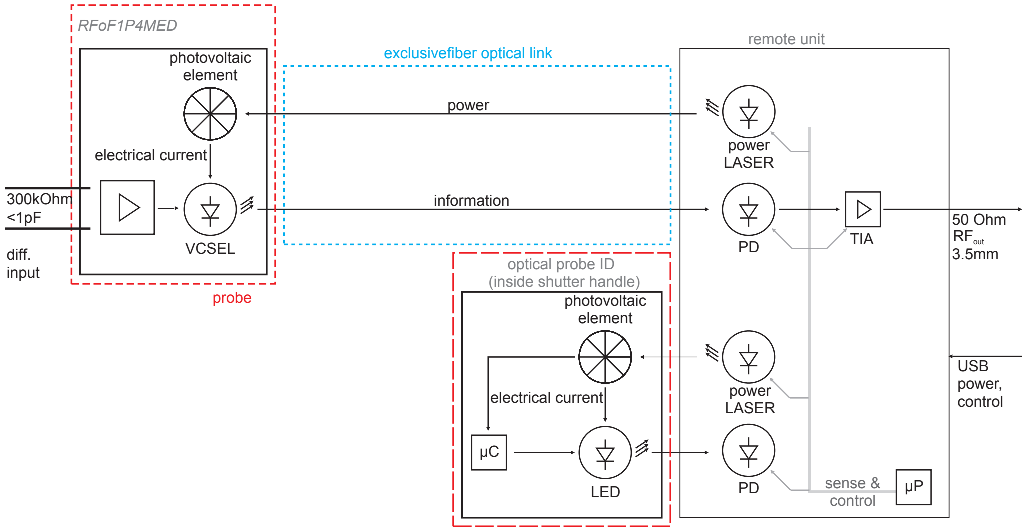

Figure 1. Schematic diagram of the RFoF1P4MED fiber-optic RF voltage probe.

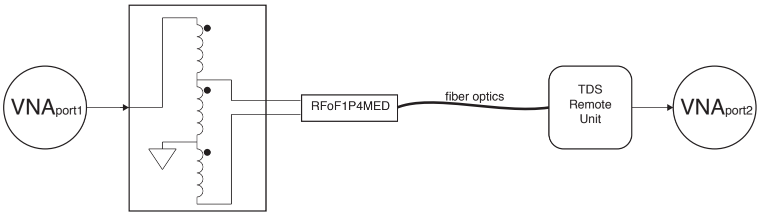

Figure 2. Schematic diagram of the RFoF1P4MED calibration setup.

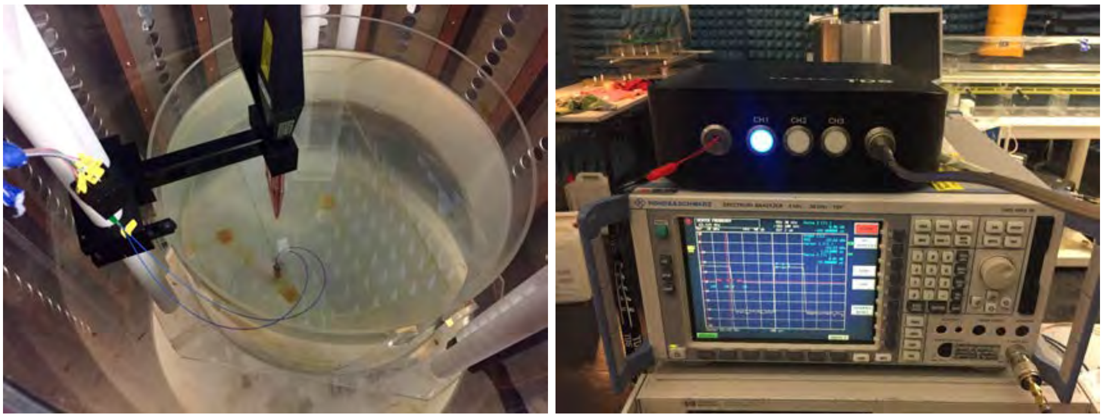

Figure 3. Left: RFoF1P4MED measurement setup inside the MITS1.5 (ZMT ZurichMedTech AG, Switzerland) MRI birdcage. Right: Measured radio-frequency signal at the output of the Remote Unit (SPEAG, Switzerland) opto-electrical converter.

3. Results

We have implemented the novel photonic voltage probe in a miniaturized design. The probe was successfully applied in the certification of a medical device according to clause 15 of [1] in a realistic MRI environment (Figure 3). The measurement uncertainty of this voltage probe system was found to be as low as 1.14 dB ($k = 1$). The overall specifications of the probe system are summarized in Table 1.

Table 1. Specifications of the RFoF1P4MED optical voltage probe system reported here.

Bandwidth (3 dB)		100 kHz – 1 GHz
Signal input		
	Connector	preci-dip 851
	Input impedance	300 kOhm
	Diff. range	± 12 V
	Noise floor	$<100\ \mu\mathrm{V}/\sqrt{Hz}$
Signal output		
	Probe	MU-duplex
	Remote Unit	50 Ohm (SMA)

4. Conclusions

We present a novel microphotonic radiofrequency voltage probe capable of acquiring the full complex-valued voltage signal under electromagnetically hostile exposure conditions. The voltage probe has been successfully applied to certify an active medical implant according to clause 15 of [1]. The overall measurement uncertainty was found to be better than 1.14 dB ($k = 1$).

References

[1] International Organization for Standardization. Draft ISO/TS 10974:2017: Assessment of the Safety of Magnetic Resonance Imaging for Patients with an Active Implantable Medical Device, 2nd ed.; ISO; 2017.

[2] Barbier T, Piumatti R, Hecker B, Odille F, Felblinger J, Pasquier C. An RF-Induced Voltage Sensor for Investigating Pacemaker Safety in MRI. MAGMA. 2014; 27(6): 539–49.

Antenna Gain Measurement System for Extrapolation Method Using Optical Fiber Link Technologies

Yuanfeng SHE*, Satoru KUROKAWA, Masanobu HIROSE, and Michitaka AMEYA

[1] National Metrology Institute of Japan (NMIJ), National Institute of Advanced Industrial Science and Technology (AIST), 305-8563, Ibaraki, Japan
*Corresponding author: yuanfeng.she@aist.go.jp

Abstract – This article shows the system variation of the gain measurement system for extrapolation method using optical fiber link technologies. The S_{21} of the standard horn antennas have been measured from 26 GHz to 40 GHz. The vibration of S_{21} by the optical system has been compared with the result by the conventional system. The system using the optical fiber link technologies has an acceptable stability.

Keywords – coaxial cable; optical fiber link; gain; extrapolation method

1. Introduction

The optical fiber link system has many advantages. The fiber is very lightweight and easy handling. The dielectric fiber can replace the metal coaxial cable and suppress the unwanted waves from the coaxial cable. The effect of the cable which distort the radiation pattern of the antenna can be avoided. And, the uncertainty of long time stability of the coaxial cable can be suppressed. [1-4]

2. System & Results

The proposed system is shown in Fig.1. The reference antenna is fixed, the antenna under test (AUT) is set on a moving rail. The distance of the antennas *D* is from 1.5 m to 4.1 m along the rail. The S_{21} of the standard horn antennas have been measured from 20 GHz to 50 GHz. 5 times have been measured at each position.

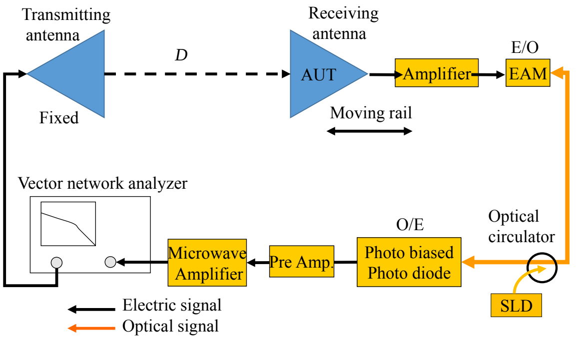

Figure 1. Extrapolation measurement system by using optical fiber link technologies

Fig.2 shows the Standard deviation of measured S_{21} at 33 GHz. This optical fiber link system is still in trial and test. Compared with the conventional system, the optical fiber system has a larger deviation but an acceptable stability.

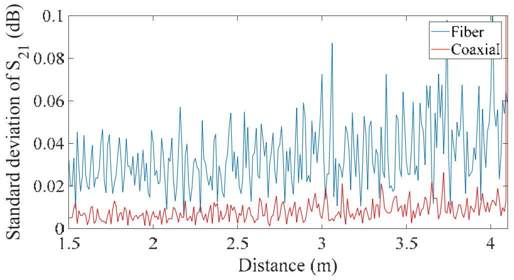

Figure 2. Standard deviation of measured S_{21} (33GHz 5 time)

References

[1] She YF, Ameya M, Hirose M, Kurokawa S, Hirokawa J, Ando M. Stability of Coaxial Cable Transmission and Measurement System Using Optical Fiber Link Technologies. Microwave Opt. Technol. Lett. 2017; 59(1): 201–204.

[2] Newell AC, Baird RC, Wacker PF, Accurate Measurement of Anetnna Gain and Polarization at Reduced Distances by an Extrapolateion Technique, IEEE Trans. On antenna and propagation, vol.AP-21, No.4, July 1973

[3] Capozzoli A, Curcio C, D'Elia G, Liseno A, Vinetti P, Ameya M, Hirose M, Kurokawa S, Komiyama K, Photonic Probes and Advanced (Also Phaseless) Near-Field Far-Field Techniques, IEEE Antennas and Propagation Magazine , vol.52, no. 5, pp 232 - 241, Oct. 2010

[4] Kurokawa S, Hirose M, Ameya M, Precision antenna measurement using optical fiber link technologies, in Proc. of CAMA 2015.

Recent Standardization Activities for Radio over Fiber Transmitter within IEC TC103 WG6 in 2017

Satoru KUROKAWA[1*] Michitaka AMEYA[1*] Junichiro ICHIKAWA[2*] Hiroyo OGAWA[3*]
Atsushi KANNO[3*], Tetsuya KAWANISHI[4*], and other members of IEC TC103WG6
1*National institute of advanced industrial science and technology (AIST), Tsukuba, Ibaraki, 305-8563 Japan
2*Sumitomo Osaka Cement CO., LTD. Funabashi, Chiba, 274-8601, Japan
3*National Institute of Information and Communications Technology, Koganei, Tokyo, 184-8795 Japan
4*Waseda University, Shinjuku, Tokyo, 169-8050, Japan
*Corresponding author: satoru-kurokawa@aist.go.jp

Abstract – This paper describes the outline of recent standardization activities for Radio over Fiber transmitter by IEC TC103WG6. Radio over Fiber transmitter consists of optical fibers, electrical to optical converter, and optical to electrical converter. IEC TC103WG6 is working on standardization on measurement method of these devices, and technical report for some applications using Radio over Fiber transmitter (totally 10 projects). This paper overviews those standardization activities which are being developed by TC103WG6 in 2017.

Keywords – Radio over Fiber transmitter, electrical to optical converter, optical to electrical converter, standardization, TC103, TC103WG6

1. Introduction

Radio over Fiber (RoF) system is widely recognized as broadband wireless signal infrastructure to shadowing areas such as the underground, the subway stations, inside the train, and inside the building. Further, RoF system can transmit and receive broadband microwave modulated light wave. For this reason, variety of RoF systems are utilized in the area of transmitting broadband microwave signal such as TV broadcasting signals, mobile phone signals, WiFi (Wireless Fidelity) signals.

IEC TC103WG6 (International Electro Technical Commission, Technical Committee 103 Working Group 6) has started standardization of RoF transmitter from 2005. The national committee of TC103WG6 has more than 9 work programs. This paper presents recent standardization activities for RoF transmitters within IEC TC103WG6.

2. Outline of Working Programs

IEC TC103WG6 standardize RoF transmitter and related technologies. This working group has 9 projects as follows;

(1) Frequency response of optical-to-electric conversion device in high-frequency radio over fibre systems - Measurement method [1].
This International Standard provides a method for measuring the frequency response of optical-to-electric conversion devices in wireless communication and broadcasting systems. The frequency range covered by this standard goes up to 100 GHz (practically limited up to 110 GHz by precise RF power measurement) and the wavelength band concerned is 0,8 μm to 2,0 μm.

(2) Measurement Method of a Half-Wavelength Voltage for Mach-Zehnder Optical Modulator in Wireless Communication and Broadcasting Systems [2]
This standard gives a measurement method of half-wavelength voltage applicable to Mach-Zehnder optical modulators in wireless communication and broadcasting systems. In addition, this method is also effective for the estimation of the intermodulation distortion of Mach-Zehnder optical modulators in the frequency range from

10 MHz to 30 GHz.

(3) Measurement Method of a Half-Wavelength Voltage and a Chirp Parameter for Mach-Zehnder Optical Modulator in High-Frequency Radio on Fibre (RoF) Systems [3]
The standard defines the measurement methods of a half-wavelength voltage and a chirp parameter which have a significant impact on the performance of RoF systems. Additionally, these methods are also used for the estimation of the intermodulation distortions and transmission performances. The half-wavelength voltage and the chirp parameter can be measured at the same time using the methods defined in this standard. The nonlinear distortion characteristics are also important for the performance of the systems. The intermodulation distortion of the MZM is calculated from the driving voltage and the half-wavelength voltage in the frequency range from 5GHz to 110GHz.

(4) System applications of radio over fibre technologies [4]
This document provides information on the current and latest applications of radio over fibre technology. Wireless communication, broadcasting, and airport multilateration systems which are already implemented or will be in the near future, are introduced. This document includes the basic concept, a brief outline and related standards of the applications of RoF technology.

(5) Radio-over-Fibre Technologies for electromagnetic field measurement - Part 1: Radio over fibre technologies for antenna measurement [5]
This document provides information on the current and latest applications for antenna measurement using radio-over-fibre technology. Antenna gain and antenna pattern measurement systems are covered, which are practically in use or will be used soon. It will be beneficial to system developers and system users in the fields of antenna measurement.

(6) Radio-over-Fibre Technologies for spectrum measurement - 100-GHz spectrum measurement equipment [6].
This document describes 100-GHz spectrum measurement methods using RoF technologies. It covers the background to measurement over 100 GHz, the configuration of a spectrum analyzer, the key technologies, such as mm-wave tunable filter, and RoF-technologies-based local oscillator, and provides some measured examples.

(7) Radio over fibre fronthaul network for train communication network [7]
This document introduces detail of a radio over fibre fronthaul network for train communication networks. A network topology of a train communication network with a radio access system is shown in the figure 1. In the proposal, network configuration based on a wavelength-division multiplexing (WDM)-RoF system is implemented to the network between the node base station and the track-side radio access units (TS-RAUs). For realization of broadband connections between the TS-RAU and the train car, broad bandwidth radio signal such as a millimeter-wave radio could be applied for realization of the capacity of 1 Gbit/s or more.

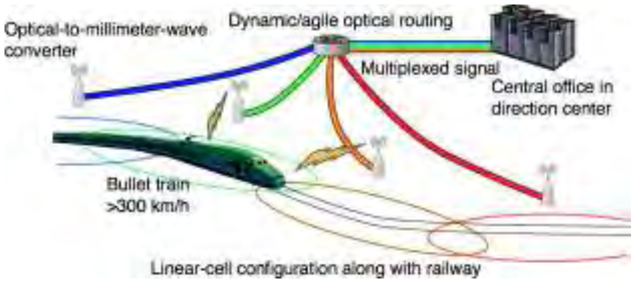

Figure 1. Schematic of millimeter-wave radio-over-fiber backbone for high-speed trains.

(8) Radio-over-Fibre Technologies and their

performance standard - Part 3: Foreign object and debris (FOD) detection radar system [8]
This standard provides the link performance of RoF which connects the central station and remote antenna stations of foreign object and debris (FOD) detection radar system. The FOD detection radar system utilizes millimeter-wave frequencies carried through the optical fibre to perform high-sensitivity and high-range resolution. The system to detect FOD on airport surfaces plays an important role in managing airport security and safety.

(9) Frequency response of optical to electrical conversion device in high frequency radio over fibre systems - Part 2 Measurement method of common mode rejection ratio of optical coherent receiver [9]
Measurement method of frequency response of common-mode rejection ratio of optical coherent receiver discusses state-of-the-art measurement method of commonly used balanced optical-to-electrical conversion devices and provides useful technical specifications for measurement of frequency responses of common-mode rejection ratio.

References

[1] IEC 62803:2016 Edition 1.0 (2016-07-12) Transmitting equipment for radiocommunication - Frequency response of optical-to-electric conversion device in high-frequency radio over fibre systems - Measurement method

[2] IEC 62801 ED1, Measurement Method of a Half-Wavelength Voltage for Mach-Zehnder Optical Modulator in Wireless Communication and Broadcasting Systems, to be published.

[3] IEC 62802 ED1, Measurement Method of a Half-Wavelength Voltage and a Chirp Parameter for Mach-Zehnder Optical Modulator in High-Frequency Radio on Fibre (RoF) Systems, to be published.

[4] IEC TR 63098-1 ED1, Transmitting equipment for radiocommunication - Radio-Over-Fibre Technologies and their performance standard - Part 1: System applications of radio over fibre technologies, to be published.

[5] IEC TR 63099-1 ED1, Transmitting equipment for radiocommunication - Radio-Over-Fibre Technologies for electromagnetic field measurement - Part 1: Radio over fibre technologies for antenna measurement, to be published.

[6] IEC TR 63100 ED1, Transmitting equipment for radiocommunication - Radio-Over-Fibre Technologies for spectrum measurement - 100-GHz spectrum measurement equipment, to be published.

[7] PNW 103-164, IEC 6XXXX-2 Ed.1.0: Transmitting equipment for radiocommunication - Radio-Over-Fibre Technologies and ther performance standard - Part 2: Radio over fibre fronthaul network for train communication network, to be published.

[8] PNW 103-166, Transmitting equipment for radiocommunication - Radio-Over-Fibre Technologies and their performance standard - Part 3: Foreign object and debris (FOD) detection radar system, to be published.

[9] PWI 103-3 ED, Transmitting equipment for Radio communication -Frequency response of optica to electrical conversion device in high frequency radio over fibre systems - Part 2 Measurement method of common mode rejection ratio of optical coherent receiver, to be published.

Generation and Control of Nonlinear and Quantum Optical Effects

A. C. AMARO DE FARIA Jr[1*]
[1]Photonics Division, Institute for Advanced Studies, 1222000 Sao Jose dos Campos, Brazil
[2]Mechanical Eng. Department, Federal Technological University of Parana, 85053525, Guarapuava, Brazil
*Corresponding author: atoni.carlos@gmail.com

Abstract – In this work we present a technique based on photonics applied to electromagnetic measurements and electromagnetic systems that are able to identify, process and transmit nonlinear optical signals and quantum optical effects from the interaction of light with matter. The photonic device developed applied to these electromagnetic measurements can generate and control the non-linear optical beams and quantum noises through the interaction of light (lasers) with matter, from optical fibers to photonic crystals.

Keywords – photonics-applied, non-linear optics, quantum optical scattering, optical potential

1. Introduction

A specific waveguide can be projected for generation, control and sensing of nonlinear optical beams. The waveguide crystal lattice generates and keep the nonlinear optical pulses that propagates through the guide. Quantum effects such as the Raman and Brillouin scattering add up to the nonlinear effects so that the effective effect is the propagation of these nonlinear pulses by the guide, figure 1. Nonlinear effects due to polarization of an optical beam propagating through a waveguide may be responsible for selecting certain propagation modes acting as a self-filter of wavelengths. Polarization in a nonlinear medium can be written as

$$\vec{P} = \varepsilon_0 \chi^{(1)} \vec{E} + \vec{P}^{NL}, \tag{1}$$

where, $\boldsymbol{E}$, ε_0, $\chi^{(1)}$ and $\boldsymbol{P^{NL}}$ are the Electrical Field, the Electrical permissiveness, the Electrical susceptibility and the non-linear polarization term respectively. The propagation of an optical beam in a non-linear medium is described by equation

$$\nabla^2 \vec{E} = \mu_0 \varepsilon_0 \frac{\partial^2 \vec{E}}{\partial t^2} + \mu_0 \frac{\partial^2 \vec{P}^{NL}}{\partial t^2} \tag{2}$$

where μ_0 is the magnetic permeability.

2. Applications

We can consider the propagation of an optical pulse in a given medium whose interaction of light with the constituents of this medium produces nonlinear optical effects such as the Kerr effect, for example, whose propagation equation can be derived from equation (2) taking into account the symmetries of the waveguide structure

$$\frac{d^2\phi}{dx^2} + [V + iW]\phi + |\phi|^2\, \phi = \lambda\phi \tag{3}$$

where the functions $V(x,y)$ and $W(x,y)$ are called optical potentials and describe the interaction between the optical beam and the waveguide structure, $\phi(x,y)$ is the optical pulse profile and λ is the propagation constant. We are able to reproduce the profile of the optical beam, as showed in figure 2, scattered by the crystal lattice described by optical potential, figure 3. These functions can properly describe an optical network. The optical potential can describe an optical scattering network and its symmetry properties. In this sense, the non-linear effects from scattering of light with the constituents of the waveguide material as the non-linear polarization effects carry information with respect to the crystal lattice acting as a scattering element. Thus waveguides can be appropriately designed to drive certain modes of propagation and exclude others. Thus these non-linear optical beams act as natural optical filters that have their own band structure [1,2].

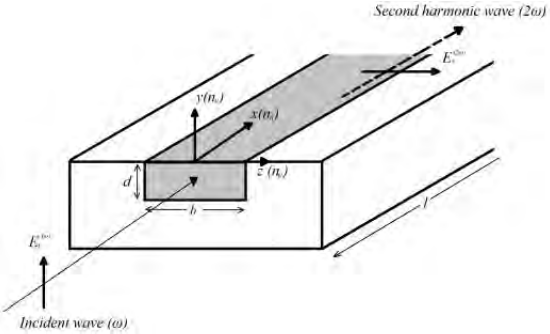

Figure 1. Waveguide with Electrical Field E directions, refractive indices, incident wave, dimensions and polarization (second harmonic generation).

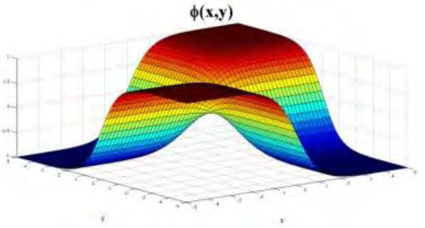

Figure 2. Optical beam profile as solution of equation (3) on the waveguide.

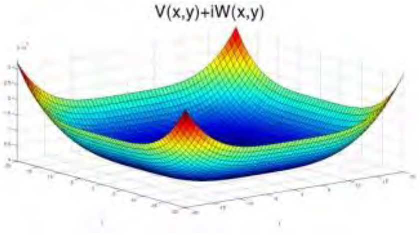

Figure 3. Optical potential: $(x^2-a^2)^2$ where a is a constant.

3. References

[1] Noda J, Optical Communication Handbook, 1st. ed., (H. Yanay, Asakura Book Co., Japan, 1982).

[2] Musslimani Z. H, Makris K. G, El-Ganainy R and Christodoulides D. N, “Optical Solitons in PT Periodic Potentials” Phys. Rev. Lett. 100, 030402 (20085).

Sensor Based on an Optical Diffraction Network

Antônio C. AMARO DE FARIA Jr[1*]
[1]Photonics Division, Institute for Advanced Studies, 1222000 Sao Jose dos Campos, Brazil
[2]Mechanical Eng. Department, Federal Technological University of Parana, 85053525, Guarapuava, Brazil
*Corresponding author: atoni.carlos@gmail.com

Abstract – We present the design of a sensor based on a optical diffraction network whose applications extend from optical filters to the processing and transmission of optical signals in integrated circuits. The characterization and application of this sensor are also presented. The physical parameters of the sensor such as the wavelength of the light used, the width of the optical diffracted pulse, the distances between the diffracted beams among others may be conveniently correlated with their respective functions and sensitivity.

Keywords – optical sensor; diffraction grating; multiplexers; demultiplexers

1. Introduction

We designed a sensor based on an optical diffraction network characterized by a set of slits that one extend regularly through a planar network. An incident optical beam is diffracted in each slit producing a scattered optical beam whose relative optical intensity can be controlled by the diffraction grating dimensions and the angle of incidence of the optical beam [1]. The result is an optical beam that produces a precisely localized interference pattern on a particular bulkhead in the device itself. The relative light intensity of the scattered beam is given by

$$I(\alpha) = I_1(\alpha).\frac{\sin^2\left(N\frac{\Delta}{2}\right)}{\sin^2\left(\frac{\Delta}{2}\right)}, \qquad (1)$$

with $\alpha = \sin\,\theta$, θ the angle of direction of the incident optical beam, N is the number of slits, Δ the lag between corresponding points of the two slits and $I_1(\alpha)$ is the intensity of the beam scattered through a slit. We can modulate the signal of the diffracted beam by regulating the dimensions of Δ and N. For $|\Delta| << 1$ and $N >> 1$, for example, we obtain a distribution function of the relative optical intensity of the scattered beam characterized by $N^2\sin^2(N\Delta/2)/(N\Delta/2)^2$, figure 1 Left.

2. The Sensor

These illumination points may be suitably coupled to a waveguide or to a network of waveguides which will conduct the modulated optical beam from the diffraction point considered. The network has a periodic structure along the plane of the waveguide. The guided modes of the propagating beam are collinearly coupled by the network. The optical beam can reach on the diffraction grating through a waveguide that produces distinct wavelengths by collimating and focusing on a set of photodiodes [2]. The photodiode array may be located appropriately at the points of maximum or minimum optical intensity according to the angular spacing that can be properly regulated through the deflection angle: $2\theta_b = d/\lambda$ where d is the spacing between the slits which are represented by the traces indicating the transmission grating filter of figure 1. The diffraction pattern is shown in figure 2.

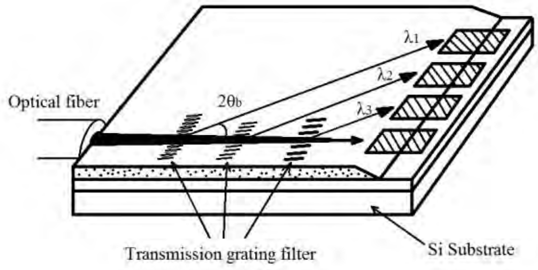

Figure 1. Layout of the sensor consisting of a diffraction grating and photodiodes.

3. The Optical Diffraction Network

As shown in figure 2 the interference pattern given by the optical intensity I(α) is fully characterized by the parameters (λ/d), giving the optical intensity peak width, (λ/Nd) giving the distance between two consecutive peaks and (N^2) giving the amplitude of the optical intensity.

Thus all these parameters can be converted into electrical signals whose corresponding electrical voltage can be properly recorded and processed.

In Figure 1, these interference patterns can be properly generated and transmitted by the transmission grating filter and appropriately correlated through wave packets with corresponding wavelengths λ_1, λ_2 and λ_3.

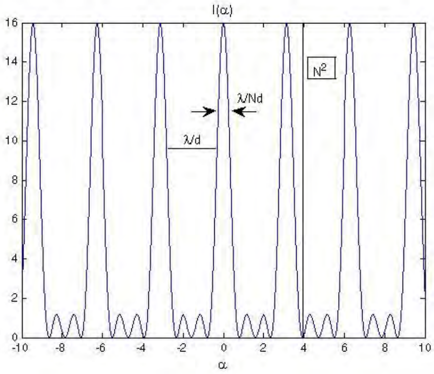

Figure 2. Graph of function I(α).The peak width is given by λ/Nd, the distance between the peaks is λ/d and the intensity is given by N^2. As we can observe these parameters can be properly modulated in order to control the scattered optical beam.

4. The Optical Diffraction Network

As shown in figure 2 the interference pattern given by the optical intensity I(α) is fully characterized by the parameters (λ/d), giving the optical intensity peak width, (λ/Nd) giving the distance between two consecutive peaks and (N^2) giving the amplitude of the optical intensity.

Thus all these parameters can be converted into electrical signals whose corresponding electrical voltage can be properly recorded and processed.

In Figure 1, these interference patterns can be properly generated and transmitted by the transmission grating filter and appropriately correlated through wave packets with corresponding wavelengths λ_1, λ_2 and λ_3.

The optical diffraction network consisting of a array of diffraction gratings, in figure 1, is an integrated device with an $As_2S_3/SiO_2/Si$ waveguide that is a micrograting-array demultiplexer.

5. Conclusion

In this work we present the design of an optical sensor based on an optical diffraction network. This sensor is characterized by physical parameters such as wavelength of light used, width of separation between the slits, among others, whose sensitivity and precision can be conveniently adjusted by these parameters.

6. References

[1] Rossi B, Optics, 1st. ed., (Addison-Wesley, Reading, 1957).

[2] Rics R. R et al "Multiwavelength monolithic integrated fiber optical terminal", Proc. Soc. Photo-Optical Instr. Eng., 176, 133 (1979).

Array-Antenna-Electrode Electro-Optic Modulators Operating in 80 GHz Band Using Low-Dielectric-Constant and Low-Loss Fluorine-Based Resin Substrate

Shin YAMASAKI[1], Toshiyuki INOUE[1], Shiomi HIDEISA[1], Atsushi SANADA[1],
Satoshi KIYA[2], Makoto NAKABAYASHI[3], Kazuo MURATA[4,2], and Hiroshi MURATA[1*]

[1]Graduate School of Engineering Science, Osaka University Toyonaka, Osaka 560-8531 Japan
[2] Sumitomo Electric Printed Circuits Minakuchi-cho, Koga, Shiga 528-0068 Japan
[3]Sumitomo Electric Fine Polymer Kumaori-cho, Sennan, Osaka 590-0458 Japan
[4]Sumitomo Electric Industries Chuo-ku, Osaka 541-0041 Japan
*Corresponding author: murata@ee.es.osaka-u.ac.jp

Abstract – We have proposed and developed antenna-coupled-electrode (ACE) electro-optic modulators (EOM), which enable us to convert microwave (MW)/millimeter-wave (MMW) wireless signals to optical signals directly without external power supply. The basic operations of the proto-type ACE EOMs have been demonstrated successfully in the frequency range of 10-65 GHz. Their applications to MW/MMW sensing, radar systems, and 5G wireless communication systems are now undergoing. In this paper, a new challenge for the operation in higher frequency range, 80 GHz band by use of fluorine-based resign with low dielectric constant and low loss from Sumitomo Electric Industries is presented. By using the fabricated ACE EOM, 80 GHz wireless signals of a few mW were directly converted to optical signals without external power supply. The frequency response was in good agreement with the designed characteristics.

Keywords – Array Antenna, Optical Modulator, Millimeter-Wave, Fluorine-Based Resin, Radio-over-Fiber

1. Introduction

Recently, applications of millimeter-wave (MMW) wireless are attracting a lot of interest: for high-resolution radar/imaging systems, next generation (5G) mobile communication systems, remote sensing, and molecular spectroscopy. One drawback of MMW wireless systems is a large transmission loss in both air and cables compared to microwave (MW). Therefore, the radio-over-fiber (RoF) technique is important for the MMW applications [1].

Our group has proposed and developed antenna-coupled-electrode (ACE) electro-optic modulators (EOM) [2]-[5], which can convert wireless MW/MMW signal into lightwave (LW) signals directly without a power supply. Therefore, ACE EOMs are suitable for RoF systems in MW and MMW frequency ranges. In addition, by utilizing an array structure in ACEs and polarization-reversed structures in ferro-electric crystal substrate, wireless signal discrimination according to the irradiation angle to the array is also possible without complicated MW/MMW signal synthesis circuits like a Butler matrix [4], [5]. The basic operation of the proto-type ACE EOMs have demonstrated successfully in the frequency range of 10-65 GHz. In this paper, a new challenge for the operation in the higher frequency range of 80 GHz band is reported. By use of fluorine-based resign with low dielectric constant and low loss from Sumitomo Electric Industries, an 80 GHz wireless signal was successfully converted to a LW signal without external power supply.

2. Device Structure

The structure of the proposed device is shown in Fig. 1, where an array of ACEs is set along optical waveguides in a ferro-electric electro-optic (EO) crystal of $LiNbO_3$. The ACE is composed of a pair of planar patch antennas for receiving 80 GHz-band MMW signals and a standing-wave resonant electrode for conversion a signal from MMW to LW. The patch antennas are simple square-shape micro-strip based ones, and the standing–wave resonant electrode is composed of a coupled micro-strip line with short lines in the both ends. The two antennas and the resonant electrode is connected by use of a pair of micro-strip feedlines.

In order to have a good conversion characteristic in the MMW frequency ranges, the stacked-substrate structure composed of a thin (50 μm) $LiNbO_3$ crystal film and a 100 μm-thick fluorine-based resign plate is adopted. By using the stacked-substrate structure, the effective dielectric constant of the whole substrate becomes small compared with the substrate of an EO crystal only. Therefore, the antenna areas and modulation electrode length become larger and the conversion efficiency from the wireless to optical signals becomes higher.

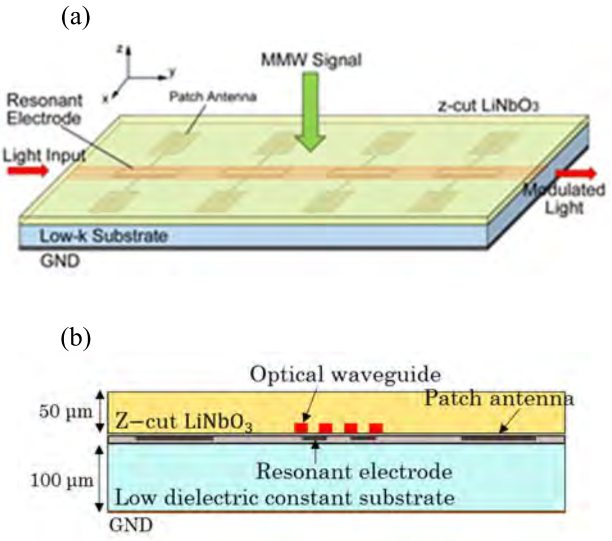

Figure 1. Basic structure of the ACE EOM. (a) Whole view. (b) Cross sectional view.

3. Analysis and Design

For the analysis and design of the ACE, we used 3-dimensional electric field analysis software, HFSS ver. 16 to obtain effective operation in the 80 GHz band.

Figure 2 (a) shows examples of the calculated surface electric field distributions on the metal of the ACE when an *x*-polarized plane-wave wireless signal of 79 GHz was irradiated to the ACE from above. In Figure 2 (b), we can see that a clear standing-wave electric field is induced along the electrode, and that its maximum value is over 150 times of the irradiated field. Therefore, an effective conversion of an 80 GHz-band MMW signal to a LW signal is expected. The designed parameters of the ACE is summarized in Table I.

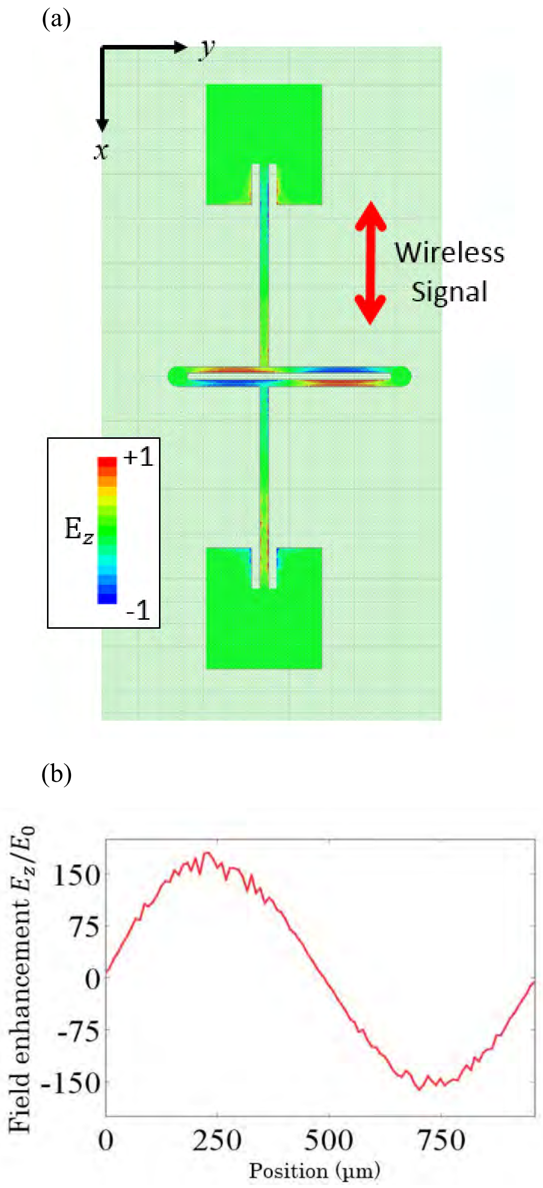

Figure 2. Pattern of the ACE and calculated surface electric field distribution when a 79 GHz plane-wave MMW signal is irradiated from above by use of HFSS ver. 16. (a) Surface electric field distribution. (b) Electric field distribution along the optical waveguide (modulation electric field).

Table 1. The parameters of the designed ACE EOM.

Antenna-coupled electrode (ACE)	
Operational frequency f_m	79 GHz
Electrode material and thickness t_e	Al, 1 μm
Square patch antenna length L_1	536 μm
Width of connection MSL W_1	40 μm
Groove length for antenna coupling ΔG_x	182 μm
Groove width for antenna coupling ΔG_y	40 μm
MSL length along y-direction y_1	900 μm
MSL connection point to the electrode from the center Δx	182 μm
Resonant electrode length L_2	921 μm
Resonant electrode width W_2	30 μm
Resonant electrode separation S	30 μm
Stacked substrate and optical waveguide	
Operational light wavelength λ	~ 1.55 μm
Base substrate material and thickness t_b	Fluorine-based resign 100 μm
EO crystal material and thickness t_c	z-cut $LiNbO_3$ 50 μm
Optical waveguide fabrication method	Annealed proton-exchange
Optical waveguide core size $w \times d$	3 μm x 2 μm

4. Experiments

Based on the design, the 80 GHz-band ACE EOM was fabricated. The fabrication processes are essentially the same as for the previous devices [4], [5]. Figure 3 show a photograph of the fabricated ACE EOM for the 80 GHz band.

Figure 3 shows an example of the measured spectrum of the output light from the ACE EOM when a 79 GHz MMW signal of 10 dBm was irradiated from above. Clear modulation sidebands are identified. The measured frequency response is shown in Figure 4. The 3 dB bandwidth is over 5 GHz, therefore, this ACE EOM can be used for the data transfer over 5 Gb/s with a simple ASK modulation scheme.

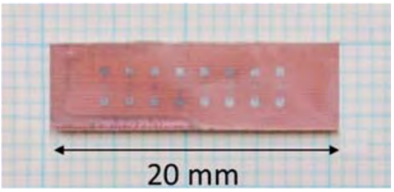

Figure 3. Photograph of the fabricated ACE EOM.

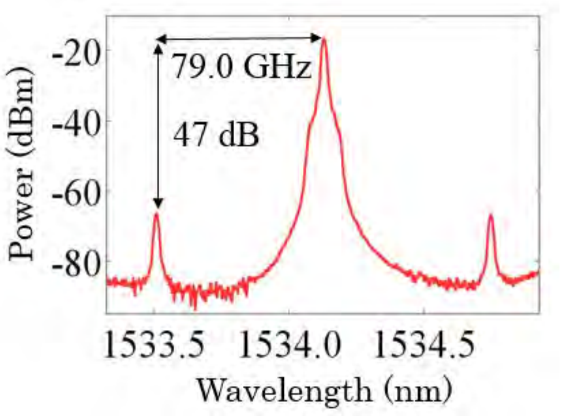

Figure 4. Measured optical spectrum from the fabricated ACE EOM.

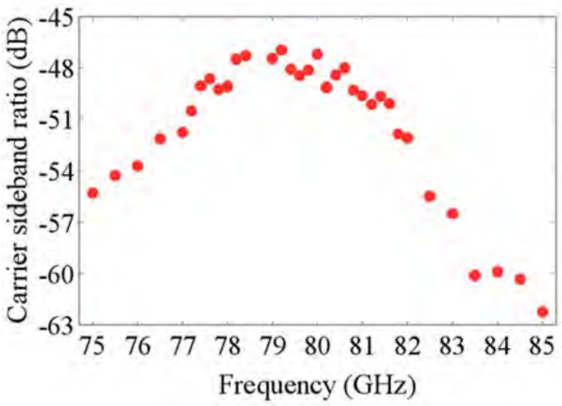

Figure 5. Measured frequency response of the fabricated ACE EOM.

5. Conclusions

The MMW-LW signal conversion in the 80 GHz band was demonstrated successfully. The obtained modulation index in the 80 GHz band is enough for the data transfer or detailed field sensing. We have also succeeded in the IF-band (~1 GHz) of the MMW signal by using the photonic technology of high-speed optical phase modulation in ~20 GHz.

The applications of the ACE EOM to MMW wireless channel sounding measurement systems are also expected.

Acknowledgement

The authors thank Prof. Yasuyuki Okamura of Osaka University, Japan for his valuable comments on the device design. The authors also thank Prof. H. Toda of Doshisha Univ., Japan, Drs. N. Yonemoto and Y. Kakubari of ENRI, Japan, Dr. N. Shibagaki of Hitachi, Japan, Dr. K. Ikeda of CRIEPI, Japan, and Dr. H. Mano of Koden Techno Info, Japan for their valuable discussion. This work was achieved in part by the research project of "Radio technologies for 5G using Advanced Photonic Infrastructure for Dense user environments (RAPID)," the commissioned research of NICT, Japan.

References

[1] J. Capmany and D. Novak, "Microwave photonics combines two worlds," *Nature photonics*, **vol.1**, pp.319-330, 2007..

[2] H. Murata, R. Miyanaka and Y. Okamura, "Wireless space-division-multiplexed signal discrimination device using electro-optic modulator with antenna-coupled electrodes and polarization-reversed structures," *Int. J. Microw. Wireless Technol.*, **vol.4**, pp.399-405, 2012.

[3] Y. N. Wijayanto, H. Murata and Y. Okamura et al., "Electro-optic millimeter-wave-lightwave signal converters suspended to gap-embedded patch antennas on low-*k* dielectric materials," *IEEE J. Sel. Topics Quantum Electron.*, **vol.19**, 3400709, 2013.

[4] N. Kohmu, H. Murata and Y. Okamura, "Electro-Optic Modulator Using an Antenna-Coupled-Electrode Array and a Polarization-Reversed Structure for a Radar Tracking System," *Radio Science Bulletin*, no.349, pp. 32-39, 2014.

[5] T. Inoue, K. Ikeda, Y. Kakubari, N. Yonemoto, N. Shibagaki, H. Toda and H. Murata, "Millimeter-Wave Wireless Signal Generation and Detection Using Photonic Technique for Mobile Communication Systems," *AVFOP/MWP 2016*, TuM1.8, October 2016, Long Beach, CA, USA.

Performance Evaluations of Surgical Energy Devices Using Microwave and Radio Frequency Current

Kazuyuki SAITO[1*], Masashi SUGIYAMA[2], and Ryo MANAGO[2]
[1]Center for Frontier Medical Engineering, Chiba University, 2638522 Chiba, Japan
[2]Graduate School of Science and Engineering, Chiba University, 2638522 Chiba, Japan

*Corresponding author: kazuyuki_saito@faculty.chiba-u.jp

Abstract – Today, many types of surgical devices using radio frequency (RF) current, ultrasound, laser etc. They are called "energy devices". The energy devices are indispensable for modern surgical operations. This paper describes development of surgical devices by use of the microwave thermal effect. There are some merits using the microwave devices by comparison with other practical surgical devices. However, the microwave devices also have some weaknesses. Therefore, in this study, surgical devices combining the RF current and the microwave energy will be developed.

Keywords – surgical device; microwave; RF current; pencil type device

1. Introduction

Generally, electric scalpel has widely been used for surgical operation and employs the RF (from several hundred kHz to several MHz) current. The electric scalpel can sharply incise biological tissue. On the other hand, the device is not good at the tissue coagulation. In order to realize clear coagulation of the tissue, modern electric scalpel system equips several wave forms of RF current. However, fog and tissue carbonization will occur, because the device based on the discharge between the device tip and the tissue surface. According to our preliminary investigations, a surgical device based on the microwave technology can coagulate the tissue appropriately [1]. These characteristics are listed in Table 1. In this study, pencil type device by combining the RF current and the microwave (2.45 GHz) are developed. Moreover, the performances of developed devices are evaluated by the numerical calculations based on the finite difference time domain (FDTD) techniques and some experiments by use of extracted organs.

Table 1. Characteristics of surgical devices.

	Tissue resection	Tissue coagulation
RF current (from several hundred kHz to several MHz)	○	△
Microwave	×	◎

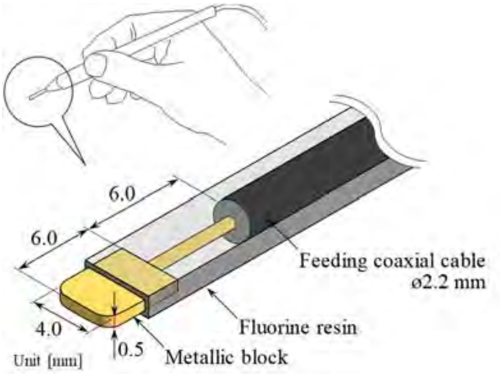

Figure 1. Proposed surgical energy device.

2. Device Structures

The authors have been studying several types of microwave surgical devices. In this paper, a "pencil type" device shown in Fig. 1 is introduced. The device tip operates such as a monopole antenna a role of electrode for tissue incision by the discharge. The energy source (RF current or microwave) can be selected according to preference of the surgeon. The RF current can cut target and the microwave generates coagulated region for the hemostasis. Of course, the RF current can be used for the tissue coagulation.

The operating frequency of the microwave region is 2.45 GHz, which is one of the industrial, scientific and medical (ISM) frequencies.

3. Characteristics of Device

Figure 2 shows calculation model for investigations and some parameters for the calculation are listed in Table 2. Detail procedure of the calculation is explained in [2]. Figure 3 shows a calculated reflection coefficient of the device around the operating frequency. At the operating frequency, reflection coefficient is -10.9 dB. It is acceptable for practical use. Figure 4 shows calculated temperature distribution [3] around the device when the device is used for microwave tissue coagulator. From the results, high temperature region can be observed around the device tip.

4. Summary

In this study, pencil type surgical device combining the RF current and the microwave was developed and evaluated its characteristics. As a further study, practical device based on this technique should be developed.

5. Acknowledgement

A part of this study has supported by the Japan Society for the Promotion of Science, Grant-in-Aid for Scientific Research (C) 15K06010.

References

[1] Endo Y, Saito K, Ito K. The Development of Forceps-Type Microwave Tissue Coagulator for Surgical Operation. IEEE Trans. Microw. Theory Tech. 2015; 63(6): 2041-2049.

[2] Saito K, Hayashi Y, Yoshimura H, Ito K. Heating Characteristics of Array Applicator Composed of Two Coaxial-Slot Antennas for Microwave Coagulation Therapy. IEEE Trans. Microw. Theory Tech. 2000; 48(11): 1800-1806.

[3] Pennes H H. Analysis of Tissue and Arterial Blood Temperatures in the Resting Human Forearm. J. Appl. Physiol. 1948; 1(2): 93-122.

Table 2. Physical properties for calculations.

	Electrical properties (@2.45 GHz)	
	Relative permittivity	Conductivity [S/m]
Liver	43.0	1.69
Blood	-	-

	Thermal and other properties			
	Specific heat [J/kg/K]	Thermal conductivity [W/m/K]	Density [kg/m^3]	Blood flow rate [m^3/kg/s]
Liver	3,540	0.52	1,079	1.43×10^{-5}
Blood	3,960	-	1,050	-

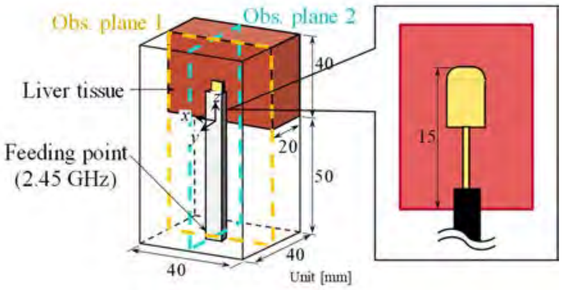

Figure 2. Calculation model.

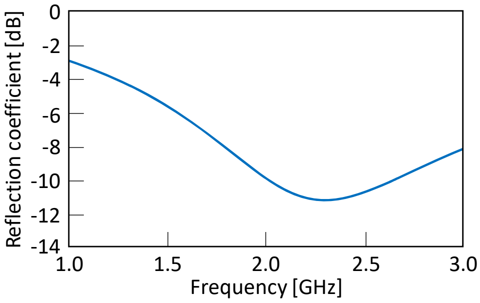

Figure 3. Calculated reflection coefficient.

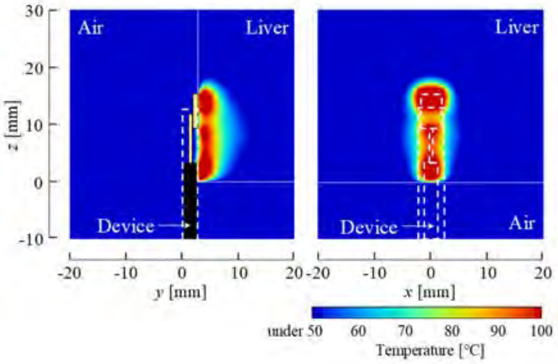

Figure 4. Calculated temperature distributions.

Non-Destructive Inspection of Buried Pipeline Composed of Fiberglass-Reinforced Plastic Mortal Using Electro-Optic Sensor and Microwave Guided-Modes

Yoshiyuki AZUMA[1], Fumiaki UENO[1], Hiroshi MURATA[1*], Atsushi Sanada[1],
Tadahiro OKUDA[2], and Masaya HAZAMA[2]
[1]Graduate School of Engineering Science, Osaka University Toyonaka, Osaka 560-8531 Japan [2]Kurimoto LTD Higashi-Ohmi, Shiga 52-0108 Japan
*murata@ee.es.osaka-u.ac.jp

Abstract – We have proposed and developed a new non-destructive inspection method for buried fiberglass-reinforced plastic mortar (FRPM) pipelines by using precise photonic measurement of transmission and scattering of microwave guided-modes. In this paper, new measurement results for a buried agricultural water pipelines under a road are reported.

Keywords – Electro-optic sensor, Microwave, Dielectric waveguide, FRPM, non-destructive measurement

1. Introduction

An electro-optic (EO) sensor is a small invasive sensor for electro-magnetic fields in RF and microwave (MW) frequency ranges, since it can be composed of non-metal or minute metal elements. Therefore, an EO sensor is useful for many application of RF and MW field measurements required small invasiveness and high accuracy [1], [2].

Fiberglass-reinforced plastic mortar (FRPM) has high mechanical strength and high chemical corrosion resistance despite being lightweight. Therefore, FRPM is used in many application fields such as protecting tubes for electric power/optical fiber cables, sewer pipes and agricultural water pipes. Especially, the total length of the FRPM pipelines used for agricultural water supply is approximately 50,000 km in Japan. Therefore, an easy-to-use nondestructive inspection method for FRPM pipelines is required for regular testing and maintenance.

There are several candidates for the inspection method for FRPM pipelines: magnetic resonance imaging (MRI), X-ray and ultrasonic waves [3]. However, these methods are unsuitable for inspection of long and buried FRPM pipelines, since they require rather large and specific measurement machines. Therefore, there is no effective inspection method for long FRPM pipelines yet, as far as we know.

We have found that FRPM is a dielectric material with relatively small loss in the MW frequency range of 1~10 GHz and that a buried FRPM pipe can be a cylindrical-shaped dielectric waveguide for MW with a relatively low propagation loss. By utilizing these interesting characteristics, we have proposed a new inspection method for FRPM pipelines; the MW guided-modes are excited by use of appropriate antennas installed at the connection joint in the pipeline, and the transmission characteristics of the MW guided-modes are to be measured by use of an EO sensor or a small probe precisely. If a defect, crack or foreign object is in/on the FRPM pipe wall, the MW guided-mode propagation is disturbed, which leads to MW scattering into inner/outer spaces or coupling between guided-modes. As a result, the MW transmission is degraded [4], [5]. These change can be measured by use of an EO sensor or probe. In addition, by scanning the distribution of the evanescent MW fields on the inner surface of the FRPM pipe, we can also identify the position, size, and electrical characteristics of the defect, crack or object nondestructively. Therefore, we can inspect FRPM pipelines [4], [5]. In this method, an EO sensor is suitable since the invasive field measurement is a key point.

In this paper, new experimental measurement results of a buried agricultural water pipeline under a road are reported for the first time.

2. Principle of Measurement

A schematic of the proposed inspection method is shown in Figure 1. In this method, an FRPM pipe is used as a core of a cylindrical-shaped MW dielectric waveguide, which is composed of a FRPM pipe wall (core), surrounding sand (outer cladding), and inside air (inner cladding). A MW signal is to be input from one end of the FRPM pipe at the connection joint, and propagates along the pipe-wall. The propagated MW signal can be detected at the opposite end of the pipe by use of an EO sensor. If there is a defect, crack or foreign object in the pipe wall inside or on the outer surface, the MW propagation is distorted by them. Thus, the transmitted signal level is degraded and the MW distribution on the inner surface is changed. Therefore, we can detect them as the change in the transmission and distribution of the MW.

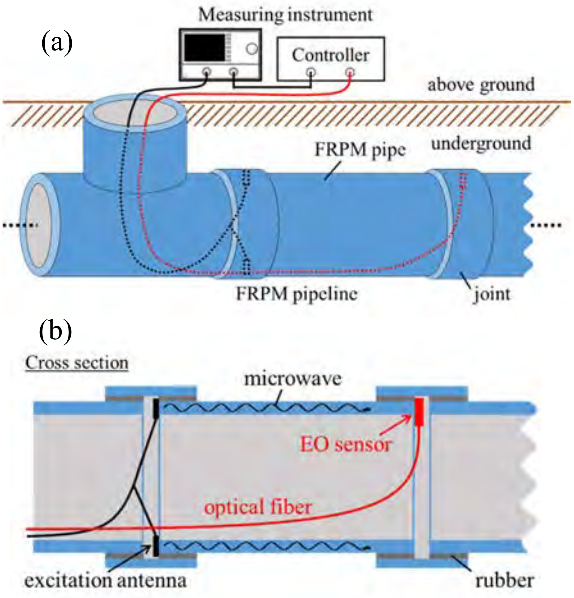

Figure 1. Schematic of the proposed inspection method. (a) Whole view. (b) Cross sectional view along the pipeline direction.

3. Analysis

The detailed analyses of the MW guided-modes along buried FRPM pipelines have been reported in [4] and [5]. Then, only some important results are shown here. Figure 2 shows modal dispersion curves of the guided-modes propagating along FRPM pipelines buried underground. We can see that there is only a single guided mode (TE_{00}) for TE waves at 2.4 GHz, while there are two TE guided modes (TE_{00}, and TE_{01}) at 6 GHz. The field distributions of the two modes at 6 GHz are plotted in Figure 3.

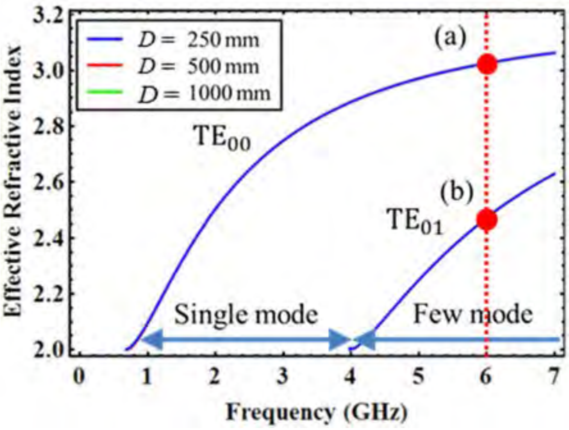

Figure 2. Dispersion characteristics of guided-modes propagating along the FPRM pipeline underground.

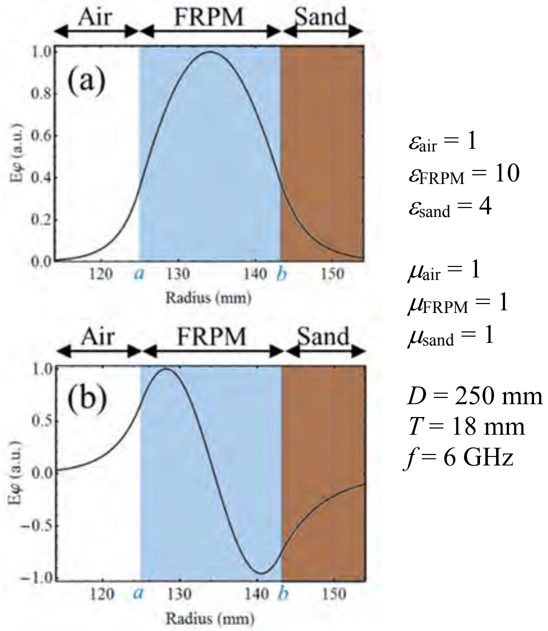

Figure 3. Electric field distributions of the guided-modes indicated by (a) and (b) in Figure 2.

Another important characteristic is that in Figure 2, the three dispersion curves with the same thickness (T =18 mm) but different diameter values (D = 250/500/1000 mm) are almost overlapped in these frequency ranges. Therefore, this method can be applied various diameter pipelines as long as the wall thickness value is almost the same.

4. Experiments

We have tried to do experiments of the proposed inspection method for a FRPM pipe/pipeline in an experimental room and in a factory, and verified its usefulness for nondestructive inspection. Based on these results, we have tried to do an experiment for a buried agriculture water pipeline under a public road.

The photographs for the agriculture water pipeline to be measured and the surroundings are shown in Figure 4. We have tried to measure MW transmission /scattering for the selected 10 pipes underground from a 2 km-long pipeline for agriculture water supplying. The experiment was done in the off-season of agriculture in the area. Therefore, the pipeline inside was not water filled, but a little water remained (wet condition).

The diameter, D, and thickness, T, of the buried pipe were 1,350 mm and 34 mm, respectively. In the pipeline, 4 m-long pipes were connected by use of connection joints with a slightly larger diameter and sealing rubber. At the connection joint, a few mm-long gap was located between the connected pipes, and we can install a small dipole antenna to input MW signals from 1 to 6 GHz along the pipeline.

An example of the measured MW transmission along a 4-m-long pipe is shown in Figure 5. We can see that clear MW signal transmission in the underground pipeline. The measured transmission characteristics indicates a clear co-relationship with other measurement results of mechanical strains and deformations. For the pipes with large mechanical strains, less MW transmissions were identified, which coincided well with our expectation.

For the two pipes which indicated the small MW transmission and large mechanical strains, we also tried to do measurement by scanning the probe on the inner pipe walls. The results are shown in Figure 6. Although the surfaces of the inner pipe walls were clean and uniform, the MW intensity variations along the inner surface were identified clearly. The measured variation patterns were in good agreement with the mechanical strain distributions. Therefore, the patterns of Figure 6 indicate the existence of foreign objects on the outer surfaces of the measured pipe, we believe.

Figure 4. Photographs about the FRPM pipeline used for the field experiment. (a) The road where the FRPM pipeline is buried 2 m underground. (b) The man-hole to access the buried FRPM pipeline. (c) Inside the FRPM pipeline to be measured.

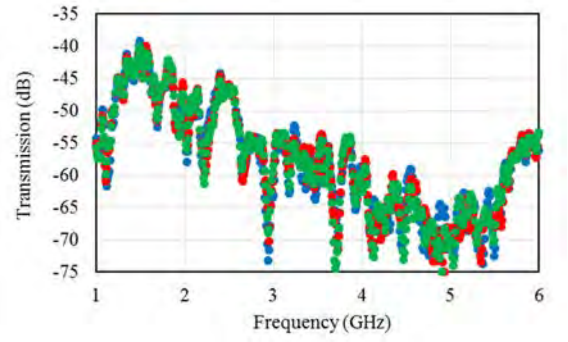

Figure 5. Measured MW transmission characteristics for the buried FRPM pipe.

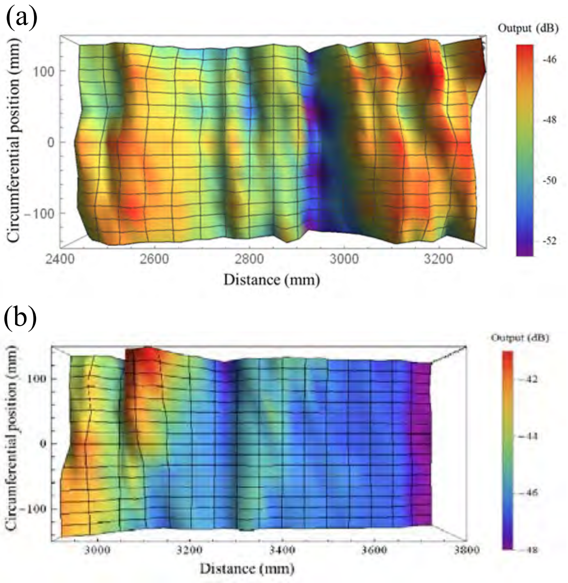

Figure 6. Measured MW intensity distribution on the inner surface of the selected two buried pipe.

5. Discussion and Conclusion

We have demonstrated the new nondestructive inspection method for FRPM pipelines. The MW signals propagating along the FRPM pipe-wall were affected by a defect, crack or foreign object in/on the pipe walls. The difference of MW transmission and field distributions between normal and abnormal pipes were clearly identified by use of an EO sensor. We can also identify the position of the defect, crack or foreign object by scanning the EO sensor with small invasiveness from the inside surface of the pipe wall. Therefore, the pipelines can be inspected nondestructively from its inner surface by use of the MW and photonic techniques.

Acknowledgement

The authors thank Prof. Yasuyuki Okamura and Dr. Hidehisa Shiomi of Osaka University, Japan for their valuable comments on the analysis. The authors also thanks to Dr. Satoru Kurokawa and Dr. Masanobu Hirose from AIST, Japan for their valuable comments. The authors also thanks to Dr. Yoshikazu Toba from SEIKOH GIKEN Co. Ltd. for the provision of the EO sensor.

References

[1] T H. Togo, S. Mochizuki, and N. Kukutsu. “Optical fiber electric field sensor for antenna measurement,” NTT Technical Review, vol.7, no.3, March 2009.

[2] H. Togo, N. Shimizu, and T. Nagatsuma, “Tip-on-fiber Electro-optic Probe for Near-field Measurement,” NTT Technical Review, vol.4, no.1, Jan. 2006.

[3] E. Marfisi, C. J. Burgoyne, L. D. Hall, and M. H. G. Amin, "Use of the MRI technique to study concrete and FRP reinforced concrete behavior," Research Leading to the Development of Design Guideline for the Use of FRP in Concrete Structure – 2nd ConFiberCrete Young Researcher Conference, Corfu, Greece, June 2002.

[4] F. Ueno, H. Murata, T. Okuda, M. Hazama, and Y. Okamura, “New Nondestructive Measurement for Fiberglass-Reinforced Plastic Mortar Pipes Using Microwave and Photonic Techniques,” MWP/APMP 2014, TuED-2, Sapporo, Japan, Oct. 2014

[5] Y. Azuma, F. Ueno, H. Murata, Y. Okamura, T. Okuda, and M. Hazama, “Precise Measurement of Microwave Evanescent Fields along Fiberglass-Reinforced Plastic Mortar Pipe Using Electro-Optic Sensor for Nondestructive Inspection,” OECC/PS 2016, WA2-73, July, 2016.

SPONSORS AND EXHIBITORS

I – Wave Corporation

Sevensix Inc.

Sumitomo Osaka Cement Co., Ltd.

WAKA Manufacturing Co., Ltd.

Awards

Schmid & Partner Engineering AG

PEM2017

Organizers

IT'IS Foundation
Zeughausstrasse 43, 8004 Zurich
Tel: +41 44 245 96 86 Email: info@itis.ethz.ch www.itis.ethz.ch